Tampere University

Veera Peltonen

HIGH STRAIN RATE TENSILE TESTING OF A NICKEL SUPERALLOY

Master's thesis
Faculty of Engineering and Natural Sciences
Mikko Hokka
Matti Isakov
October 2020

ABSTRACT

Veera Peltonen: High strain rate tensile testing of a nickel superalloy
Master's thesis
Tampere University
Materials Science
October 2020

In this thesis a novel nickel-based superalloy was studied to determine whether it is suitable to be used as a turbine blade material of a jet engine based on its tensile properties both at room temperatures and at elevated temperatures. Turbine blades encounter temperatures as high as 700 °C. The material is tested at high strain rates to examine the dynamic behaviour of the studied nickel-based superalloy.

The theory part includes Chapters 2-4. In Chapter 2, the effect of strain rate and temperature on material properties is discussed, followed by the basic working principles of a turbine engine and the materials used in turbine engines in Chapter 3. Chapter 4 discusses different dynamic testing methods, focusing on Split Hopkinson bar, since Split Hopkinson tensile bar was used in the experiments of the thesis.

Chapter 5 presents the experimental setup and the used material. The experimental setup was a Split Hopkinson tensile bar and the tensile pulse was created with a striker bar at a strain rate range of 320-450 1/s. At the elevated temperatures, a furnace was used to heat the sample and a water-cooling system was placed on both sides of the furnace to keep the temperature of the bars at room temperature. The testing temperatures were room temperature (20 °C), 650 °C and 760 °C. The samples were 20 mm long and had a diameter of 4 mm. Altogether 18 samples were tested, 6 at each temperature. The samples were mounted to place with a screw at both ends of the samples. The chemical composition nor the heat treatment history of the material is not known, since it is a proprietary industrial material. It is known, however, that the material is a nickel-based superalloy intendent to be used in turbine blades. The data of the experiments was processed with Excel and the steps are also explained in Chapter 5.

The results were presented and discussed in Chapter 6. The ultimate tensile strengths were 1460 ± 11 MPa at room temperature, 1200 ± 10 MPa at 650 °C, and 1180 ± 12 MPa at 760 °C. The ultimate tensile strengths were determined from the stress strain curves. The yield strengths were impossible to determine from the stress strain curves since the screw mounting of the samples caused oscillations in the beginning of the stress strain curves. For this reason, a Johnson-Cook model fitting was carried out with Matlab to estimate the yield strengths. Also, Johnson-Cook model parameters make it easier to compare the material to other nickel-based superalloys used in turbine engines. The yield strengths were 900 ± 1 MPa at room temperature, 830 ± 1 MPa at 650 °C and 780 ± 2 MPa at 760 °C. The yield strength and especially the ultimate tensile strength of the studied nickel-based superalloy were high at room temperature when compared to other nickel-based superalloys. However, both strengths decreased with increasing temperature which is not typical for nickel-based superalloys at a temperature range of 20-800 °C.

The Johnson-Cook model fitting was representative of the experimental results. The parameters were A = 900 MPa, B = 3377 MPa, n = 0.75, C = 0.01, and m = 3.5. The strain hardening related parameters B and n were high, when compared to parameters of other nickel-based superalloys found in literature. The strain rate related parameter C was in the same range as the other nickel-based superalloys. Temperature softening related parameter m was also high when compared to other nickel superalloys.

Keywords: nickel alloys, nickel superalloys, high strain rate, dynamic testing, Split Hopkinson Tensile bar, High temperature Split Hopkinson Bar, aerospace materials, turbine engine materials

The originality of this thesis has been checked using the Turnitin OriginalityCheck service.

TIIVISTELMÄ

Veera Peltonen: Nikkelisuperseoksen suurien myötönopeuksien vetokokeet
Diplomityö
Tampereen yliopisto
Materiaalitekniikka
Lokakuu 2020

Tässä työssä tutkittiin uutta nikkelipohjaista superseosta sekä huoneenlämmössä että korotetuissa lämpötiloissa, jotta saataisiin selville, onko materiaali sopiva käytettäväksi lentokoneturbiinissa. Materiaalin tulee kestää jopa 700 °C ja sitä testataan korotetuilla myötönopeuksilla, jotta saadaan selville sen dynaaminen käytös.

Työn teoriaosuus käsitellään luvuissa 2-4. Luvussa 2 puhutaan myötönopeuden ja lämpötilan vaikutuksista materiaaliominaisuuksiin. Sitä seuraa turbiinimoottorin toimintaperiaatteen ja turbiineissa käytettävien materiaalien esitteleminen luvussa 3. Luvussa 4 käsitellään erilaisia dynaamisessa materiaalikoetuksessa käytettäviä testimetodeja. Painopiste on Split Hopkinson Bar -testauksessa, sillä sitä käytettiin myös työn kokeellisessa osiossa.

Luvussa 5 esitellään työn testilaitteisto ja tutkittava materiaali. Testilaitteisto oli Split Hopkinson tensile bar, jolla tehtiin vetokokeita myötönopeuksilla 320-450 1/s. Korotettujen lämpötilojen testeissä näyte lämmitettiin testilaitteistoon integroidulla uunilla, jonka molemmin puolin sijoitettiin vedellä toimiva jäähdytysjärjestelmä, jolla varmistettiin, että laitteiston tankojen lämpötila pysyi huoneenlämmössä. Testauslämpötilat olivat huoneenlämpö (20 °C), 650 °C ja 760 °C. Näytteet olivat pituudeltaan 20 mm ja läpimitaltaan 4 mm, näytteiden poikkileikkaus oli pyöreä. Näytteitä oli yhteensä 20, joista 18 testattiin, 6 jokaisessa lämpötilassa. Näytteet kiinnitettiin laitteiston tankoihin ruuvaamalla. Materiaalin kemiallinen koostumus tai lämpökäsittelyhistoria eivät ole tiedossa, sillä materiaali on tarkoitettu teollisuuden käyttöön. On kuitenkin tiedossa, että materiaali on nikkelipohjainen superseos, joka on tarkoitettu käytettäväksi lentokoneturbiinissa. Testeistä saatu raakadata käsiteltiin Excelillä ja datakäsittelyn vaiheet on esitelty myös luvussa 5.

Tulokset esitettiin luvussa 6. Materiaalin vetomurtolujuudet olivat 1460 ± 11 MPa huoneenlämmössä, 1200 ± 10 MPa 650 °C:ssa ja 1180 ± 12 MPa 760 °C:ssa. Vetomurtolujuudet määritettiin jännitys-myötymäkäyristä. Myötölujuuksien määrittäminen jännitys-myötymäkäyriltä ei ollut mahdollista näytteenkiinnitystavasta johtuvasta oskillaatiosta käyrän plastisen alueen alussa. Tästä syystä materiaalille tehtiin myös Johnson-Cook-mallinnus, jonka avulla pystyttiin arvioimaan myötölujuudet. Johnson-Cook-mallinnus myös helpotti materiaalin vertaamista muihin turbiinimoottoreissa käytettäviin nikkelipohjaisiin superseoksiin. Myötölujuudet olivat 900 ± 1 MPa huoneenlämmössä, 830 ± 1 MPa 650 °C:ssa ja 780 ± 2 MPa 760 °C:ssa. Tutkitun materiaalin myötölujuus ja erityisesti vetomurtolujuus olivat huoneenlämmössä korkeita verrattuna kirjallisuudesta löytyviin nikkelisuperseosten lujuuksiin. Kuitenkin tutkitun materiaalin lujuus laski lämpötilan kohotessa, mikä on epätyypillistä nikkelipohjaisille superseoksille 20-800 °C välillä.

Johnson-Cook-mallinnuksella saatiin kokeellisia tuloksia hyvin kuvaava malli. Saadut parametrit olivat A = 900 MPa, B = 3377 MPa, n = 0.75, C = 0.01 ja m = 3.5. Myötölujittumisesta riippuvaiset parametrit B ja n olivat korkeita verrattuna kirjallisuudesta löytyviin nikkelipohjaisiin superseoksiin verrattuna. Myötönopeuteen liittyvä parametri oli samaa luokkaa kirjallisuudesta löydettyjen arvojen kanssa. Lämpötilasta riippuvainen parametri oli korkea verrattuna kirjallisuusarvoihin.

Avainsanat: nikkelisuperseos, korkea myötönopeus, dynaaminen testaus, Split Hopkinson Tensile Bar, lentokonemateriaalit, turbiinimateriaalit

Tämän julkaisun alkuperäisyys on tarkastettu Turnitin OriginalityCheck –ohjelmalla.

PREFACE

I want to thank everyone in the material sciences department for the education I hae received there and special thanks my mentor in Tampere, Mikko Hokka. I wouldn't have had this opportunity and experience if it wasn't for his suggestion to make a double degree and the support before and during my time in Madrid. Big thanks also to my mentor in Madrid, Victor Rey for all the help and support he has given me during the writing process and for working with me in the laboratory. I also want to thank Francisco Galvez for an interesting subject for my thesis. Great thanks to all my friends, family and the colleagues in both universities for the peer support and sometimes even peer pressure during this process.

Tampere, 8th October 2020

Veera Peltonen

CONTENTS

LIST OF FIGURES

LIST OF SYMBOLS AND ABBREVIATIONS

A_B	Area of the bar
A_{JC}	Constant in Johnson-Cook model
A_S	Area of the sample
B	Constant in Johnson-Cook model
BCC	Body Centered Cubic
C	Constant in Johnson-Cook model
C_0	Speed of sound
CCT	Cold Contact Time
D_B	Diameter of the bar
D_S	Diameter of the sample
E	Young's Modulus
FCC	Face Centered Cubic
G	Gain
IR	Infrared
K	Gage factor
K_H	Strength coefficient in Hollomon equation
L_s	Initial length of the sample
ln	Natural logarithm
n_H	Strain hardening coefficient in the Hollomon equation
n_{JC}	Constant in Johnson-Cook model
RT	Room temperature
SHPB	Split Hopkinson Pressure Bar
SHTB	Split Hopkinson Tensile Bar
T	Temperature
T_m	Melting temperature
T_{ref}	Reference temperature
t	Time
TSHB	Torsion Split Hopkinson Bar
U	Voltage
U_0	Constant voltage
UTS	Ultimate tensile strength
V	Interface velocity
X_a, X_e	Positions
ε	Strain
ε_{eng}	Engineering strain
ε_I	Initial pulse
ε_p	Plastic strain
ε_{pulse}	Strain of an elastic wave
ε_R	Reflected pulse
ε_{ref}	Reference strain rate
ε_T	Transmitted pulse
ε_{true}	True strain
$\dot{\varepsilon}$	Strain rate
ρ	Density
σ	Stress
σ_{eng}	Engineering stress
σ_{true}	True stress
σ_y	Yield strength
v	Poisson's ratio

1 INTRODUCTION

In this thesis, a novel nickel-based superalloy and its mechanical properties are being studied. This SX superalloy is planned to be used in turbine engine blades, where the temperatures can go as high as 700 °C [1], meaning that the material needs to hold its tensile properties even at elevated temperatures.

The superalloys were first introduced in the 1930s, and they typically include nickel, iron and cobalt based alloys [1]. The inventing of the turbine engine had a large contribution to the interest to develop the superalloys even further, and the ever-developing turbine engine demands constantly higher temperature resistance and lifetime cycles. The materials used in high temperature aerospace applications, meaning mostly the engines, are developing still further. In addition to the high temperatures, the nickel superalloys used in the highest temperatures can also encounter high strain rates, if something breaks within the engine or some foreign object hits the engine. Due to these sudden impacts, the mechanical properties of the nickel-based superalloys need to be good also at elevated temperatures and at high strain rates.

The strain rate and temperature dependence of the yield and ultimate tensile strength of the nickel-based superalloys are studied in this thesis. In addition, the temperature and strain rate sensitivity of the strain hardening of the material is determined. The alloy is tested with split Hopkinson tensile bar in 20-760 °C and with strain rates from 290 to 450 1/s. Also, a Johnson-Cook model and the Hollomon equation are fitted to the experimental data. The results of the tensile properties as well as the model fittings are compared to other results found in literature.

2 THE EFFECT OF TEMPERATURE AND STRAIN RATE ON MATERIAL PROPERTIES

The plastic deformation of a material is caused by dislocation movement [2], which is illustrated in Figure 2.1.

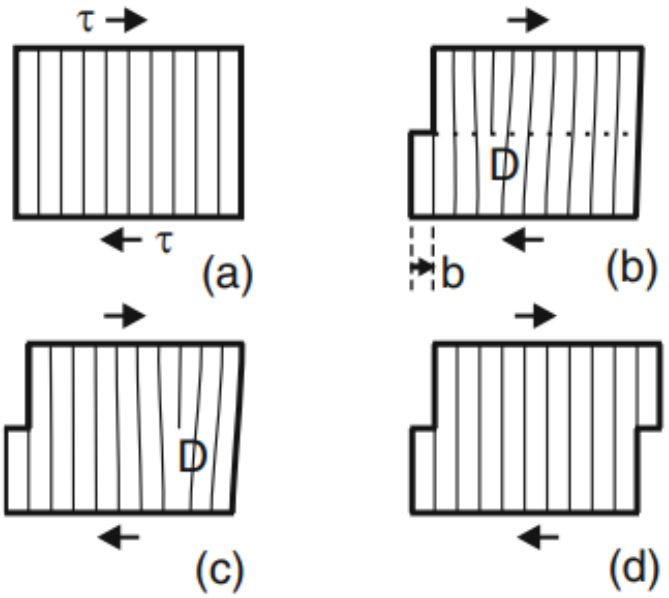

Figure 2.1. *Shear caused by dislocation movement of a dislocation [3].*

The strength of material can then be seen as its ability to prevent dislocation movement [4, 5]. Dislocation movement can be prevented with lattice friction, other dislocations, grain boundaries, solute atoms and precipitates. The movement of dislocations happens by the movement of atoms, jumping from one low energy position to another [6]. Dislocations move in a material mostly by gliding [6, 7]. The low energy points are called Peierls valleys and the high energy points between them Peierls hills [7]. In order to overcome the energy barrier between the two low energy positions, the atom needs energy, which can either be obtained from its own thermal vibrations or external mechanical energy, meaning shear stress [2, 6]. The effect of temperature on overcoming the obstacles is presented in Figure 2.2 a) and b).

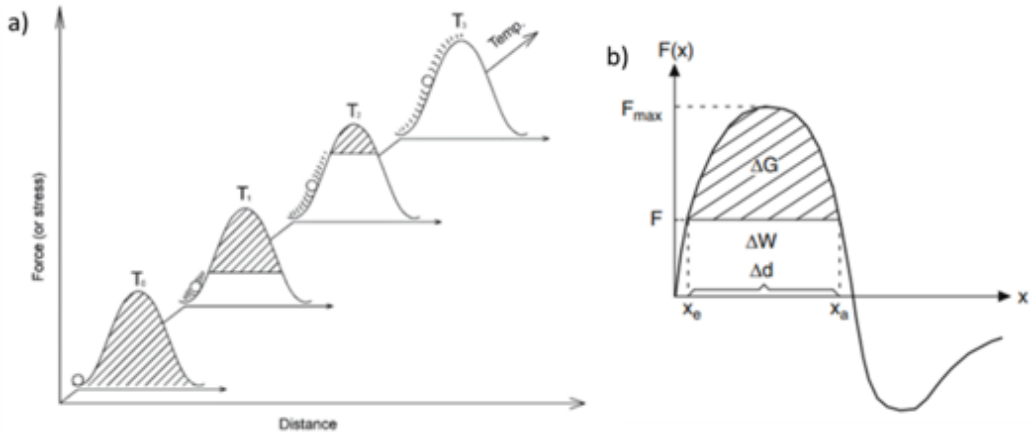

Figure 2.2. *The required mechanical and thermal energies to overcome a thermal obstacle. a) Shaded area is the proportion of mechanical energy needed and the unshaded the thermal energy of the atom [6] and b) the shaded area is the thermal energy [7].*

The thermal energy consists of the thermal vibrations of the atoms and its proportion grows higher with increasing temperature, as can be seen in Figure 2.2 a), when compared to the mechanical energy [7]. In Figure 2.2 b), the dislocation needs to travel distance from x_e to x_a with the help of the thermal energy, since the work, meaning the mechanical energy, only covers a part of the needed energy. In higher temperatures, the thermal vibrations of an atom increase, giving it more energy, thus making dislocation movement easier [6].

The above-mentioned thermal energy only helps significantly, when the obstacles are what is called thermal or thermally activated: if the obstacles are too long range, the thermal energy doesn't help the dislocation to overcome it [6, 7]. These obstacles are called athermal or extended obstacles. The thermally activated obstacles are also called localized obstacles, due to their shorter range [7]. The stresses of thermal and athermal obstacles and their dependence on temperature and strain rate are presented in Figure 2.3.

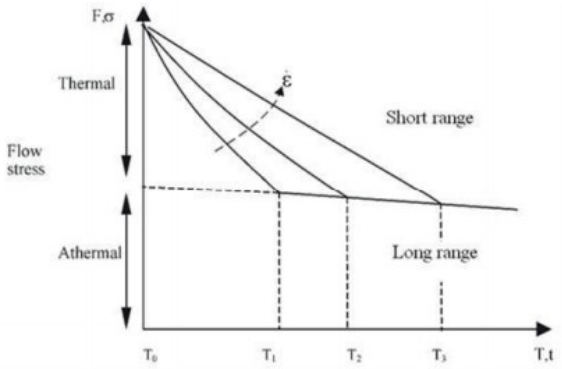

Figure 2.3. *The effect of temperature and strain rate on thermal and athermal obstacles of the flow stress [6].*

As can be seen in the Figure above, the thermal component of the flow stress decreases significantly with increasing temperature, but the athermal component of the flow stress is only slightly affected by the temperature. Increasing strain rate increases the thermal component of the flow stress, but the athermal component is not affected by the strain rate [6].

The strain rate affects the tensile properties, since the probability of the atom having enough energy to overcome an obstacle decreases with strain rate [6]. The waiting time of the dislocation for the overcoming an obstacle is shorter at higher strain rate, so it's less likely, that the atom will have enough thermal energy at the right moment. For this reason, higher yield strengths and ultimate tensile strengths are typically reached at higher strain rates.

The body centered cubic (BCC) metals are typically more sensitive to temperature and strain rate than the face centered cubic (FCC) metals [2]. The effects of temperature and strain rate on stress-strain curves of BCC and FCC metals are presented in Figure 2.4.

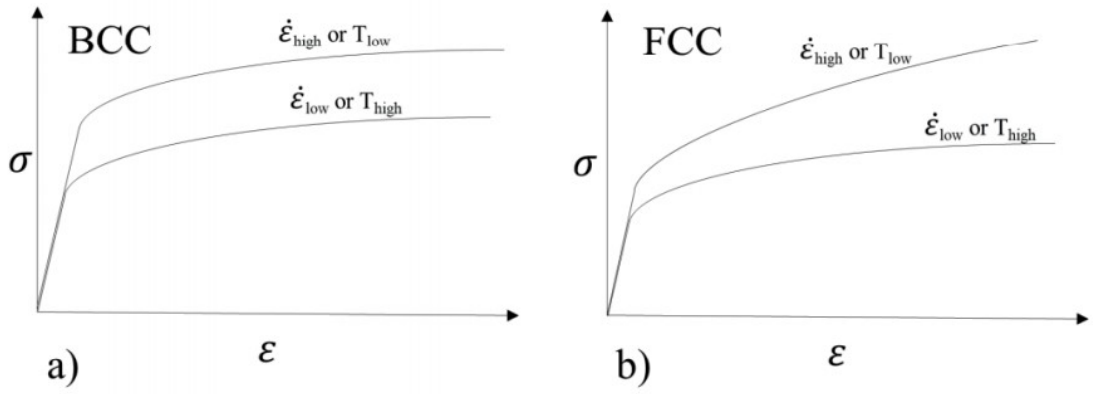

Figure 2.4. *The effect of strain rate and temperature on stress-strain curve of BCC and FCC metals [6].*

In BCC metals, the Peierls-Nabarro stresses, which are the stresses caused by the crystal lattice, are the biggest thermally activated obstacles for dislocation movement, whereas in FCC metals, the main thermally activated obstacle for dislocation movement is other dislocations and jog formation [2]. The strain hardening of pure BCC materials is independent from strain rate, since the Peierls-Nabarro stresses do not increase with growing strains. This leads to the curve keeping the same form even with higher strain rates, as is presented in Figure 2.4 a). In FCC materials, the dislocation motion gets harder with increasing amount of dislocations, especially in lower temperatures and with higher strain rates [8]. The Peierls-Nabarro stresses are small in FCC metals, since they have so good glide planes and systems. The dislocation density increases with growing

strain, leading to more jogs to block dislocation movement. The increasing number of jogs leads to increased strength with higher strains, as is presented in Figure 2.4 b).

The Peierls-Nabarro stresses and jog formation discussed above, are the main thermally activated mechanisms in BCC and FCC metals. In alloys, there are also the precipitates which are local concentrations of other phases in the base metal matrix. These obstacles can be divided into local and extended obstacles, depending on the size of the precipitates [7]. Extended precipitates are athermal obstacles, since due to their size, they can't be passed with thermal vibrations only, making them quite independent of the temperature. However, the size is not the only property of the precipitates that influences their strengthening abilities but also the volume fraction, shape and the interface between the precipitate and the matrix affect it. The interface can be either coherent, noncoherent or semicoherent, as illustrated in Figure 2.5.

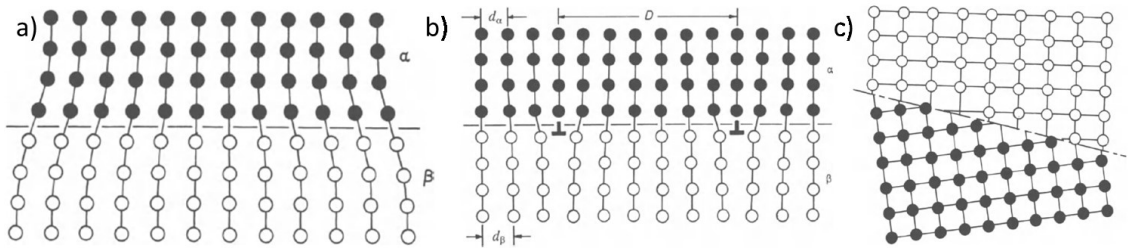

Figure 2.5. *a) Coherent, b) semicoherent and c) incoherent interface [9].*

In the case of coherent interface, the two lattices fit together perfectly while in semicoherent interphase the misfit between the two lattices is accommodated with dislocations. In noncoherent interphase, there is no possible way to match the two lattices. [9] When a dislocation moves through an interphase, it can either cut or bow, depending on the coherency of the interface and the size of the precipitate particle. Bowing by Orowan looping and cutting through a precipitate are illustrated in Figure 2.6. [10]

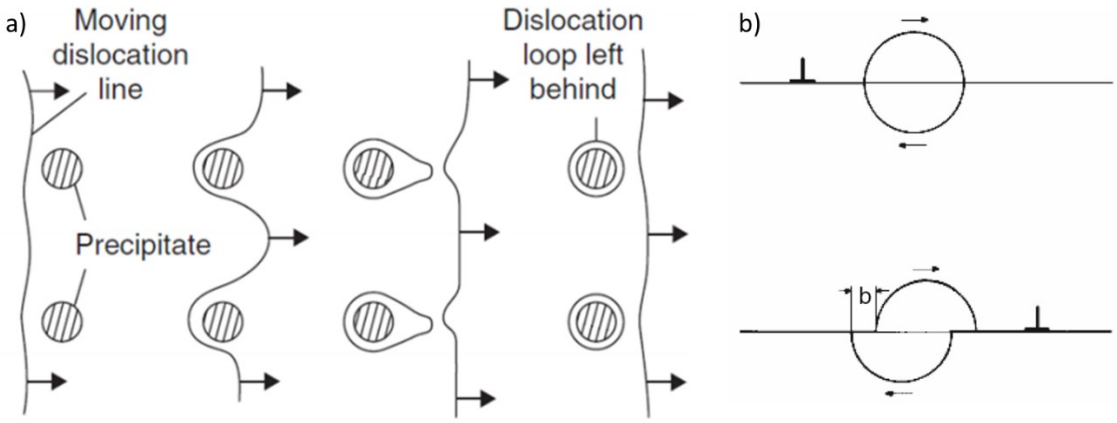

Figure 2.6. *a) Bowing [10] and b) cutting through a precipitate [11].*

The dislocation loop that is left behind the dislocation line makes it harder for next dislocations to move across the precipitates, since the effective distance between the particles decreases. The effect on work hardening of the precipitates depends on their size and the maximum strengthening is achieved with the critical particle size which is the particle size value at intersection of the bowing stress and cutting stress that are illustrated in Figure 2.7.

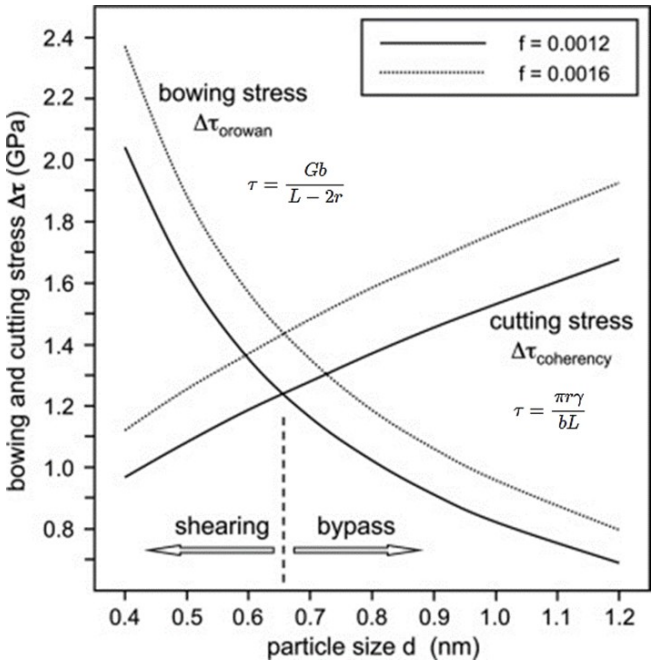

Figure 2.7. *Bowing and cutting stress as a function of particle size [12].*

Temperature also affects the rate of the diffusion that occurs in the material. Diffusion means the movement of atoms in a system [9]. It causes for example creep, dynamic strain aging and phase transformations. Diffusion of atoms only happens, if it lessens the internal energy of the system, Gibbs free energy. Diffusion movement in solid lattice alloys can happen in three ways, either substitutionally, interstitially or along grain boundaries. Interstitial atoms force their way between larger atoms, while substitutional atoms move by a vacancy mechanism. The movement of substitutional and interstitial atoms is illustrated in Figure 2.8.

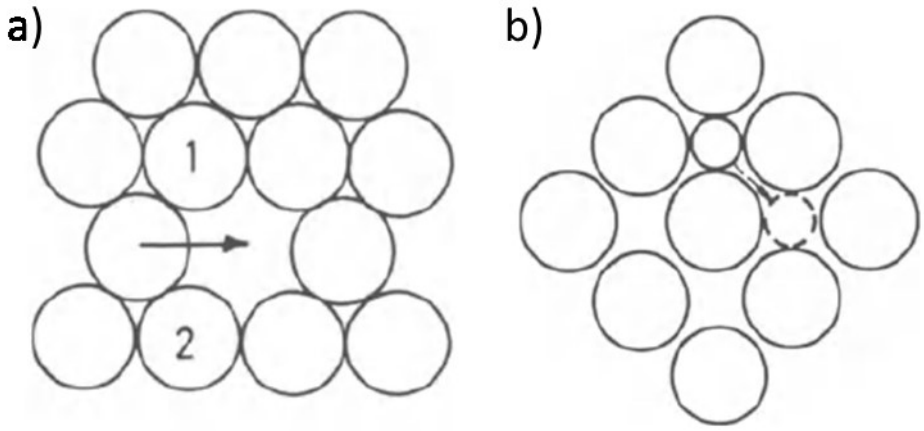

Figure 2.8. *a) Movement of a substitutional atom from one vacancy to another and b) movement of an interstitial atom [9].*

Diffusion increases in high temperatures due to the increased vibrational energy of atoms and the increasing number of vacancies that both are dependent on temperature. [9] Grain boundary diffusion is faster than the diffusion through the crystal and it becomes more important with decreasing temperature, when interstitial and substitutional diffusion are restricted due to the small thermal energy. Diffusion can be prevented with for example larger grain sizes and grain boundary precipitates.

At temperatures above Debye temperature which is the temperature when a crystal reaches its highest normal vibration [13] and at high strain rates, when the stress level in a material reaches the point when even the highest potential barrier is easy to overcome the dislocation drag turns to viscous and the stress – velocity dependence changes from non-linear to approximately linear and the dislocation speed is about few percent of the sound speed [14]. The dominating mechanism of dislocation drag is then the moving dislocations scattering off phonons, also called the phonon wind, instead of the dislocation forests. The phonon wind has been studied since the 1950's [15]. In this area, the dislocation drag coefficient and the average dislocation velocity increases as a function of stress applied to the material. Dislocation velocity can then even approach the transverse sound speed within the crystal. [16]

3 TURBINE ENGINES

The basic working principles of the turbine engines are presented in Chapter 3.1, and the different high temperature resistant materials used in the engines are presented in Chapter 3.2. These materials include nickel-based superalloys, steels, titanium alloys, ceramics, composites, and various coatings. The focus is on the nickel-based superalloys, since the material studied in the experiments is a nickel-based superalloy and other materials are revised only briefly. More information on the different materials and the materials selection for aerospace applications can be found in the book *Aerospace Materials and Applications* by Biliyar N. Bhat et al. [17].

3.1 Working principles of gas turbine engines

Basically, the jet engine is a type of a gas turbine engine. The engine can be divided in three parts: the compressor, the combustion chamber, and the turbine [18, 19]. The air flow through a gas turbine engine is presented in Figure 3.1.

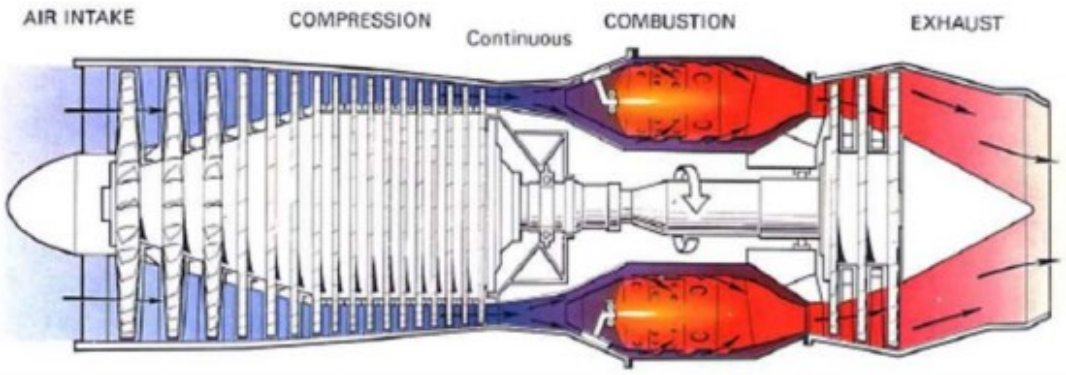

Figure 3.1. *The air flow inside a gas turbine engine [18].*

The compressor draws the air to the engine with multiple rows of blades that further pressurize the air [18, 19]. Each row of the blades in the compressor consists of a rotor and a stator, which are made of multiple blades and vanes that compress the air and increase its temperature [18]. Then the hot and pressurized air reaches the combustion chamber, where it is mixed with fuel, and the gas mixture is ignited with a spark causing the gas to expand and the temperature of the gas to rise further [18, 19].

Next the gas reaches the turbine, which is between combustion and the exhaust sections of the engine, as can be seen in Figure 3.2. [18, 19] The turbine section has several stages, some of which rotate, while some are fixed. The fixed ones convert the kinetic energy of the gas to mechanical energy by redirecting the gas to rotate the turbine. The

rotating part of the turbine is called the turbine rotor and it consists of turbine blades. [18] The temperature of the gas mixture drops to 700 °C when entering the turbine, while in the combustion chambers the temperature can be even over 1500 °C [1].

3.2 Materials for turbine engines

Gas turbine engine materials have many restrictions and requirements, due to the high temperatures and high stresses inside the turbine engines. Figure 3.2 presents the different parts of a turbine engine and the most typical materials used in them.

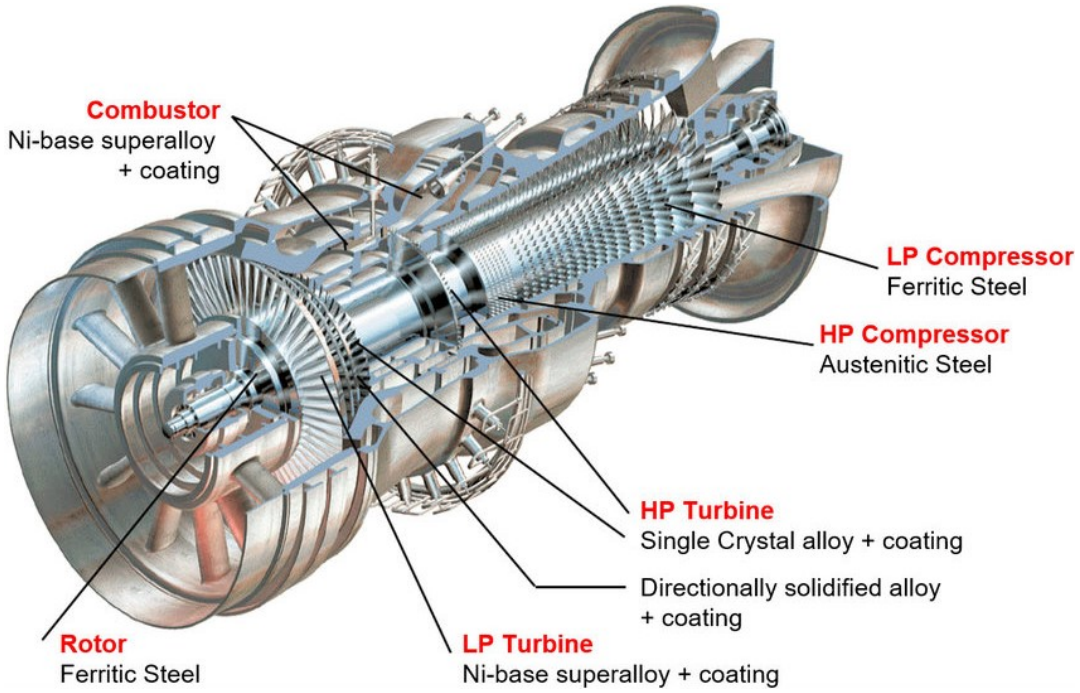

Figure 3.2. *The turbine engine parts and the suitable materials for each part [20].*

For example, the materials need to have a high creep resistance, but also high yield strength, fatigue strength, and corrosion resistance [1, 21]. The manufacturing aspects of the components have to also be considered when determining the materials [21]. As noted above, for the turbine blades, the operating temperatures typically can go as high as 700 °C [1].

3.2.1 Nickel superalloys

Nickel has an FCC crystal structure and the nickel-based superalloys consist of this FCC gamma (γ) matrix with gamma prime (γ') precipitates, also called a superlattice [22]. These structures are presented in Figure 3.3.

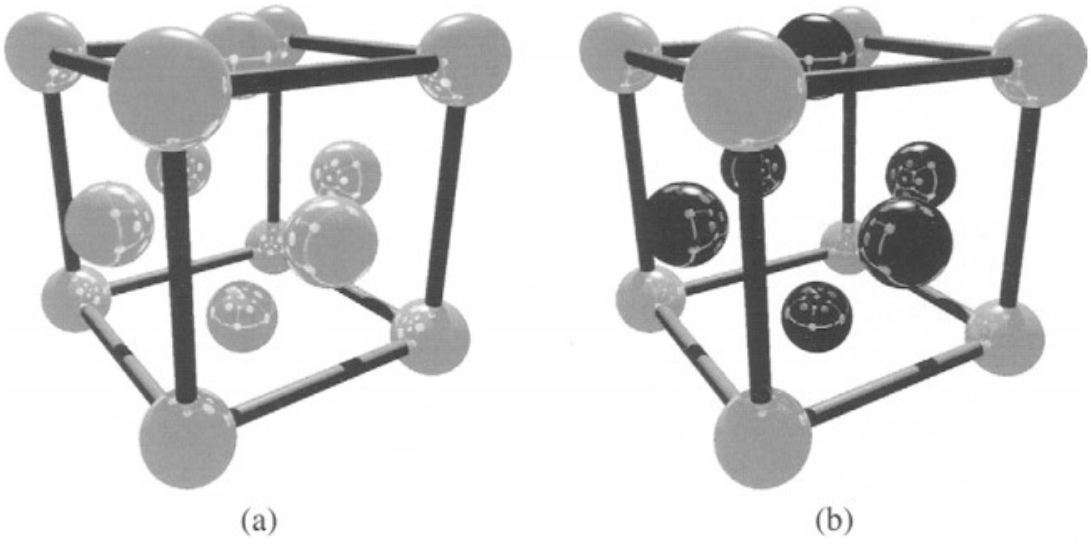

Figure 3.3. *The structure of a) FCC crystal lattice and b) FCC crystal lattice with γ' precipitates, also called the superlattice [22].*

As discussed in Chapter 2, the main thermally activated mechanism in FCC lattices are the other dislocations, which contribute to the yield strengths [23]. In nickel-based superalloys, the superlattices are one of the main reasons behind the strength. The precipitates and matrix are coherent [24]. The strengthening effect is due to two reasons. Firstly, the order hardening occurs when the ordered lattice structures of the precipitates slow down the dislocation movement when the dislocations need to cut through them. When the dislocations move from gamma phase to gamma prime phase, antiphase boundaries are formed. [25, 26] The formation of an antiphase boundary is presented in Figure 3.4.

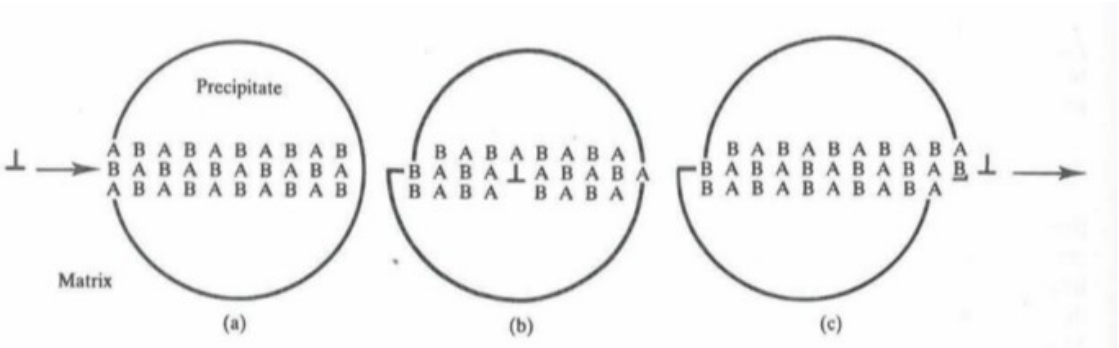

Figure 3.4. *Formation of an antiphase boundary [25].*

The second effect of the superlattice is the lattice mismatch between the phases that causes long-range coherency stresses. These stresses slow down the dislocation movement even further. [26]

In gas turbine engines, nickel-based superalloys are typically used in the combustors and the turbines, due to their temperature resistance [1, 18, 20, 21]. Inconel 718, a Fe-

Ni-based superalloy, is the most used nickel superalloy in the world, due to its excellent mechanical properties in elevated temperatures [21]. Inconel 718 has a superlattice also, but instead of γ' precipitates, it has gamma double prime (γ'') precipitates, that give even better mechanical properties than gamma prime precipitates. However, Inconel 718 cannot be used in the parts operating in the highest temperatures since the γ'' precipitates are unstable at temperatures over 650 °C [24].

However, nowadays in the turbine blades typically single crystal blade alloys, also CMSX-4 alloys are used due to their really high temperature resistance. Turbine blades typically encounter a lot of creep due to the high temperatures and can face plastic deformation even before yield strength. One way to enhance the high temperature endurance of turbine blades is by changing the grain size and shape. [1, 18] Three differently solidified turbine blades are presented in Figure 3.5.

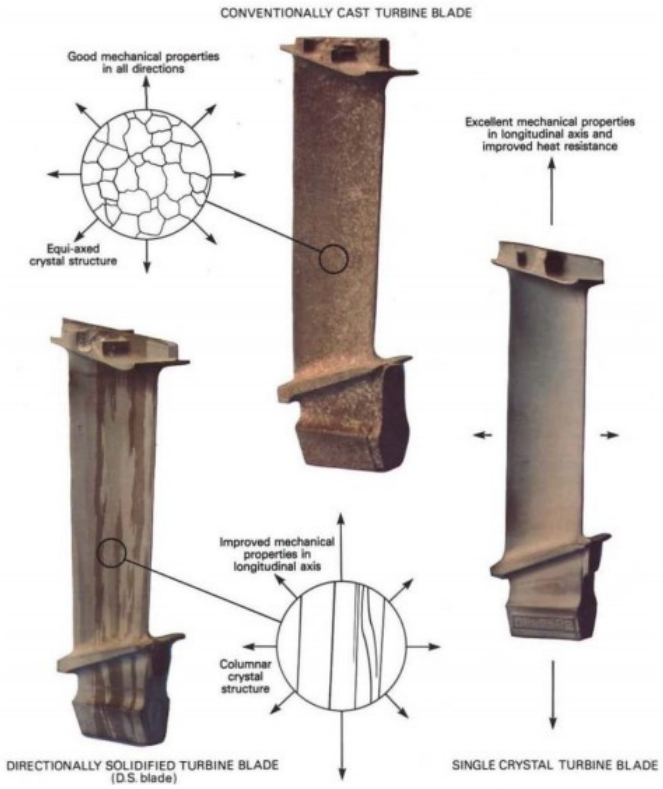

Figure 3.5. *Polycrystalline, directionally solidified and single crystal turbine blades [18].*

With directional solidification, less creep occurs than with conventionally casted polycrystalline grain structure, since there are less grain boundaries [1, 18]. However even better results can be achieved with a single crystal structure, since it eliminates the grain boundaries altogether and increases the possible operating temperature of the component around 50 °C when compared to polycrystalline grain structure [1, 18]. Nowadays

typically only single crystal structures are used in the applications that operate at the highest temperatures [22].

The mechanical properties of a material in a high temperature can be divided into three groups: short- and long-term mechanical properties and hot corrosion resistance [1]. Short-term mechanical properties include yield strength and ductility and are the focus of this thesis. Fatigue and creep are long-term mechanical properties.

The different strengthening mechanisms of nickel superalloys are presented in Figure 3.6.

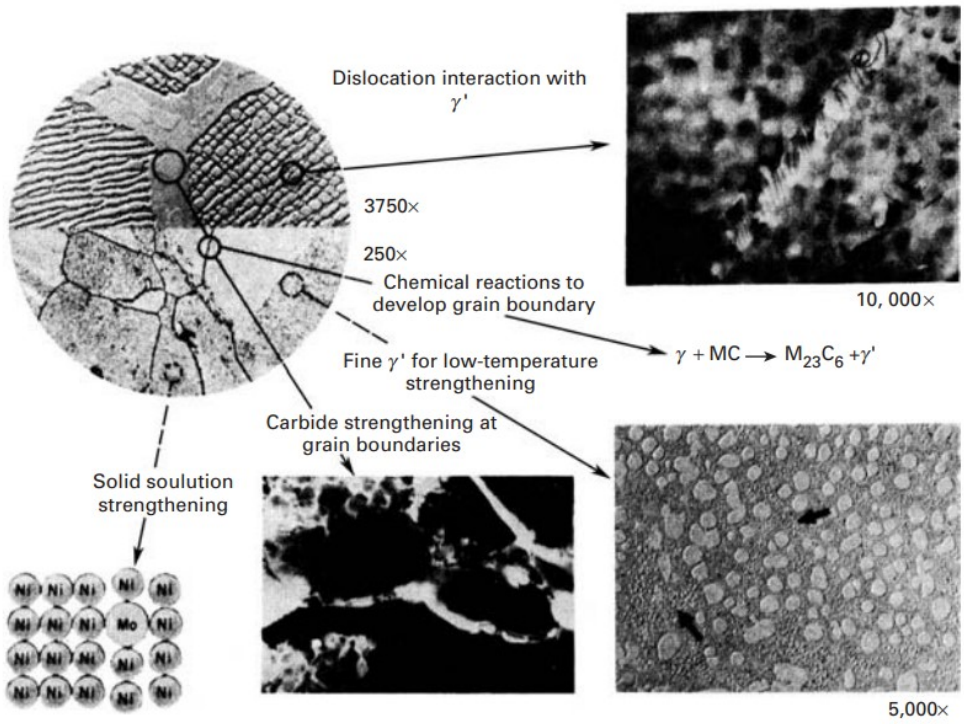

Figure 3.6. *Different microstructural strengthening mechanisms of nickel superalloys [1].*

The different strengthening methods for nickel-based superalloys include solid solution strengthening, forming carbides at grain boundaries, and forming precipitates. Different alloying elements are used for the different strengthening mechanisms [1]. Superalloys are also usually heat treated before usage [21].

In the experiment by Balikci et al. [27], the effects of precipitate size on the tensile properties and strain hardening in different temperatures and with different strain rates were analysed. Figure 3.7 presents the yield strengths and ultimate tensile strengths of the different materials as a function of temperature of the experiment.

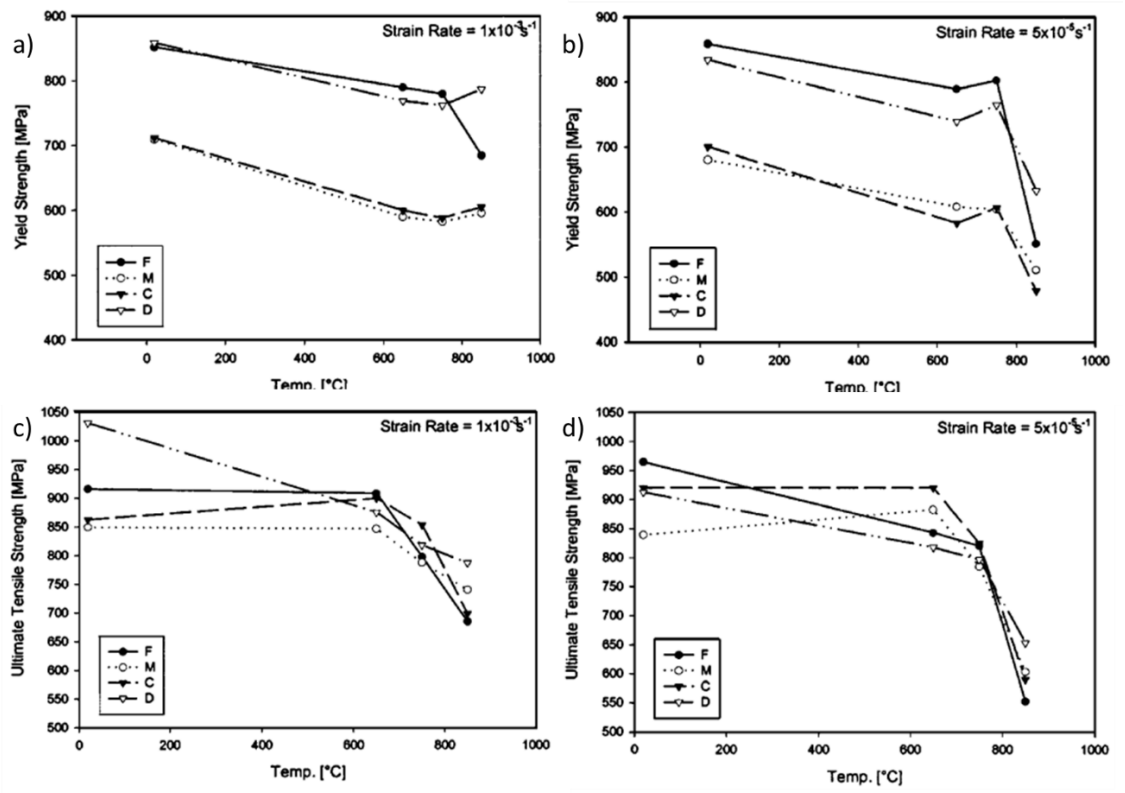

Figure 3.7 *The effect of precipitate size on yield strength and ultimate tensile strength [27].*

The different alloys contained fine (F), 70 nm, medium (M) sized, 450 nm, coarse (C), 700 nm, and duplex (D), 50 nm and 450 nm, precipitates. As can be seen in Figure 3.7, at low temperatures the fine precipitates strengthen the material the most, since the highest yield strengths and ultimate tensile strengths are achieved with the alloys F and D, which both included fine precipitates. However, when the temperature increases, the ultimate tensile strength of the alloys decreases significantly at both strain rates. The yield strengths of these alloys also decrease with increasing temperature at the lower strain rate of $5 \cdot 10^{-5}$ 1/s, but at the strain rate of 10^{-3} 1/s the drop in strength is not as significant. At temperatures around 700-800 °C, the alloy with coarse precipitate size has the highest ultimate tensile strength at both strain rates.

The strain hardening exponent (n) of the nickel superalloys as a function of temperature and at two different strain rates is presented in Figure 3.8.

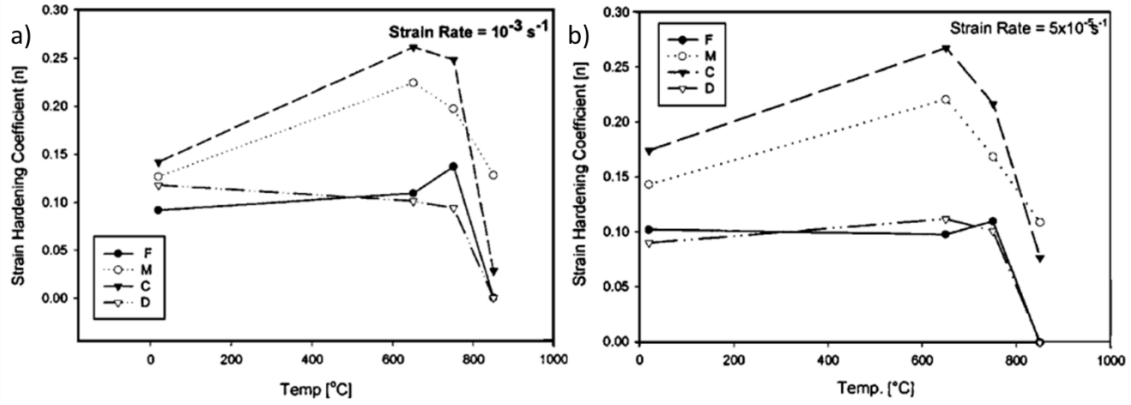

Figure 3.8. *The effect of precipitate size on strain hardening exponent [27].*

As can be seen in Figure 3.8, the alloys with the coarse precipitates strain harden the most at elevated temperatures. This is due to the athermic nature of these extended precipitates and their ability to block the dislocation movement. At higher strain rates, the strain hardening exponent of the alloy with coarse precipitates also holds at higher temperatures better. In addition to the lower probability of the dislocation movement that was explained in Chapter 2, the increasing strain rate is also noticed to increase the dislocation density in the nickel-based superalloy studied by Balicki et al [28].

All in all, nickel-based superalloys are used at high temperatures due to their good temperature resistance, which is achieved with both the FCC crystal structure but especially with the high amount of large precipitates [22]. The precipitates hold the mechanical properties at high temperatures in two ways: carbides strengthen the grain boundaries to reduce diffusion and improve the creep resistance, and other precipitates block the dislocation movement inside the grains, even in high temperatures. The precipitates also prevent creep deformation in intermediate temperature range around 800-1000 °C [22]. Nickel superalloys also typically have higher ultimate tensile strengths in elevated temperatures, around 500-800 °C, than at room temperature due to the fact that the large precipitates increase the strength by strain hardening at higher temperatures [29-31].

3.2.2 Steels

Steels are attractive to aerospace applications because they have high fracture toughness and they can achieve really high strengths with heat treatments. In aerospace applications, stainless steels are typically used due to their good corrosion resistance. In the turbine engines, steels are typically used in parts, where the temperatures are not the highest: in the compressor and at the other end, the rotor [20]. In high pressure compressor, austenitic stainless steels alloyed with chromium and nickel are used [20, 21].

In low pressure compressor and rotor, ferritic stainless steels that typically contain high amounts (up to 18 %) of chromium are used.

3.2.3 Titanium alloys

Titanium is widely usable in different applications due to its high strength, low density and corrosion resistance, but the development of titanium is still in the beginning and it is mostly used in the aerospace industry. However, its rather high price explains the minute usage of titanium in for example automotive industry. Figure 3.9 shows the tensile properties of Ti-64 titanium alloy compared to other aerospace structural metals.

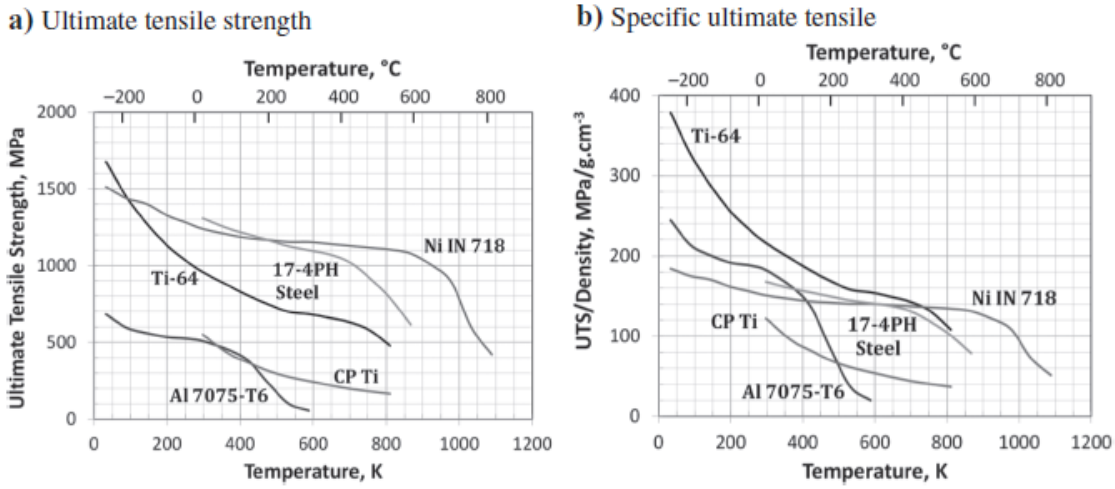

Figure 3.9. *Strength of the Ti-64 titanium alloy compared to other aerospace structural metals [21].*

Specific ultimate tensile strength is the ultimate tensile strength divided by the density of the material. At temperatures above 500 °C only the Inconel 718 has higher specific ultimate tensile strength than the titanium alloy. At lower temperatures the titanium alloy has the highest specific ultimate tensile strength. Titanium is typically strengthened by precipitation hardening and solid solution hardening [32].

3.2.4 Other materials

Different ceramic materials can be used as environmental barrier coatings to enhance the temperature and corrosion tolerance of the components of turbine engines. Ceramic coatings can be difficult to use, because they have different coefficient of thermal expansion with the base metals. One used solution for this problem is an intermediate layer between the coating and the base metal.

Typically, nickel-based superalloys used in the turbine engine combustors and turbines are coated for improved corrosion and oxidation protection [21]. First, the parts are aluminized, meaning that they are subjected to vaporized aluminium to form nickel-aluminium alloy layer. To further improve the corrosion resistance also cobalt, chromium, yttrium and platinum can be added to the coating. The last layer added to the components is a thermal barrier coating, which is typically the ceramic yttria-stabilized zirconia coating. Zirconia is suitable as a thermal coating since its melting point is really high, around 2700 °C, it's has low thermal conductivity, and it has relatively high thermal expansion coefficient. [21]

Nickel superalloys are starting to reach their limit with the development of the temperature properties [21] and a proposed alternative for them are the SiC/SiC ceramic matrix composites. They have low density, good oxidation resistance, and their creep resistance is high. However, they need environmental barrier coatings to prevent the rapid strength degradation that happens when the protective silica layer volatilizes when exposed to water. [21]

4 DYNAMIC TESTING OF MATERIALS

Different methods of dynamic material testing methods are presented and discussed in this Chapter. The focus is on Split Hopkinson bar, since it's used in the experimental part of the thesis, but the Taylor anvil and the expanding ring methods are also presented briefly.

4.1 Split Hopkinson bar

Split Hopkinson bar was first introduced by Kolsky in 1949 [33]. With the Split Hopkinson Bars, or Kolsky bars, strain rates roughly in the range of 10^2-10^4 1/s can be achieved [34]. There are compression, tensile, and torsion split Hopkinson bars and both brittle and ductile materials can be tested with them [34].

The Split Hopkinson Pressure Bar (SHPB) is the conventional and most used of the Hopkinson bar devices [35]. Figure 4.1 shows a schematic picture of a split Hopkinson pressure bar.

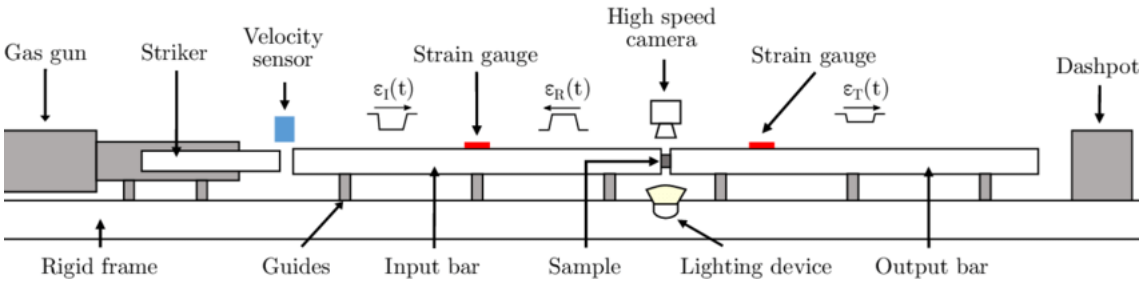

Figure 4.1. *Schematic picture of a split Hopkinson pressure bar [36].*

SHPB system consists of three bars: a striker bar, also called a projectile, an incident bar, also known as an input bar, and a transmitter bar, sometimes referred to as an output bar. There's also a gas gun that accelerates the striker bar towards the incident bar, and strain gages that measure the stress pulses generated by the impact of the striker bar to the incident bar [34, 35]. The impact of the striker bar with the free end of the incident bar creates a uniaxial stress pulse to the incident bar, called the incident pulse. The pulse travels first through the incident bar and then transmits through the sample to the transmitter bar creating the transmitted wave. The specimen is sandwiched between the incident and transmitter bars and it experiences plastic deformation as the pulse travels through it. [34] The elastic wave is long compared to the length of the specimen and the wave propagation in the specimen is not taken into account in the calculations. Part of the elastic wave reflects back to the incident bar creating the reflected wave.

[34, 35, 37] The movement of these waves in the setup is illustrated in Figure 4.1 and an example of the strain amplitudes as a function of time is shown in Figure 4.2. In each type of split Hopkinson bars, the waves are the same: incident (ε_i), transmitted (ε_t), and reflected (ε_r). The impedance difference between the bar material and sample material causes the transmitted wave to differ from the original incident wave [24, 25]. The impedance difference generates the reflected wave.

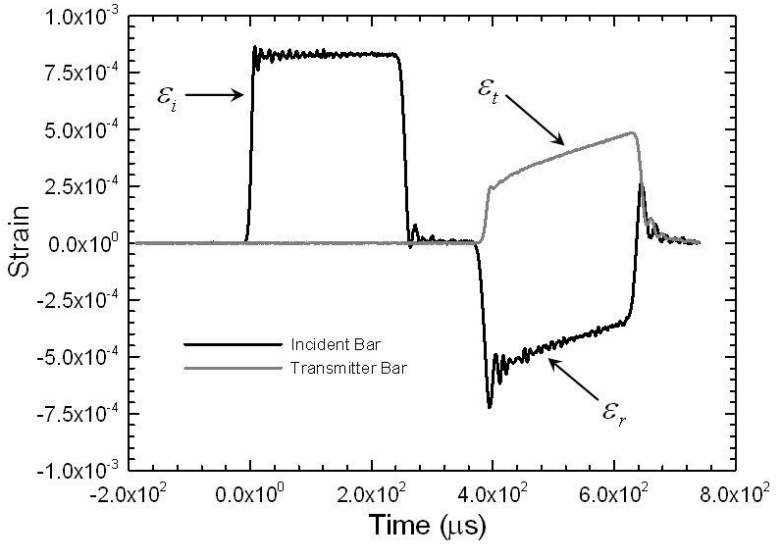

Figure 4.2. *The stress pulses in a split Hopkinson bar test [38].*

The stress-strain response of the sample can be calculated from these three pulses [34]. The calculations are presented in Chapter 5.3. In addition, a high-speed camera can be added to record images of the test, so that the strains can be calculated from the videos to ensure the accuracy of the calculations [36, 39-43]. From the videos, the success of the test can also be checked, since the test is too fast for visual observation of human eye.

One possible setup for the split Hopkinson tensile bar (SHTB) also has incident and transmitter bars, but instead of striker bar it has a striker tube that causes a tensile pulse to the incident bar [34, 44, 45]. The SHTB used in the experiments of this thesis uses a striker tube to produce the tensile pulse. A schematic picture of this type of SHTB is presented in Figure 4.3.

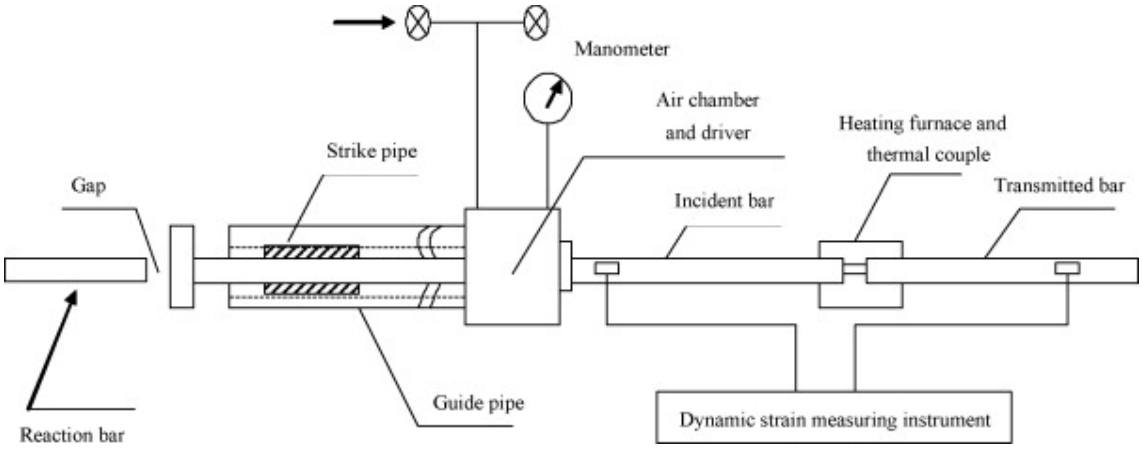

Figure 4.3. *Schematic picture of a split Hopkinson tensile bar [44].*

The SHTB, as its name says, is a tensile test. The incident bar moves backwards with the tensile wave and pulls the specimen away from the transmitted bar causing tensile strain in the specimen [34, 37, 45]. If the sample doesn't break with the loading, the waves keep travelling back and forth and the sample experiences loading, which makes recovery tests difficult [37], but Nemat-Nasser et. al [46] has proposed a wave trapping method that is widely used [34, 37].

There are also numerous other methods to carrying out tensile testing with split Hopkinson bars, in addition to the one presented in Figure 4.3 and in Figure 4.4 d). Some of them can be seen in Figure 4.4 a)-c).

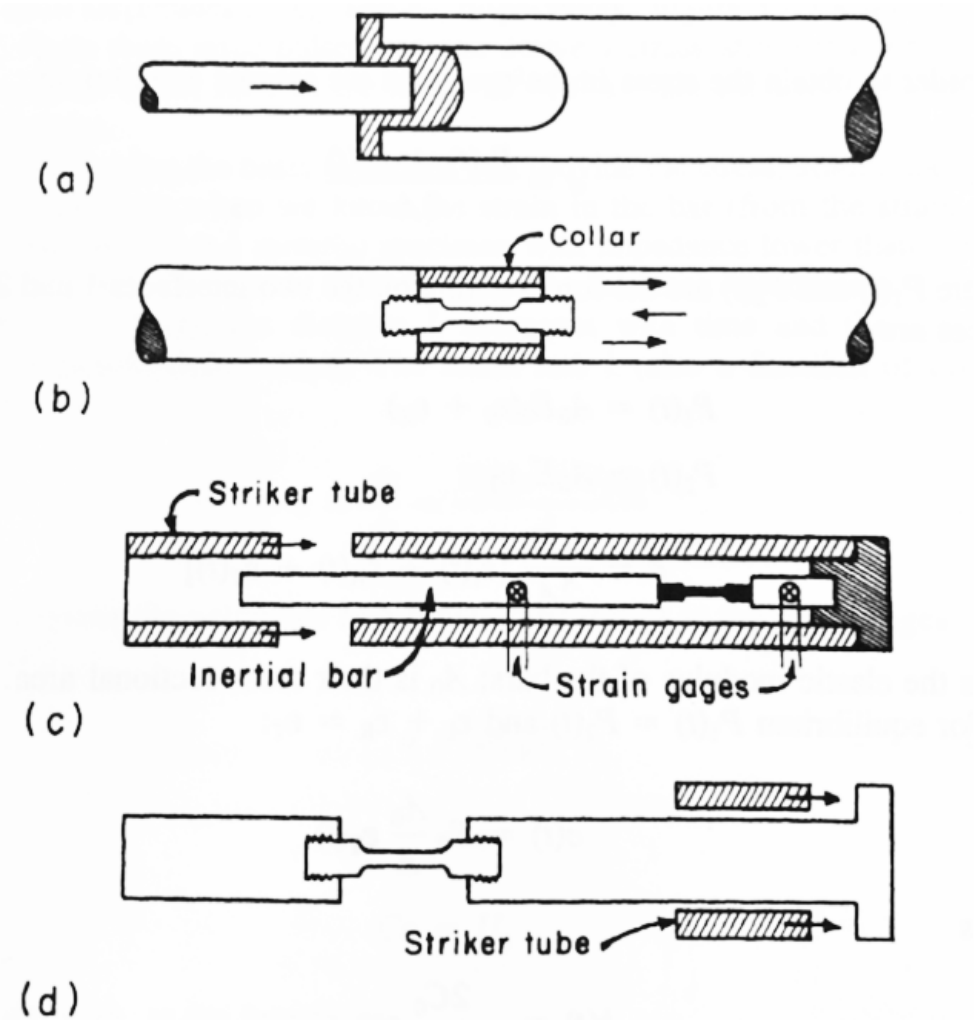

Figure 4.4. *Different methods to execute a split Hopkinson tensile test: a) a hat-shaped specimen, presented as the shaded part of the picture, b) a collared specimen, c) an inertial-bar setup and d) collar impacting bolt head [34].*

The hat shaped specimen was first introduced by Lindholm and Yeakley in 1968 [47]. The incident bar, on the left in Figure 4.4 a), hits the hat-shaped specimen from the left and sandwiches the sample between itself and the hollow transmitted tube causing tensile strain to the gage section of the specimen [45]. With the collared specimen presented in Figure 4.4 b), the compression does not affect the specimen due to the collar and the compression wave returns as a tension wave to the specimen [34, 45]. The collared specimen was first introduced by Nicholas in 1981 [48]. With the inertial setup presented in Figure 4.4. c), the striker tube causes a compression wave to the main tube, which pulls the specimen to the right. The tension pulse is created when the inertial bar counteracts the movement to the right. [34] This method was first presented by Hauser in 1966 [49].

Torsional split Hopkinson bar (TSHB) impacts a torsional force to the specimen and gives a shear stress – shear strain data as a result [34, 45, 50, 51]. TSHB was first introduced

by Baker and Yew in 1966 [51]. A schematic picture of a torsional split Hopkinson bar is presented in Figure 4.5.

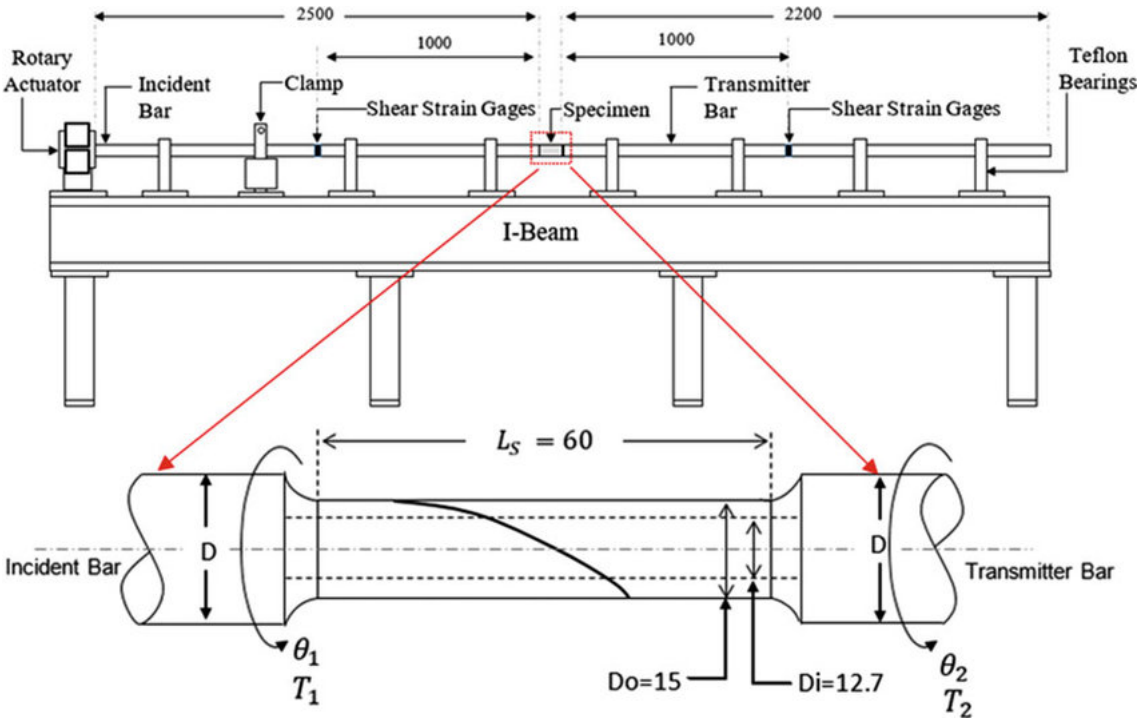

Figure 4.5. *Schematic picture of a torsional split Hopkinson bar and a spiral notch specimen mounted into place [50].*

TSHB consists of incident and transmitted bars, shear strain gages, and a system to produce a dynamic torsional load [34, 45, 50, 51]. In order for the test to be dynamic, a torsional load needs to be released suddenly. One way to generate a dynamic torsional load is by braking a clamp that holds the incident bar in place after torsional load has been generated by a rotary actuator to the end of the incident bar [34, 50, 52]. This method is called prestored energy loading [53]. Other loading methods in TSHB are for example explosive [54], direct [55], flywheel [56], and electromagnetic [57] loading. The explosive loading has two small explosive charges on either side of the incident bar, that are detonated simultaneously [54]. Direct impact load can be generated with an impact pin attached to the end of the incident bar [55]. In the flywheel loading, a flywheel is accelerated to a desired speed with a motor. After this, the flywheel can be detached from the motor and attached to the incident bar with a magnetic force while the flywheel is rotating. [56] In the electromagnetic loading, a strong magnetic field is generated to rotate the incident bar with desired speed [57]. When applying torsion to the incident bar, it needs to be confirmed that the deformation of the bar stays completely in the elastic area [51]. Shear stresses can also be achieved with a hat shaped specimen in compression [34].

Different kind of samples are needed for the different split Hopkinson bar types. With the SHPB the sample geometry is the most free, since the samples do not need to be mounted to the bars [34]. Typically, with SHPB, cylinders, discs, or ring-shaped samples are used [55, 58]. Various ductile metallic [43, 59-66] and polymeric [67, 68] materials can be tested with Hopkinson pressure bar, as well as different composite materials [69, 70].

In addition, really soft materials can be tested with the SHPB [71]. These soft materials include for example PMMA [61], different foams, rubbers and rubber-like polymers, such as gel rubber samples [55], and also different biological tissues [71]. The challenging aspect of soft material testing with the SHPB is the low acoustic impedance of the materials, which with high strain rates easily causes the stresses and strains to be non-equilibrium and non-uniform [71].

Of the brittle materials, concrete has been widely tested with SHPB both in elevated temperatures [72-76] and in room temperature [58]. Also, rocks can be tested with both pressure and tensile split Hopkinson bars [77]. Ceramics can also be tested with SHPB setup [78]. When testing brittle samples with SHPB, the pulse needs to be shaped with a pulse shaper, which is a pad made of a soft material, for example copper, cardboard, rubber or a combination of the former, placed between the striker bar and the incident bar [34]. The pulse shaper increases the rise time of the wave since without it the brittle samples can break with very small strains during the first reverberations of the wave. With brittle materials, the stresses can concentrate locally since they are not able to yield locally [79]. Different specimen types to reduce the local stresses are presented in Figure 4.6.

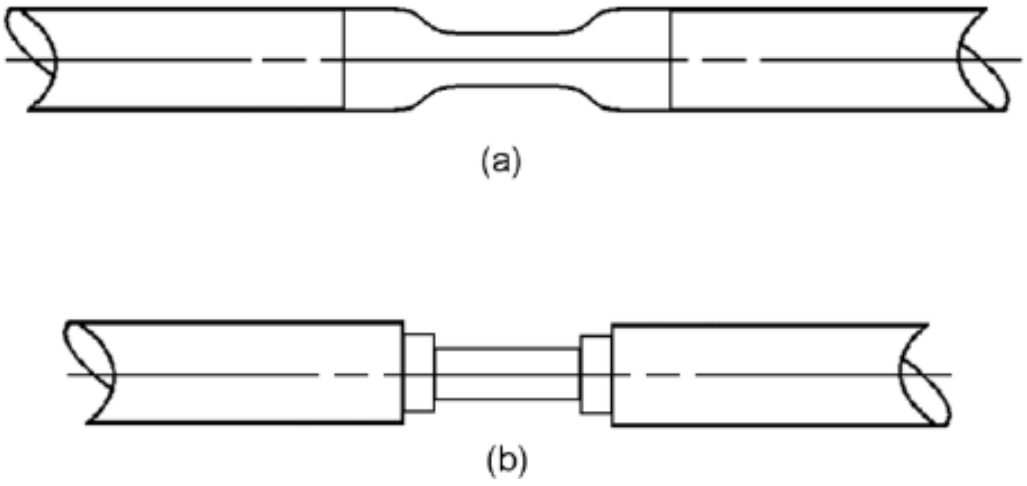

Figure 4.6. *Stress concentration reducing sample types: a) Dumbbell shaped and b) hard platens on both sides of the sample [79].*

With SHTB, different metals [37, 39, 41, 42, 80-86], polymers [44, 87-89], composites [90-93], brittle materials like concrete [94] and also biological materials [95] can be tested. Different shapes and mounting methods of the samples have been used in Hopkinson tensile tests. For example, sheet metal samples can be bolted to the incident and transmitted bars [82], an example of which is presented in Figure 4.7.

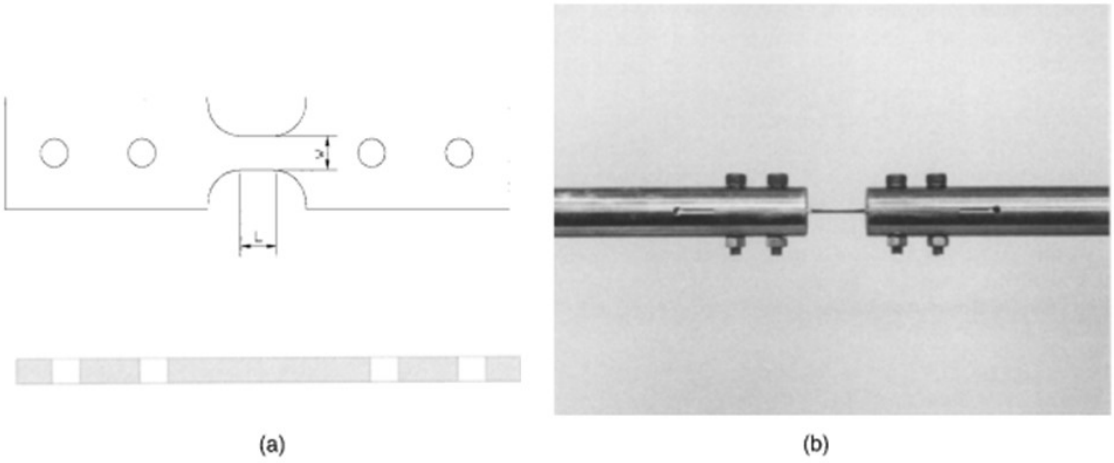

Figure 4.7. *A sheet metal SHTB sample: a) the schematic picture and b) the sample mounted to the bars with bolts [82].*

Other possible mounting methods are gluing the sample to the bars [77, 80, 81] and screwing the sample into place with treads [37, 44, 85, 86]. Another possible mounting method for a SHTB sample [83] is presented in Figure 4.8.

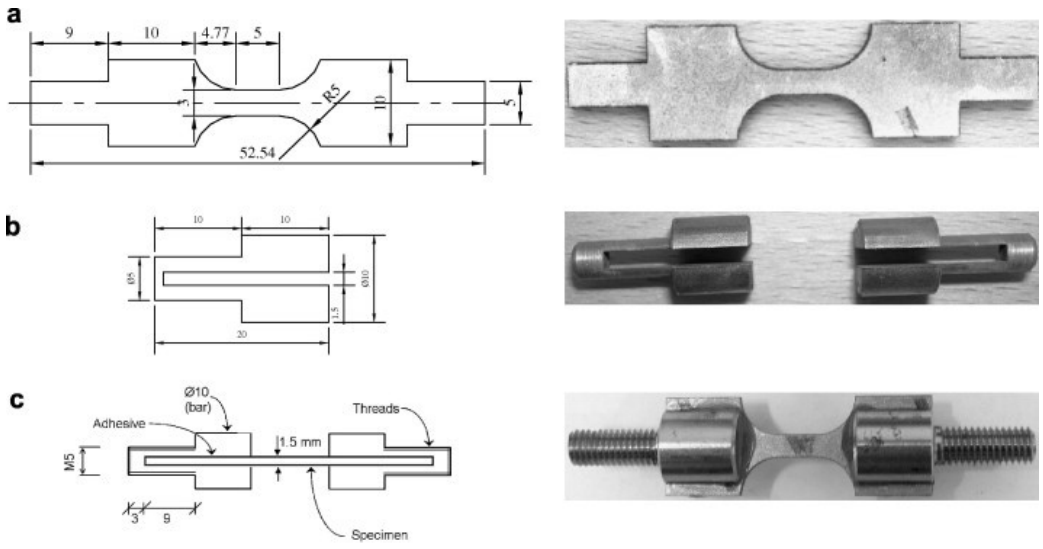

Figure 4.8. *One possible sample mounting type in SHTB [83].*

The metal sheet sample is glued to the two grips at both ends, after which the ends are machined to a screw-shape and screwed to the bars [83].

In torsional tests, the sample can be attached for example by silver brazing [51], epoxy cementing [54, 96], with a geared steel adapter [55], or with hexagonal sockets at the end of the bars in which the sample with hexagonal flanges fits [52]. The hexagonal ended sample is presented in Figure 4.9

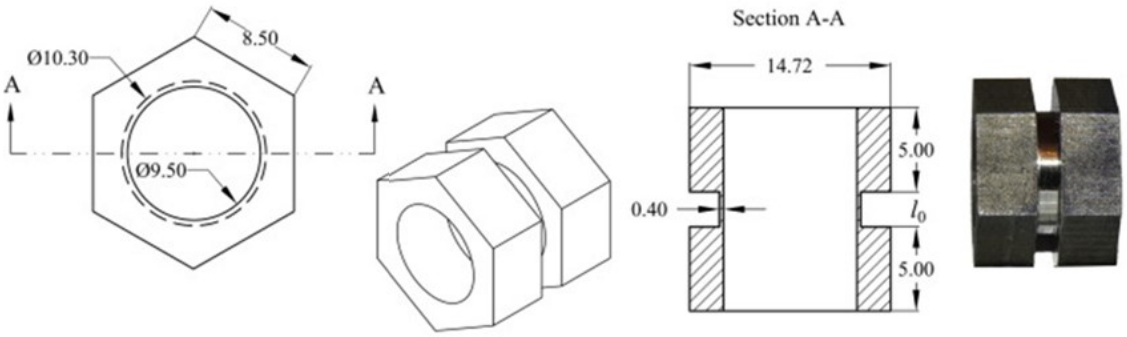

Figure 4.9. *Thin-walled tubular samples for TSHB tests [52].*

The samples are typically tubular samples with either hexagonal or cylindrical flanges, meaning that their middle part is thinner than the ends [53]. Various metals can be tested with TSHB setup [5, 48, 50, 52, 54, 96-99], but also softer, gel-like materials have been tested with a special setup [55]. A pulse shaper can also be used in TSHB tests if necessary [53].

4.1.1 High temperature split Hopkinson bar tests

In this chapter, the specifics of high temperature split Hopkinson bar tests are presented, including the things that need to be considered before the tests, the problems as well as the solutions to these problems are discussed. One possible setup for high temperature SHPB tests is shown in Figure 4.10.

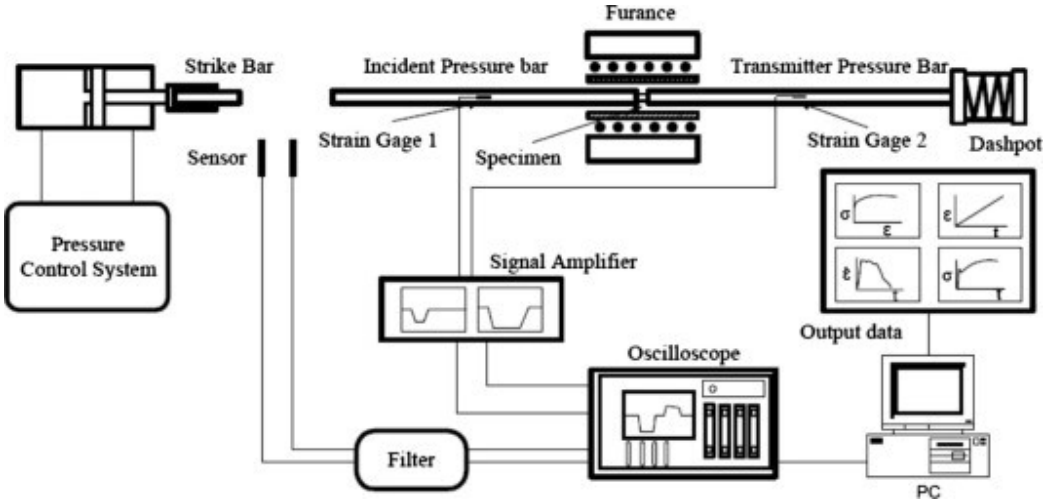

Figure 4.10 *A setup for high temperature SHPB tests [100].*

When testing materials with split Hopkinson bars in elevated temperatures, it is important to make sure, that the incident and transmitter bars stay in room temperature, since any temperature gradients in the elastic bars change the elastic constants which then leads to a change in the mechanical properties of the bar material and affects the wave propagation in the bars [37, 60, 62, 101-104]. In addition, the microstructure of the sample can be affected by the heating if it's not done carefully [60]. The heating of the samples is carried out for example by heating it in a furnace [37, 93, 100-103, 105-109], using induction heating [39-42, 104, 110, 111], with a heating tape [112], using a heat gun [113], with resistive heating plates [114], automatic microwave heating [72] or using infrared (IR) spot heaters [62, 67, 104]. One setup for an infrared spot heater is shown in Figure 4.11.

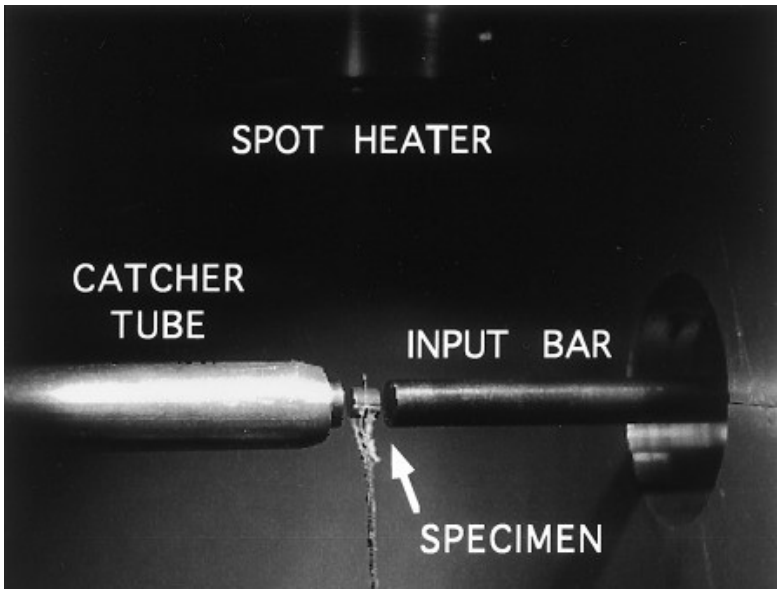

Figure 4.11 *Sample position and IR spot heater in high temperature SHPB setup [62].*

Induction heating is considered efficient in heating of the samples because it is fast, enables the localization of the heated volume, and heating without a physical contact [41, 111]. Different furnace types are resistance-heated [109] and electric [37, 100].

The temperature of the sample is traditionally measured with a thermocouple [62, 110, 112]. In the experiment carried out by Lemanski, Petrinic and Nurick [113], the temperature of the air of the heat gun was measured with a thermocouple and the temperature of the sample was determined by finite element modelling. This was done to eliminate the possibility of the measuring of the temperature having an effect on the results. Another option to measure the temperature without contact is to use a pyrometer [42] or IR thermography [115].

To avoid the bars from heating during SHPB tests, the most used technique is the one introduced by Nemat-Nasser and Isaacs [102], where the bars are kept outside of the furnace and put to contact immediately before the test took place and it, or a slightly modified version of it, has been used widely [103, 104]. Other methods are for example by providing a narrow insulating layer made from impedance-matched ceramic, for example aluminium oxide [111] or by applying thermal protective coating [37]. In the experiments of Lee and Tang [100], the bars were allowed to heat and the changes in the elastic modulus and the velocity of the pressure pulse were taken into account when calculating the results. The same method was used by Chiddister and Malvern in 1963 [116]. The calculation methods can be used to tensile and torsional Hopkinson bar as well.

When the sample is moved from the furnace to the target position, it is important to consider the cold contact time, CCT, which is defined as the time the sample is in contact with cold bars before the stress wave arrives [60, 117]. According to Li et. al [60], the CCT should be shorter than 50 ms for the experimental data to represent the true material behaviour. Shazly et al. [104] solved the problem of CCT with SHPB by sandwiching the sample with 2 WC inserts, whose impedance matched the one of the bars, which means that the waves are not disturbed by them. The WC inserts can be seen in Figure 4.12.

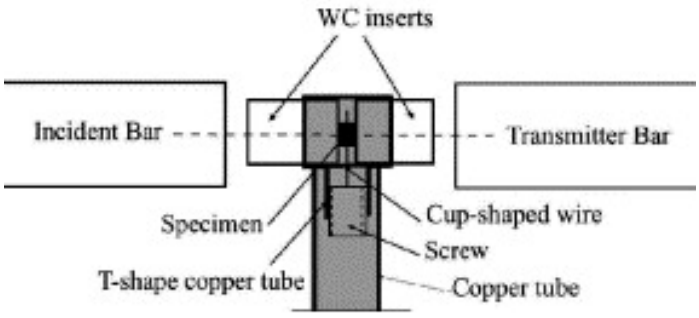

Figure 4.12 *WC inserts on both sides of the sample in a SHPB test [104].*

When the sample is brought to contact with the bars, the inserts lose the heat, keeping the temperature of the sample in the desired level [104]. In the experimental setup of high temperature SHPB of Lennon and Ramesh [62], the bars were brought to contact with the sample by an electropneumatic actuation system that can be seen in Figure 4.13.

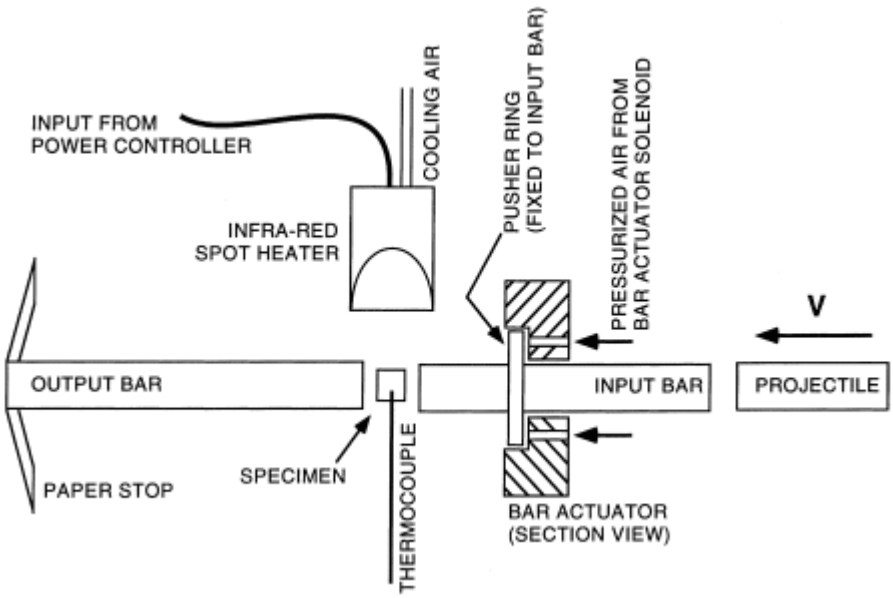

Figure 4.13 *An electropneumatic actuation system of a high temperature SHPB [62].*

The manipulation of the bars is controlled by an electronic delay circuit, which enables the cold contact time to be as short as possible. The delay time needs to be estimated correctly prior to the test since too short delays lead to bars coming to contact with the sample after the wave has passed, but too long delays make the cold contact time longer. The two values affecting the length of the delay are the projectile traveling time and bar closure time. [62]

With SHTB, high temperature testing is more difficult since the sample needs to be attached to the bars during the test [101]. The problem has been solved for example replacing the ends of incident and transmitter bars with Inconel 718 inserts [104] presented in Figure 4.14, with the Quick Hook Joint Method [101] presented in Figure 4.16, by cooling the bars attached to the heated sample with a cooling system [93] shown in Figure 4.17, using dry ice on the bars [112] or ceramic insulating tubes that surround the bars [108].

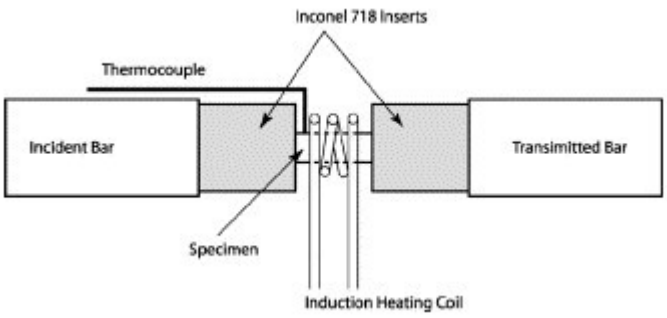

Figure 4.14 *Heating coil and Inconel 718 inserts in a SHTB test [104].*

In Figure 4.15 a picture of a non-contact heating coil for SHTB is presented.

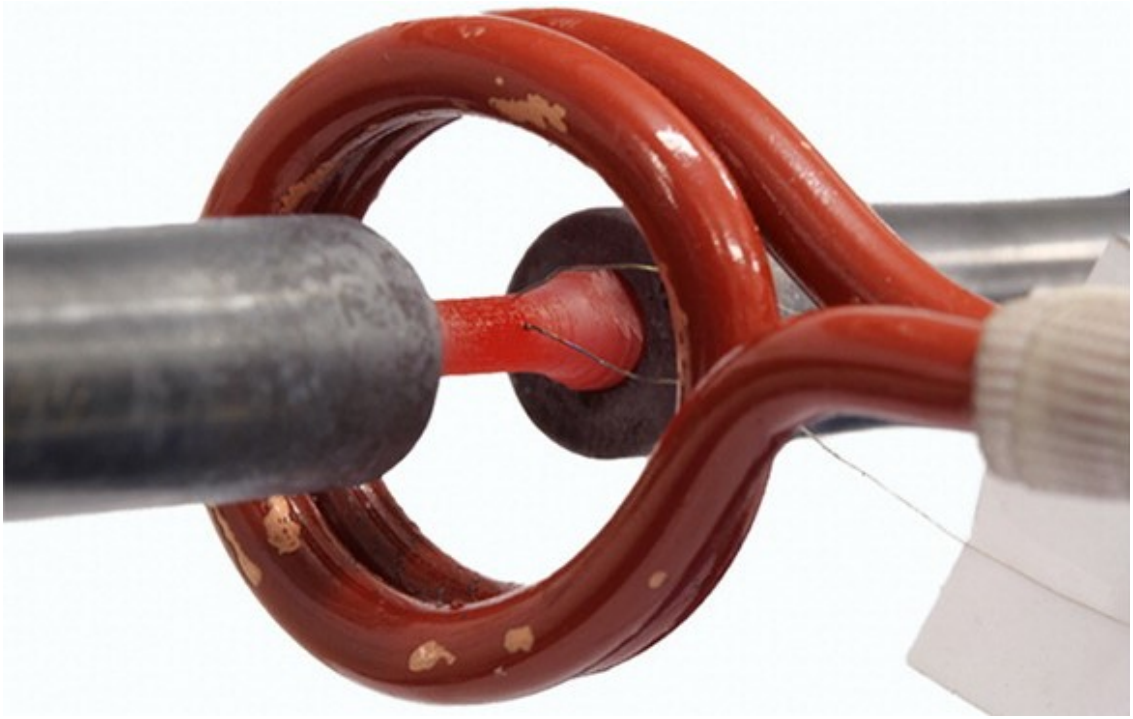

Figure 4.15 *A non-contact induction coil [110].*

In the Quick Hook Joint method, the sample is heated in a furnace and the bars are kept outside of the furnace. After the sample has reached the desired temperature, it is pushed to the target position and mounted by pneumatic actuators immediately before the arrival of the stress wave [101]. The Quick Hook Joint is illustrated in Figure 4.16.

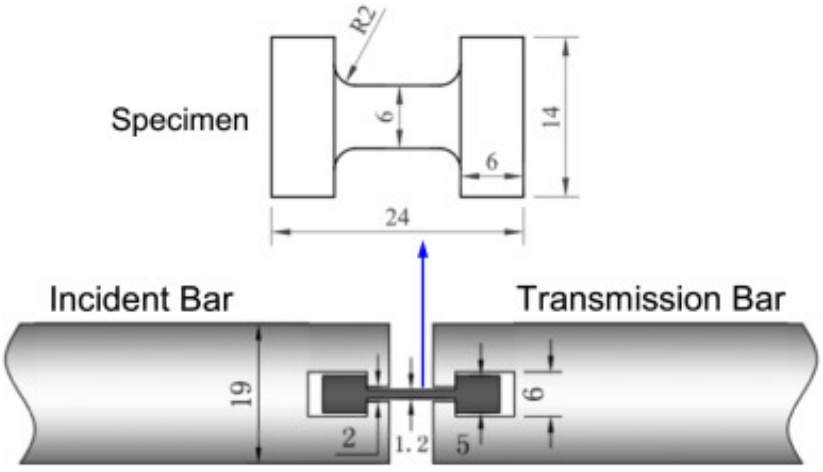

Figure 4.16. *Schematic picture of the Quick Hook Joint [101].*

Huang et al. [107] heated the attached sample with a furnace and deemed the influence of the temperature rise in the bars negligible, since the heated area of the bars was only approximately 18 cm long. Smerd et al. [108] also concluded, that even with the ceramic insulating tubes, the bars were not completely insulated but the conditions were near-

isothermal and with a comparison of tests done in room temperature, no apparent distortion was shown in the signals obtained from the tests.

As explained earlier, the sample can also be heated with a furnace without any insulative materials, if the bars are cooled. This setup is presented in Figure 4.17.

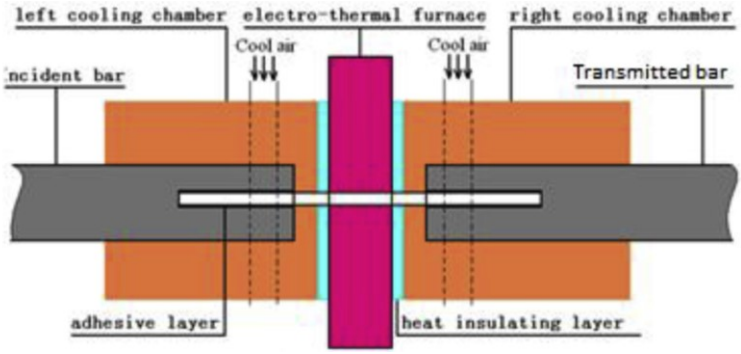

Figure 4.17 *The furnace and cooling system in high temperature SHTB tests [93].*

The bars can be cooled with air or for example water, as was done in the high temperature experiments of this thesis.

4.2 Taylor test

Even higher strain rates can be achieved with Taylor test than with split Hopkinson bar tests. Strain rates typically between 10^3 and 10^5 1/s [118] can be achieved with the Taylor test. A schematic picture of the Taylor anvil experimental setup is presented in Figure 4.18.

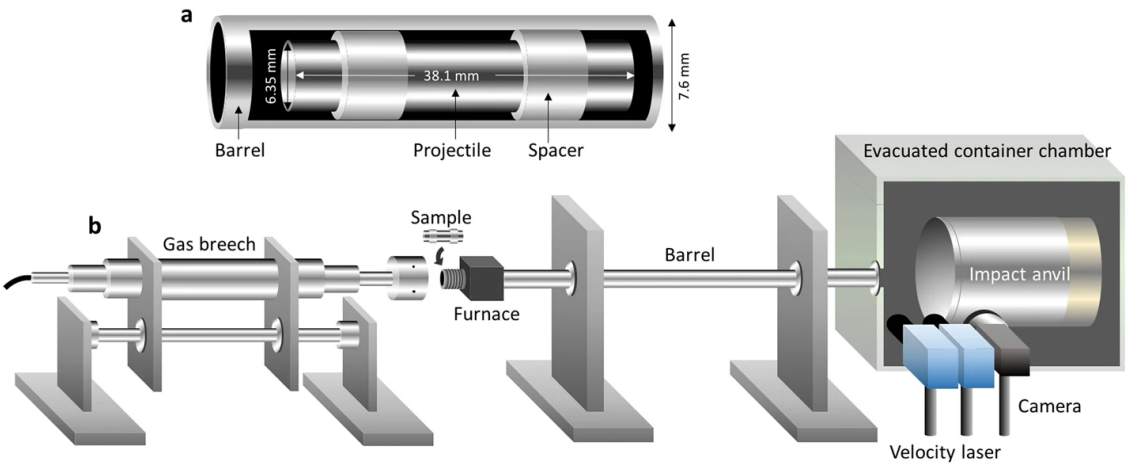

Figure 4.18. *Schematic picture of a Taylor impact experimental setup with a) the sample and b) the gas gun experimental setup [119].*

The sample [118] is shot against the rigid impact anvil. The average yield strength can be determined from the final shape of the projectile, when it's compared to the original

shape and length of the projectile. [118-120] Figure 4.19 illustrates the deformation of projectiles shot at different velocities.

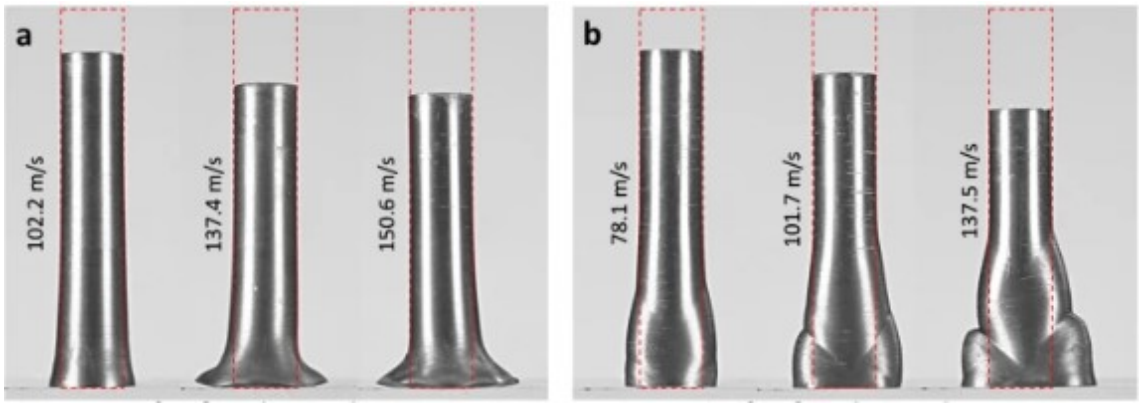

Figure 4.19. *Deformation of projectiles shot to the rigid wall at different velocities [119].*

To carry out the Taylor anvil test at elevated temperature, a furnace [119] or a heating coil [121] can be used to heat the sample. In high temperature tests the sample is typically stationary and the target anvil is shot against it.

4.3 Expanding ring

Expanding ring technique is another way to measure the flow stress and failure behaviour of materials under high strain rates [34, 122, 123]. The schematic picture of the setup is presented in Figure 4.20.

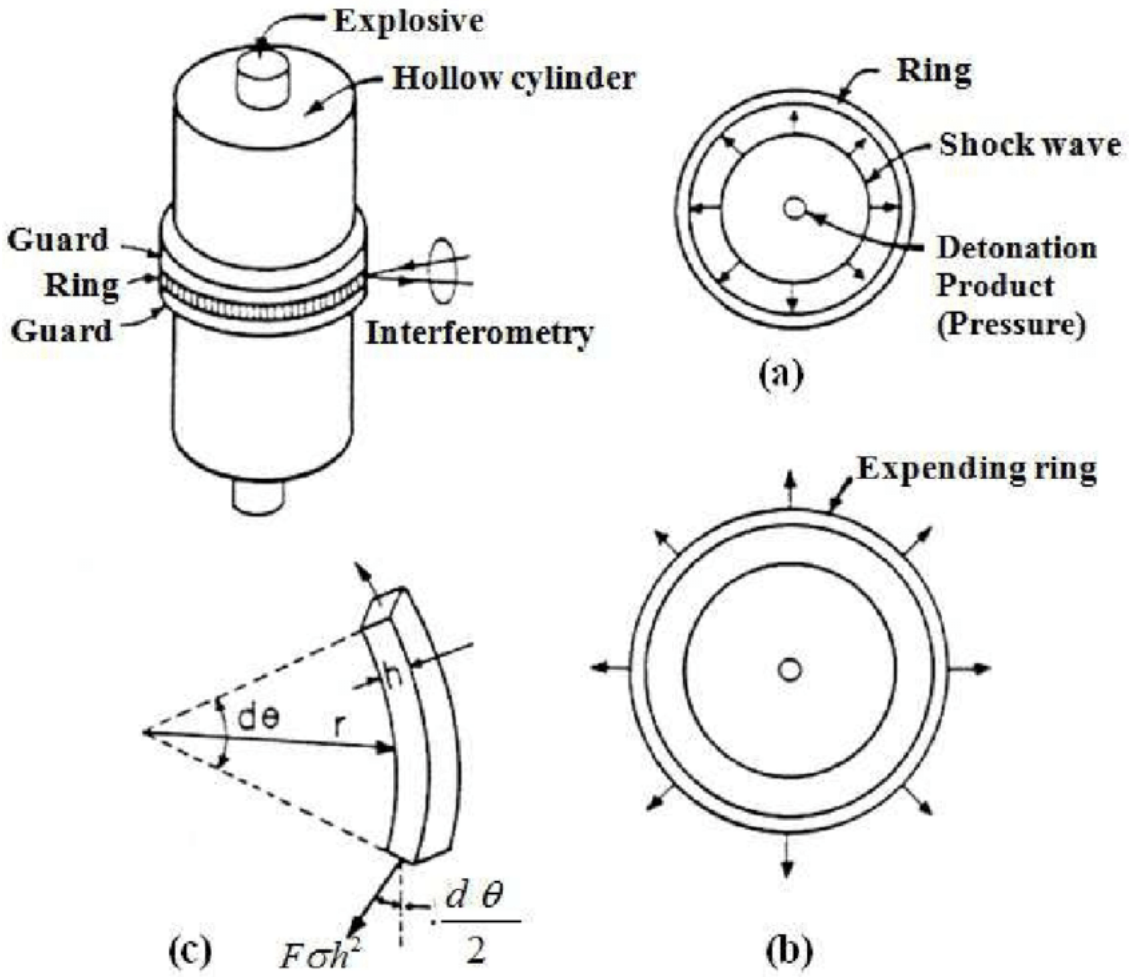

Figure 4.20. *Schematic picture of the expanding ring technique: a) explosive inside a steel block, b) cylinder's cross section right after explosion, and c) a section of the ring [34].*

The expanding ring technique was first introduced by Johnson, Stein, and Davis [124] in 1963. The explosive in the core of the ring is detonated causing high pressure inside the steel cylinder, which results in a shock wave travelling from inside to outward. The wave then enters the ring, expanding the radius of the ring. The velocity is measured by laser interferometry and with the velocity history the stress-strain curve of the ring can be determined at the imposed strain rate. [34, 122] Since the velocity history is known the deceleration of the ring can be calculated. With it and the known density and volume of the ring, the force can be calculated and thereby the stress.

5 RESEARCH METHODOLOGY AND MATERIALS

In this Chapter, the experimental setup and the geometry and material of the samples are presented. Also, the analysis of the collected experimental data is explained briefly.

5.1 Experimental setup

The experimental part of this thesis was carried out in the materials engineering laboratory of Universidad Politécnica de Madrid with a split Hopkinson tensile bar. A schematic picture of the SHTB used is shown in Figure 5.1.

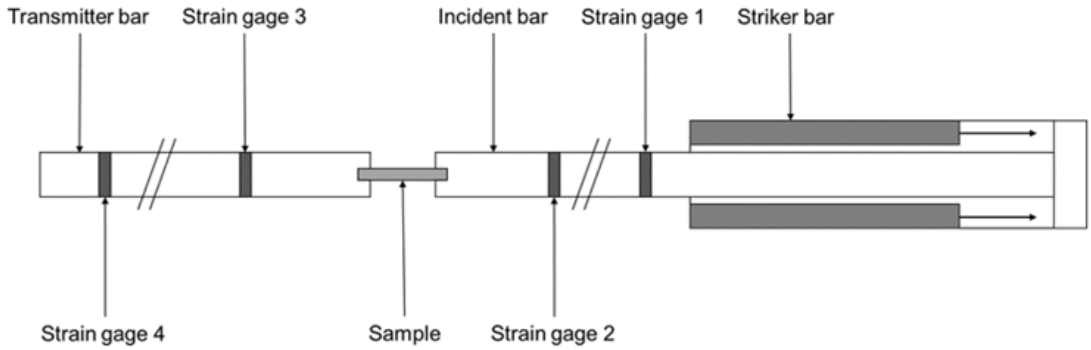

Figure 5.1 *The experimental setup.*

As explained in Chapter 3.1, in SHTB the sample is attached to the transmitter and incident bars, and the elastic waves are measured with strain gages mounted on both bars. In this experiment four strain gage stations were used instead of two to avoid losing any data if a strain gage was broken during the measurement.

First in the experiment the sample was mounted to the bars and the incident bar was placed to the correct position. Also, the placing of the transmitter bar was checked. After this, the camera that was used to record the measurements was positioned and focused correctly. The mounted sample is presented in Figure 5.2, where also the light source is shown.

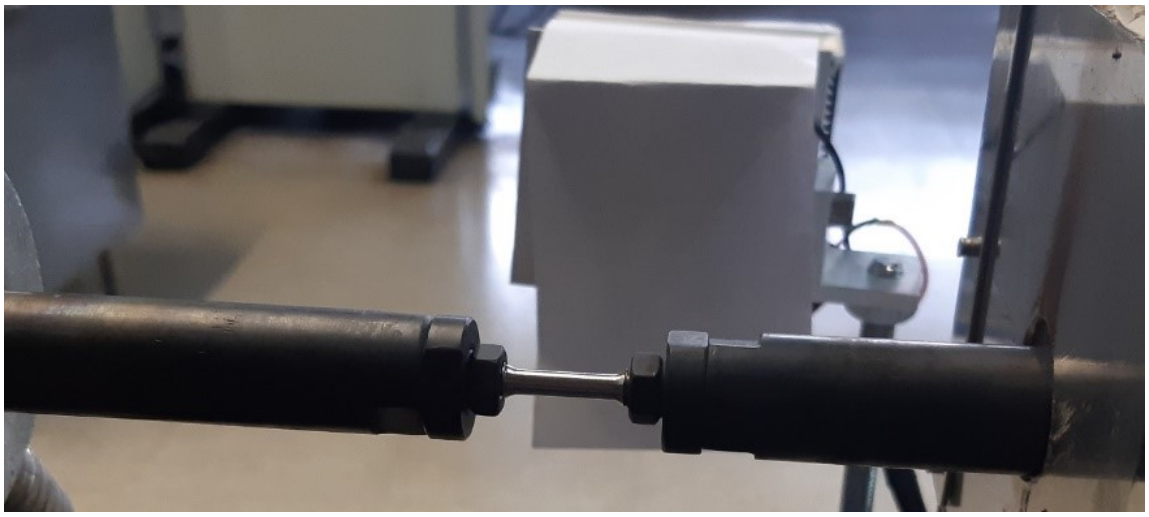

Figure 5.2 *Mounted sample and light source.*

The sample was mounted by screwing it into the bars, since in this test setup glue cannot be used. The sample was fastened into place with two bolts and the mounting of the sample didn't fail during any experiment. The light source was important, since the experiments were recorded with a video camera to make sure they were successful, and the sample needed to be illuminated. The light from the source was softened with a paper.

If the sample was heated, the next step was to put the furnace, thermocouple, and the bar cooling system to place and turn them on. The heating took approximately 45-60 minutes and the exact temperature of the sample was measured with the thermocouple touching the sample. The placing of the thermocouple is shown in Figure 5.3. After the sample had reached the target temperature, the strain gages were checked to make sure they were working properly, and the thermocouple was removed from the furnace to avoid breaking it. After this, the light source was turned on, the recording of the camera started automatically when the strain gages started to measure any elastic waves in the bars.

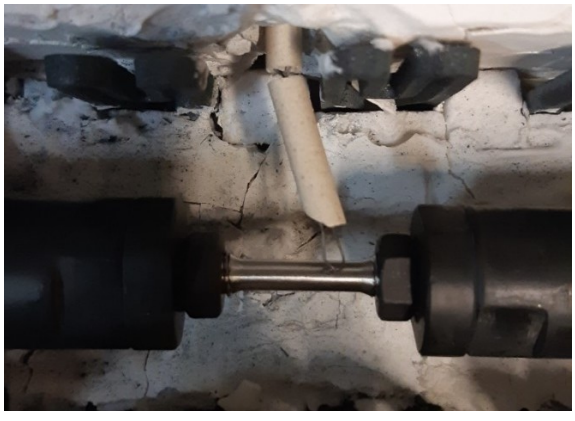

Figure 5.3 *Position of the thermocouple inside the furnace.*

The downside of the heating of the sample with a furnace was that the furnace blocked the camera view, as can be seen in Figure 5.4.

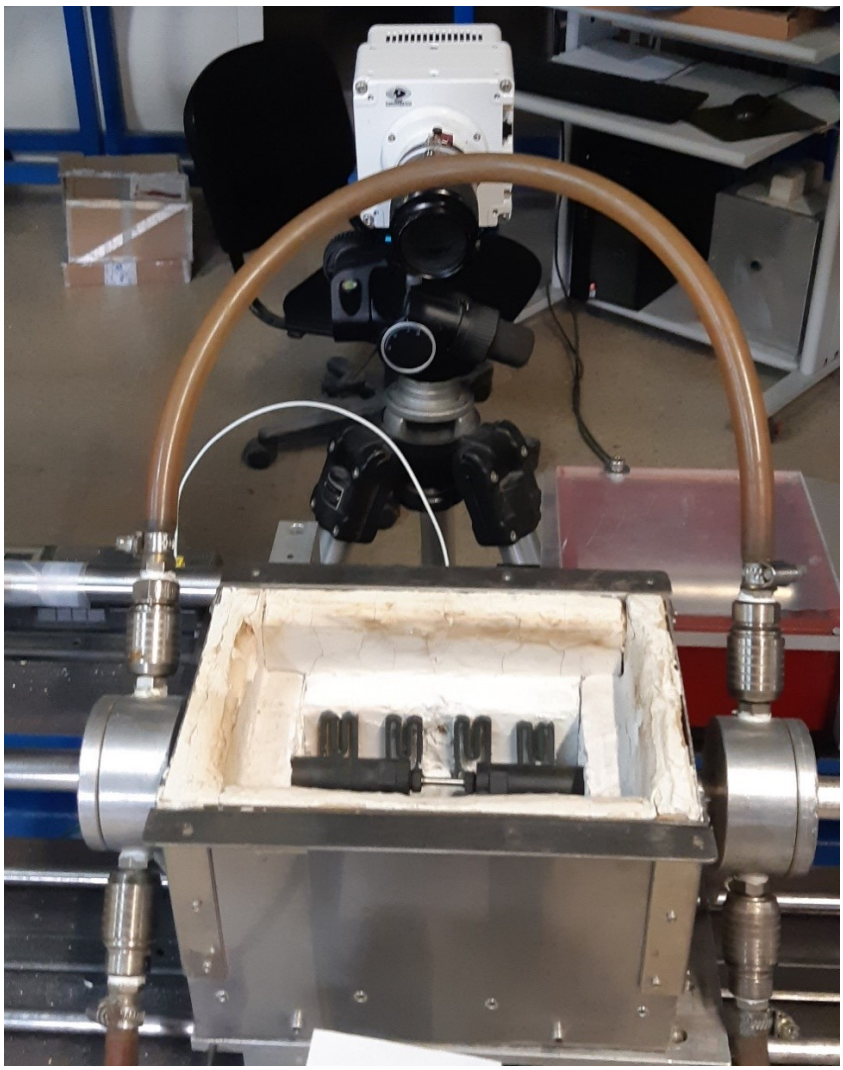

Figure 5.4 *The setup of the camera, furnace and cooling system.*

This was solved by having two people working at the same time on the experiment at this point. Almost simultaneously the furnace was moved aside, and the striker bar was launched. The sample didn't have time to cool down much during this time. After the experiment, all the results from the strain gages and the camera were saved.

5.2 Samples

The material studied in this thesis was a proprietary industrial nickel-based superalloy, which means that its composition and the heat treatment history are not presented in this thesis. However, the material is a nickel-based superalloy, intended to be used as a jet engine turbine blade material. In Table 5.2.1, the diameters and testing temperatures of the samples are presented.

Table 5.2.1. *The diameters and testing temperatures of the samples.*

Sample	L_s	Do	D1	D2	D3	D4	D5	D_s	T
T01	20	4	4.007	3.993	4.015	4.019	4.020	4.011	20
T02	20	4	4.050	4.047	4.047	4.033	4.027	4.041	650
T03	20	4	3.994	3.991	3.980	3.977	3.982	3.985	760
T04	20	4	3.897	3.866	3.881	3.880	3.876	3.880	
T05	20	4	4.027	4.035	4.040	4.051	4.057	4.042	20
T06	20	4	4.000	3.998	3.992	3.985	3.984	3.992	20
T07	20	4	4.017	4.025	4.043	4.045	4.045	4.035	650
T08	20	4	4.029	4.026	4.022	4.015	4.016	4.022	760
T09	20	4	4.004	4.005	4.012	4.017	4.023	4.012	650
T10	20	4	3.992	3.999	4.000	4.003	4.008	4.000	650
T11	20	4	3.997	3.999	4.004	4.009	4.013	4.004	760
T12	20	4	4.007	4.020	4.020	4.026	4.021	4.019	20
T13	20	4	4.047	4.051	4.046	4.039	4.028	4.042	650
T14	20	4	3.989	4.002	4.012	4.007	4.009	4.004	20
T15	20	4	4.032	4.032	4.036	4.038	4.044	4.036	760
T16	20	4	3.909	3.905	3.900	3.898	3.898	3.902	760
T17	20	4	3.969	3.98	3.997	3.999	4.006	3.990	20
T18	20	4	3.991	3.995	4.001	4.010	4.014	4.002	650
T19	20	4	4.027	4.020	4.006	4.003	3.993	4.010	760
T20	20	4	2.832	2.828	2.828	2.824	2.81	2.824	

Samples 4 and 20 were not used, since their diameters were smaller than others' and they were only held as spare samples in case some tests would fail. The samples were each measured in five places to calculate the mean diameter of the sample. In most cases, the mean value was close to the diameter in the middle of the sample (D3).

5.3 Data Analysis

The Equations presented in this Chapter can be found in many sources, for example, in the Chapter 12 of the book *Dynamic Behavior of Materials* by Marc Meyers [34], or the Chapter 2 of the book *Split Hopkinson (Kolsky) Ba*r by Weinong Chen and Bo Song [35].

In this chapter, the data analysis is explained with the used Equations as well as the plotted graphs using the data obtained from the sample T05. The sample T05 was used as an example, since its results were close to the average results obtained in the experiments done in room temperature. The original data obtained from the 4 strain gage stations can be seen in Figure 5.5.

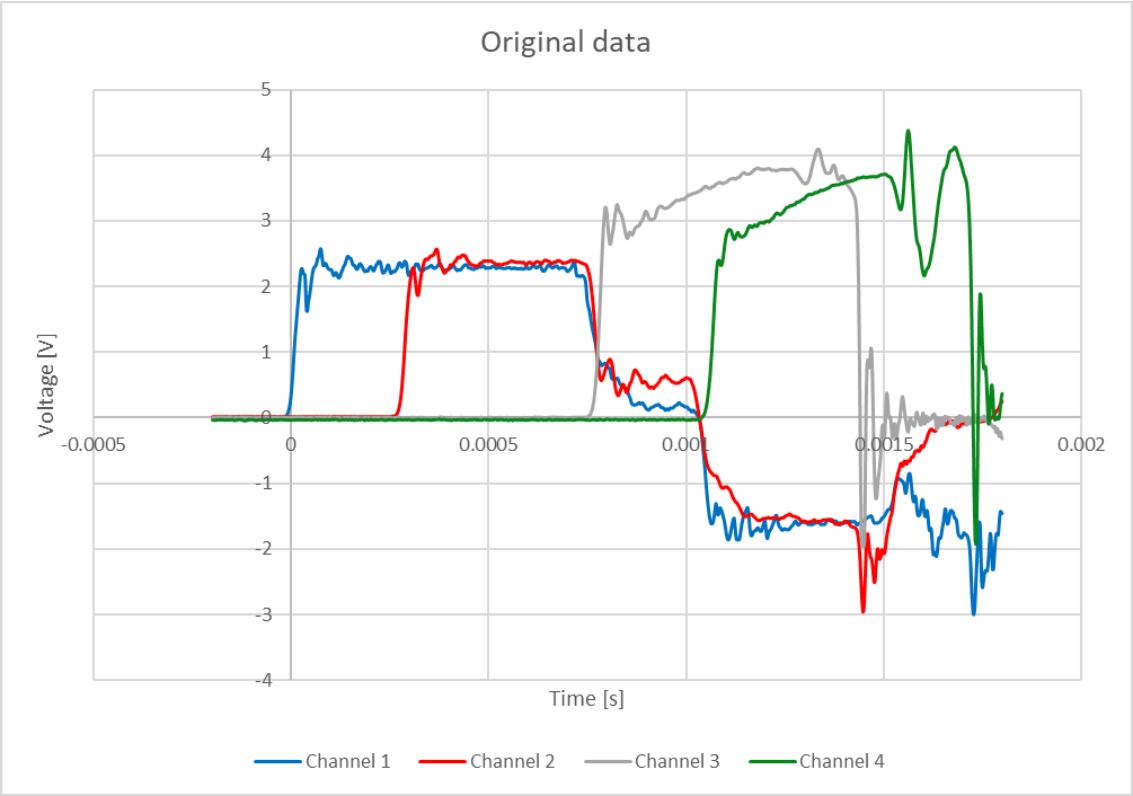

Figure 5.5 *The raw strain gage data of sample T05.*

In the graph, the channels 1 and 2 are from the incident bar and have first the incident wave and after 0.001s the reflected wave. Channels 3 and 4 contain the transmitted waves. The first step of the data analysis was to align the voltage data obtained from channels 1 and 3 to same graph with the same starting point. This can be seen in Figure 5.6.

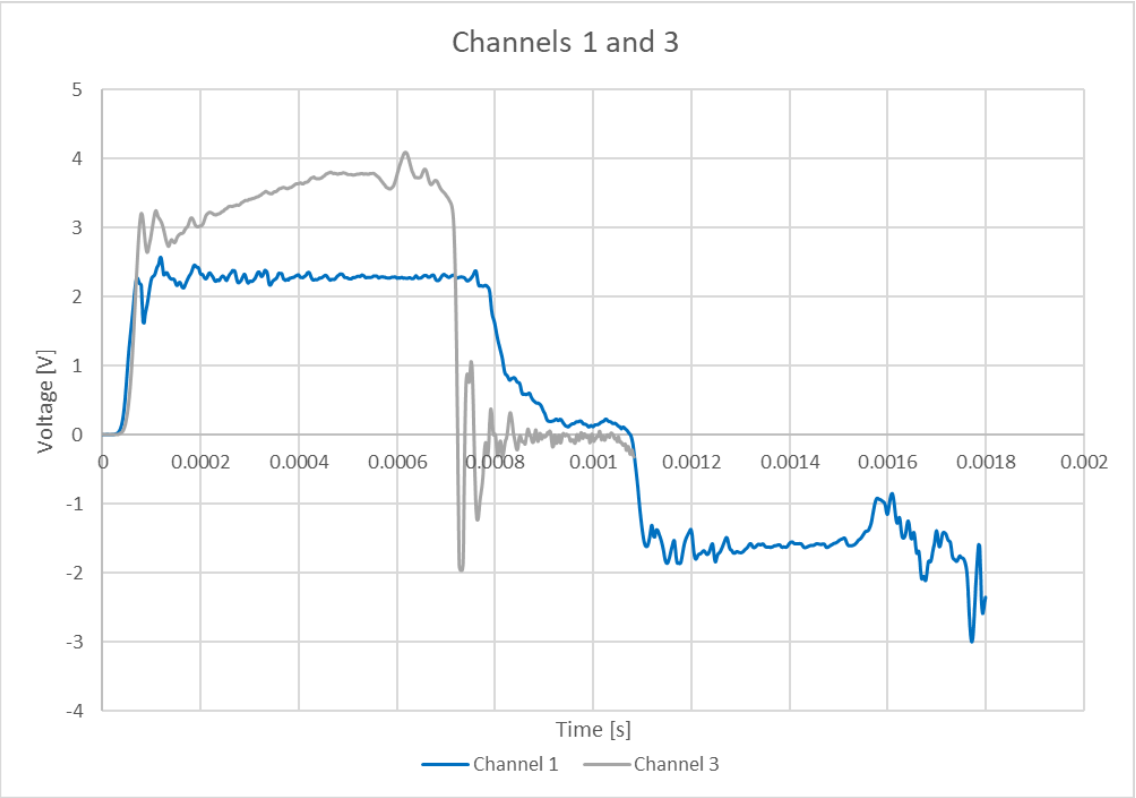

Figure 5.6 *Channels 1 and 3 aligned together.*

This step is important, since the next step is to convert the voltage into strain and plot the incident pulse (ε_I), the reflected pulse (ε_R), and the transmitted pulse (ε_T). The pulses can be calculated from the measured voltages with Eq. 1.

$$\varepsilon = \frac{2}{1+\nu} \cdot \frac{U}{K_G \cdot G \cdot U_0} \tag{1}$$

where ε is the strain, v is the Poisson's ratio, U is the measured voltage, K_G is the gage factor, G is the gain, and U_0 is the excitation voltage. The strain pulses can be seen in Figure 5.7.

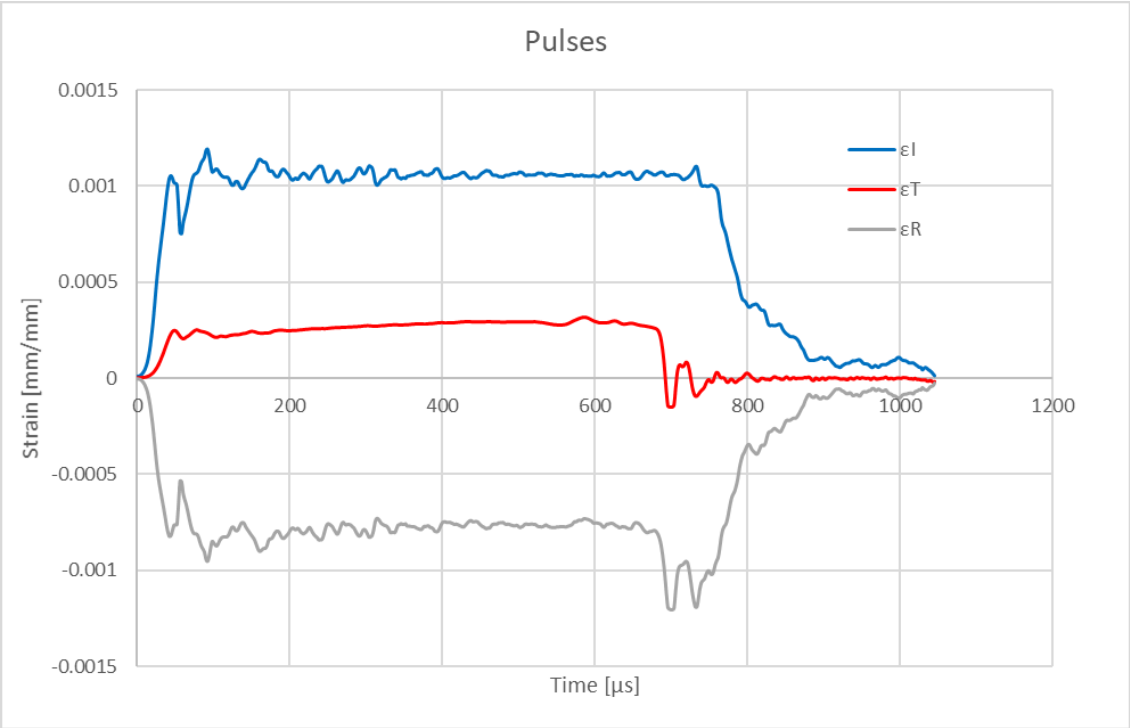

Figure 5.7 *Incident, transmitted and reflected pulses.*

The reflected pulse was calculated by subtracting the incident pulse from the transmitted pulse. For this to be possible, it must be assumed, that the sample is in dynamic stress equilibrium. The pulses are used in the calculations of the interface velocities. The constants used in this experiment are presented in Table 5.3.1.

Table 5.3.1 *The constants of the experiment.*

K_G	G_1	G_3	U_1	U_3
2.18	200	1200 (RT), 1800 (HT)	7.64 V	7.63 V

The gains chosen for the experiment need to be considered when calculating the results. For incident waves, measured with channel 1, the chosen gain was G_1 is 200 and for transmitted waves, measured with channel 3, the gain was G_3 is 1200. The constant voltages, U_0, are correspondingly U_1 is 7.64 V for the incident wave and U_3 is 7.63 V for the transmitted wave.

Table 5.3.2 lists the Poisson's ratio, Young's modulus E, density ρ, and the speed of sound C_0, that is calculated as the square root of Young's modulus divided by the density of the material [125]. Also, the diameter D_B and the area A_B of the bars are presented.

Table 5.3.2 *Properties of the bars.*

v	E	ρ	C_0	D_B	A_B
0.3	218 GPa	8249 kg/m^3	5140.73 m/s	19.3 mm	292.55 mm^2

Next, the data analysis process is presented for sample T05 as an example of the process carried out for all of the samples. The length L_s, diameter D_s and the area A_s of the sample T05 are given in Table 5.3.3.

Table 5.3.3 *Properties of sample T05.*

L_s	D_s	A_s
20.00 mm	4.042 mm	12.83 mm^2

The nominal length is the same for each sample, but the diameters vary and are presented in Table 5.2.1. The exact diameter was used for the calculations of results for each sample.

The next step is to calculate the interface velocities, V_A and V_B. This can be done using Eq. 2 and Eq. 3.

$$V_A = -C_0 \cdot (\varepsilon_I - \varepsilon_R) \tag{2}$$

$$V_B = -C_0 \cdot \varepsilon_T \tag{3}$$

where V_A and V_B are the interface velocities, C_0 is the speed of sound, ε_I is the incident pulse, ε_R is the reflected pulse, and ε_T is the transmitted pulse. The resulting interface velocities for sample T05 are presented Figure 5.8.

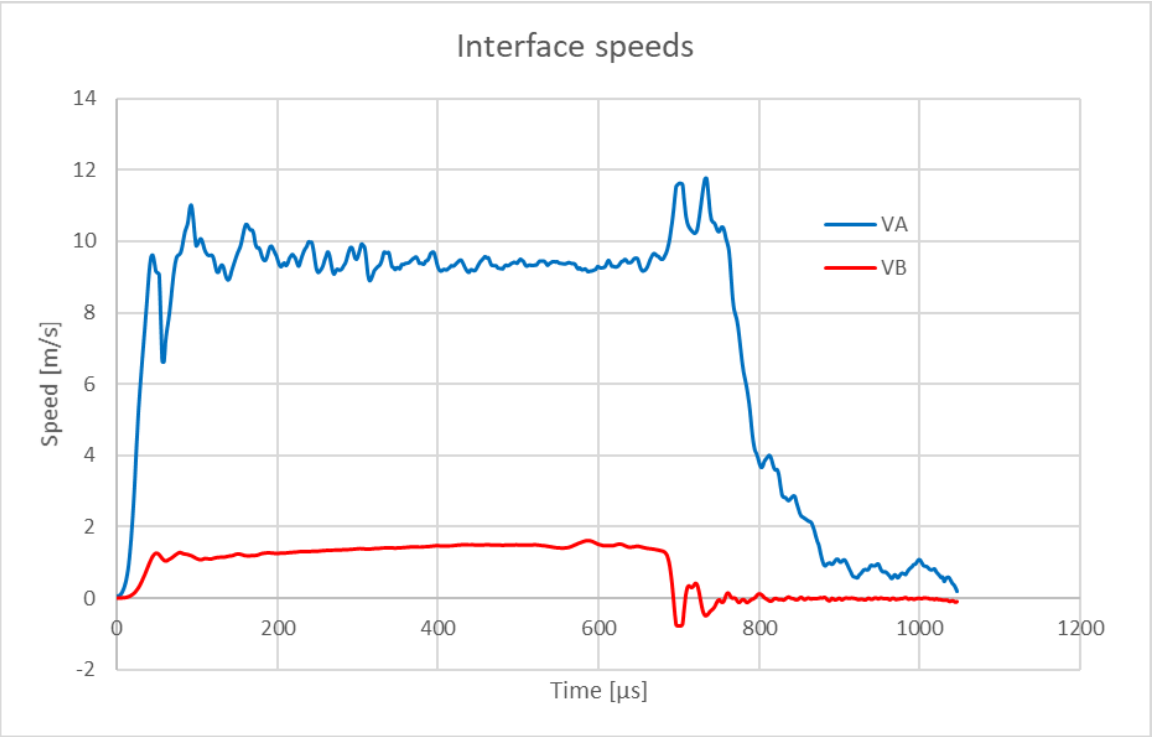

Figure 5.8 *The interface velocities.*

The interface velocities are used when calculating the strain rate. The strain rate was calculated with Eq. 4.

$$\dot{\varepsilon} = \frac{(V_A - V_B)}{L_s} \tag{4}$$

where V_A and V_B are the interface velocities and L_s is the initial length of the sample. The strain rate as a function of time is presented in Figure 5.9.

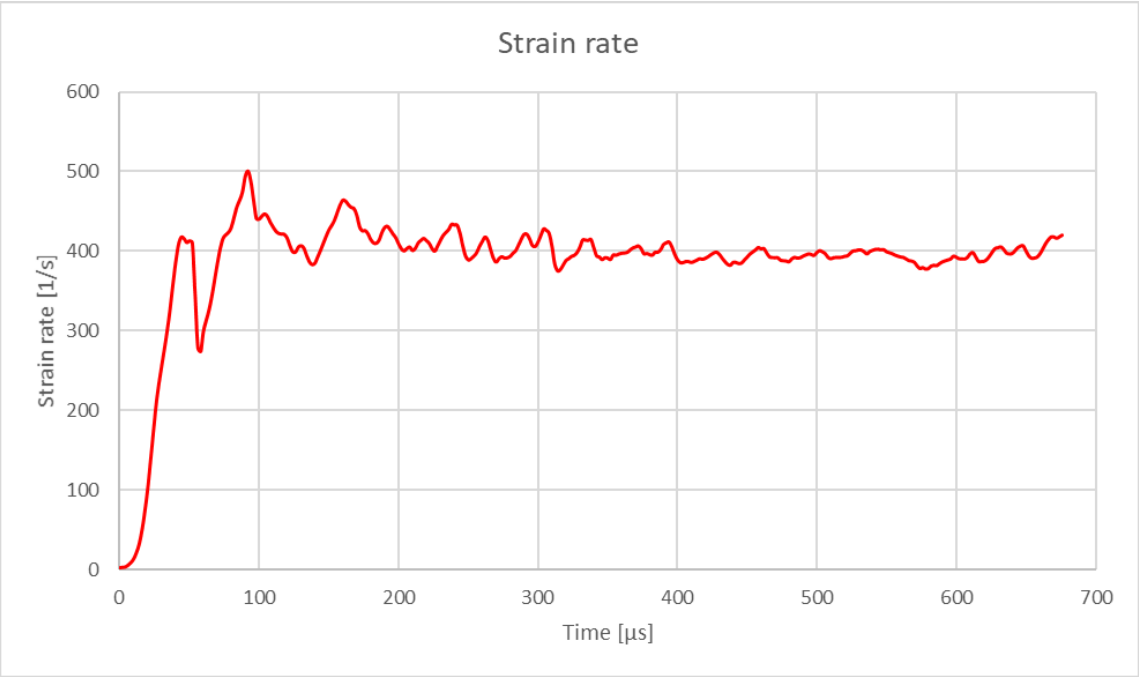

Figure 5.9 *Strain rate of sample T05 as a function of time.*

The strain rate is then used to calculate the engineering strain with Eq. 5.

$$\varepsilon_{eng} = \int_0^t \dot{\varepsilon}\, d\varepsilon \tag{5}$$

where ε_{eng} is the engineering strain, t is the time and $\dot{\varepsilon}$ is the strain rate. After this, the true strain is calculated with Eq. 6.

$$\varepsilon_{true} = \ln(1 + \varepsilon_{eng}) \tag{6}$$

where ε_{true} is the true strain and ε_{eng} is the engineering strain. These strains are presented in Figure 5.10.

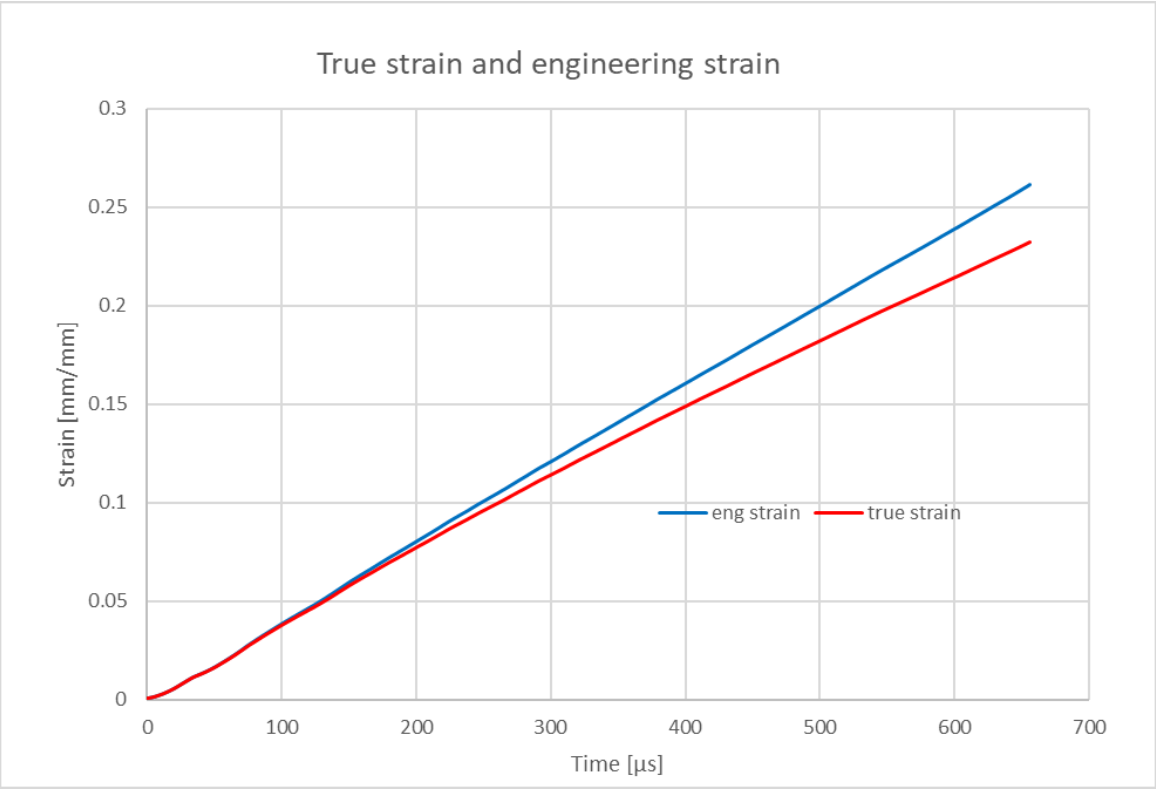

Figure 5.10 *True strain and engineering strain as function of time of sample T05.*

Since the main purpose of this thesis is to examine the tensile properties of the new nickel-based superalloy, the last step is to calculate the engineering stress and the true stress. Engineering stress is calculated with Eq. 7.

$$\sigma_{eng} = \frac{\mathrm{F}}{A_s} = \frac{A_B \cdot E \cdot \varepsilon_T}{A_s} \tag{7}$$

where σ_{eng} is the engineering stress, F is the force, A_s is the initial area of the sample, A_B is the area of the cross sections of the bars, E is the Youngs Modulus and ε_T is the transmitted pulse. True stress can be then calculated with Eq. 8.

$$\sigma_{true} = \sigma_{eng} \cdot (1 + \varepsilon_{eng}) \tag{8}$$

where σ_{true} is the true stress, σ_{eng} is the engineering stress and ε_{eng} is the engineering strain. The stresses as function of time are presented in Figure 5.11.

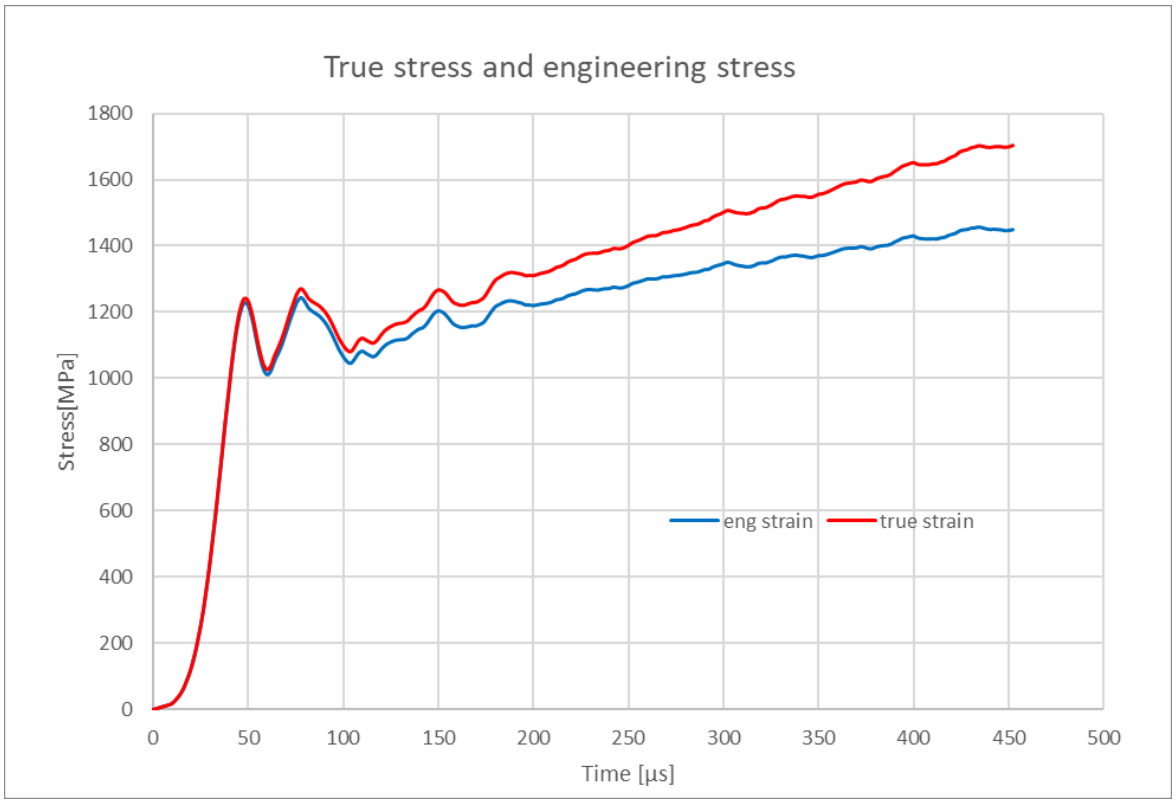

Figure 5.11. *The stresses as a function of time.*

After this, the stress strain curves were plotted. They are presented in Figure 5.12.

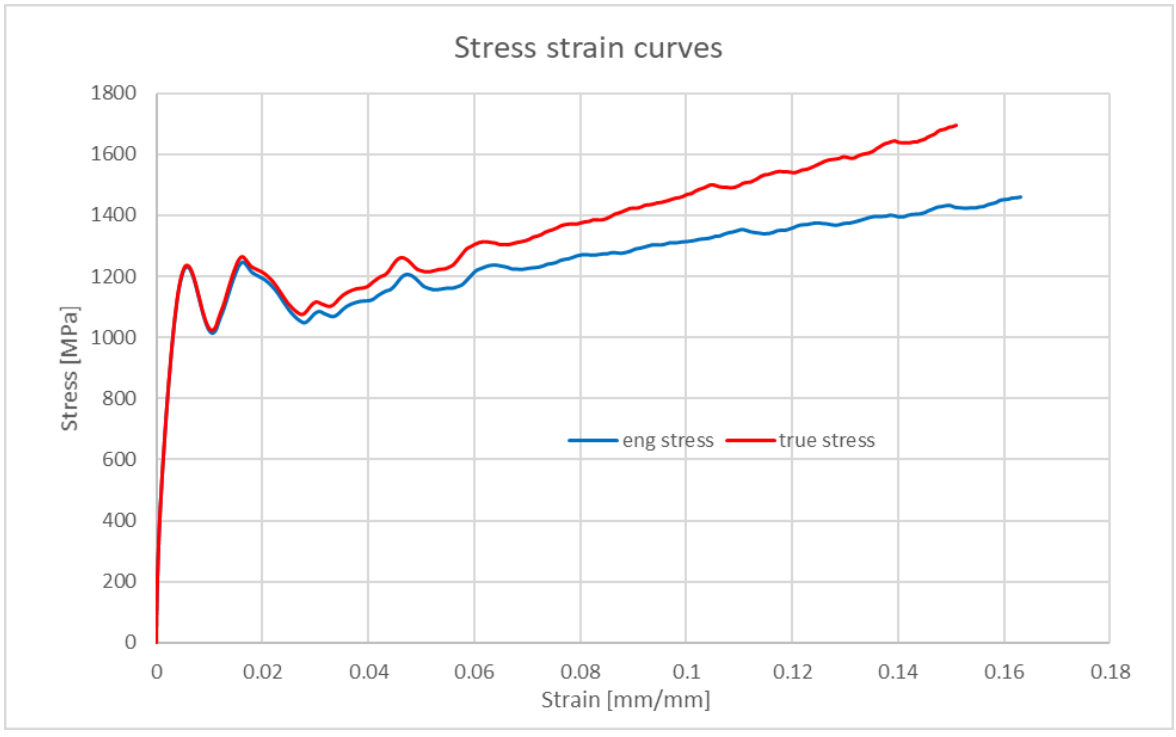

Figure 5.12 *The stress strain curves of sample T05.*

After obtaining the stress strain curves, the ultimate tensile strength of each sample was defined. The average ultimate tensile strengths for each testing temperature were also

calculated. With these, the temperature dependence of ultimate tensile strength can be examined. The failed measurements were not considered when calculating the average values. The oscillations in the beginning of the plastic deformation are due to the sample mounting fixtures and prevent the determination of the yield strength from the true stress strain curves.

6 RESULTS AND ANALYSIS

This chapter presents the results of the experiments. The failed experiments, which include samples T06, T10 and T16 are not considered, when calculating the average curves for each property in different temperatures. First, ultimate tensile strength (UTS) and yield strength and their temperature dependence are discussed, which is followed by the presentation of the strain rate dependency and after that the strain hardening and the Johnson-Cook model fitting are presented in Chapters 6.3 and 6.4.

Since the chemical composition nor the heat treatment history of the studied material is not known, the results are compared to values of different nickel-based superalloys found in literature. This is done to evaluate how the material behaves in relation to other nickel-based superalloys, since more exact comparisons are not possible.

6.1 Ultimate tensile strength

In this chapter, the different tensile properties are presented and analysed. The ultimate tensile strengths have been obtained from engineering stress strain curves, but the presented curves are true stress strain curves. In Figure 6.1, the true stress strain curves in room temperature are shown.

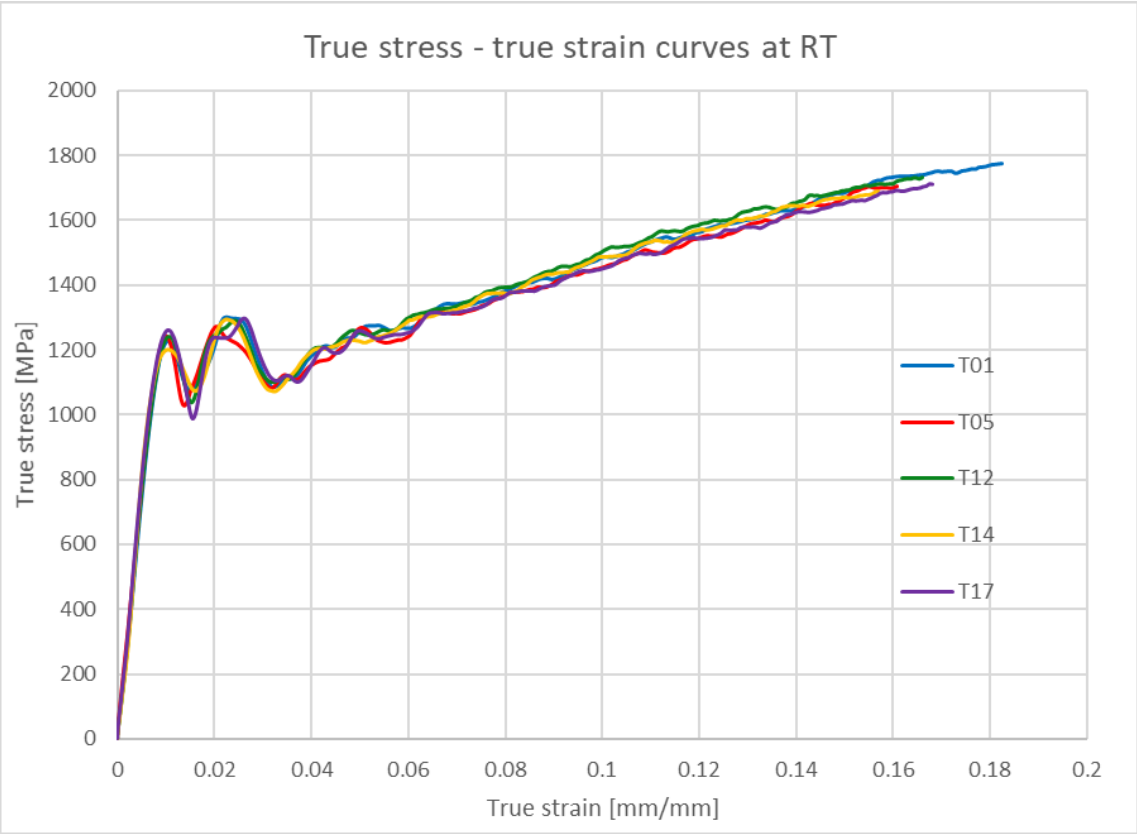

Figure 6.1 *True stress – true strain curves at room temperature.*

As can be seen, the measurements are repeatable and the true stress strain curves are similar. The only small difference between the experiments is the true strain at UTS, which varies between 0.16 and 0.18. The ultimate tensile strength varies between 1445 MPa and 1480 MPa, with an average of 1460 ± 11 MPa. At higher temperatures, the curves are not so distinctly on top of each other as at room temperature, as can be seen in Figure 6.2.

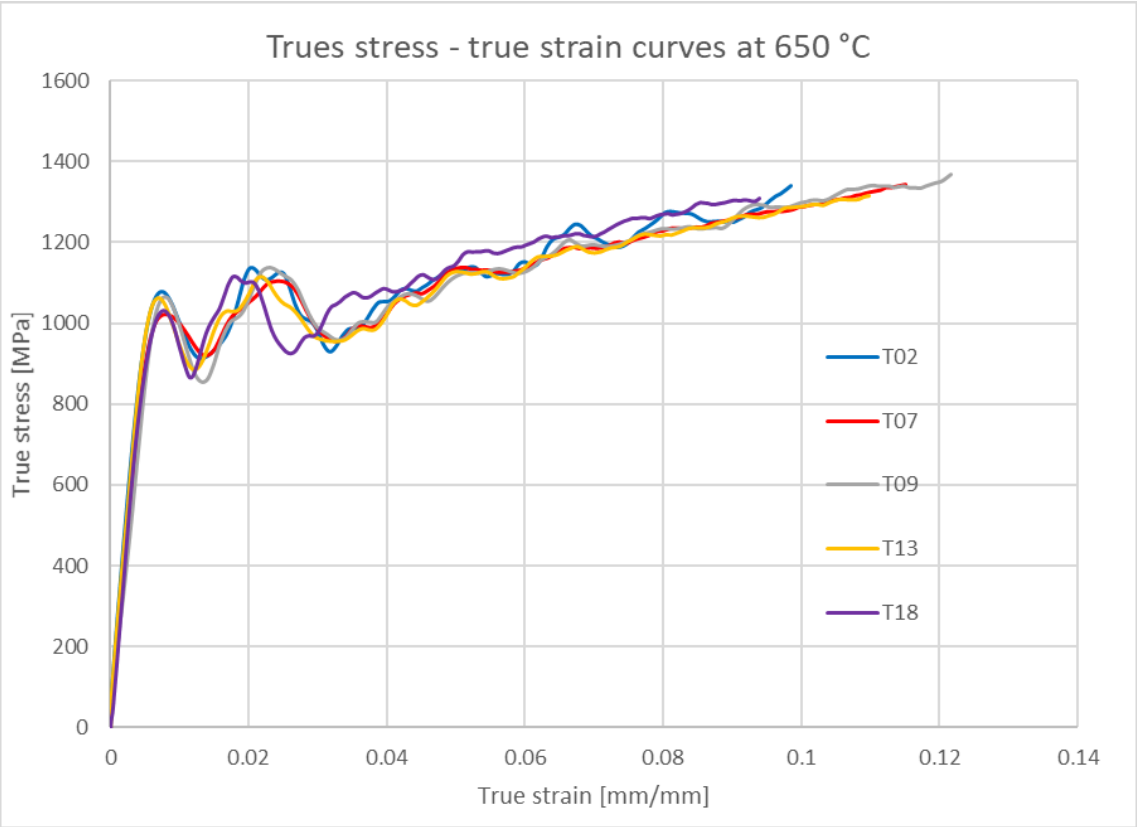

Figure 6.2 *True stress - true strain curves at 650 °C.*

When compared to the experiments carried out at room temperature, the true stress - true strain curves start to differ slightly after the elastic region but are still repeatable. The true strain values at UTS vary between 0.095 and 0.12. The minimum observed UTS was 1195 MPa and the maximum 1215 MPa. The average UTS is 1200 ± 10 MPa. The true stress – true strain curves at 760 °C are presented in Figure 6.3.

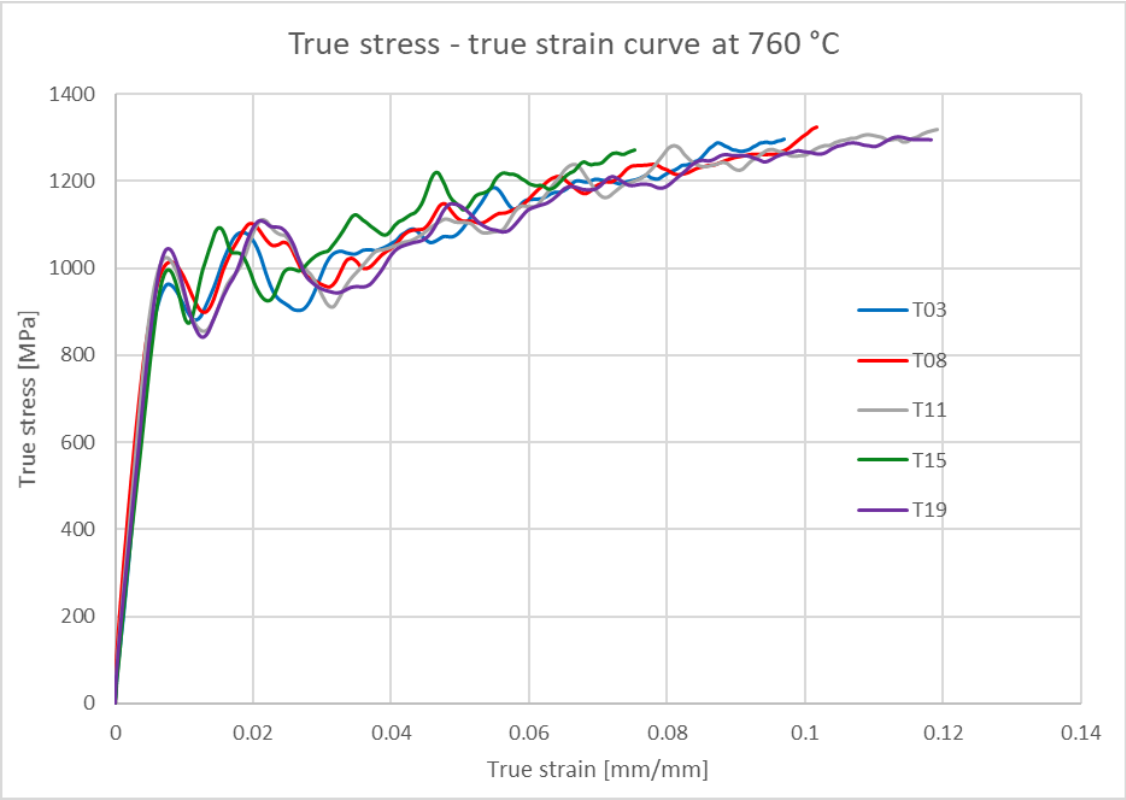

Figure 6.3 *True stress – true strain curves at 760 °C.*

Similarly, as at 650 °C, the plastic region of the true stress – true strain curves differ slightly more than at RT experiments. The true strain at UTS varies between 0.075 and 0.14. UTS varies between 1160 MPa and 1195 MPa and the average is 1180 ± 12 MPa.

The yield strengths were approximated with Matlab, while fitting the Johnson-Cook model to the experimental data. At room temperature, the yield strength was approximated by backward extrapolation with Johnson-Cook to be 900 ± 1 MPa. At 650 °C, the approximated yield strength is 830 ± 1 MPa and at 760 °C 780 ± 2 MPa. The standard deviations are small since the yield strengths are approximated values and not obtained from the curves.

All in all, the results presented here indicate that both the ultimate tensile strength and the yield strength as well as the strain at UTS decrease with increasing temperature. In addition, the standard deviation of both the ultimate tensile strength and the yield strength are really similar to each other at each of the testing temperatures, meaning that results at different temperatures are equally repeatable. The average true stress – true strain curves are presented in Figure 6.4.

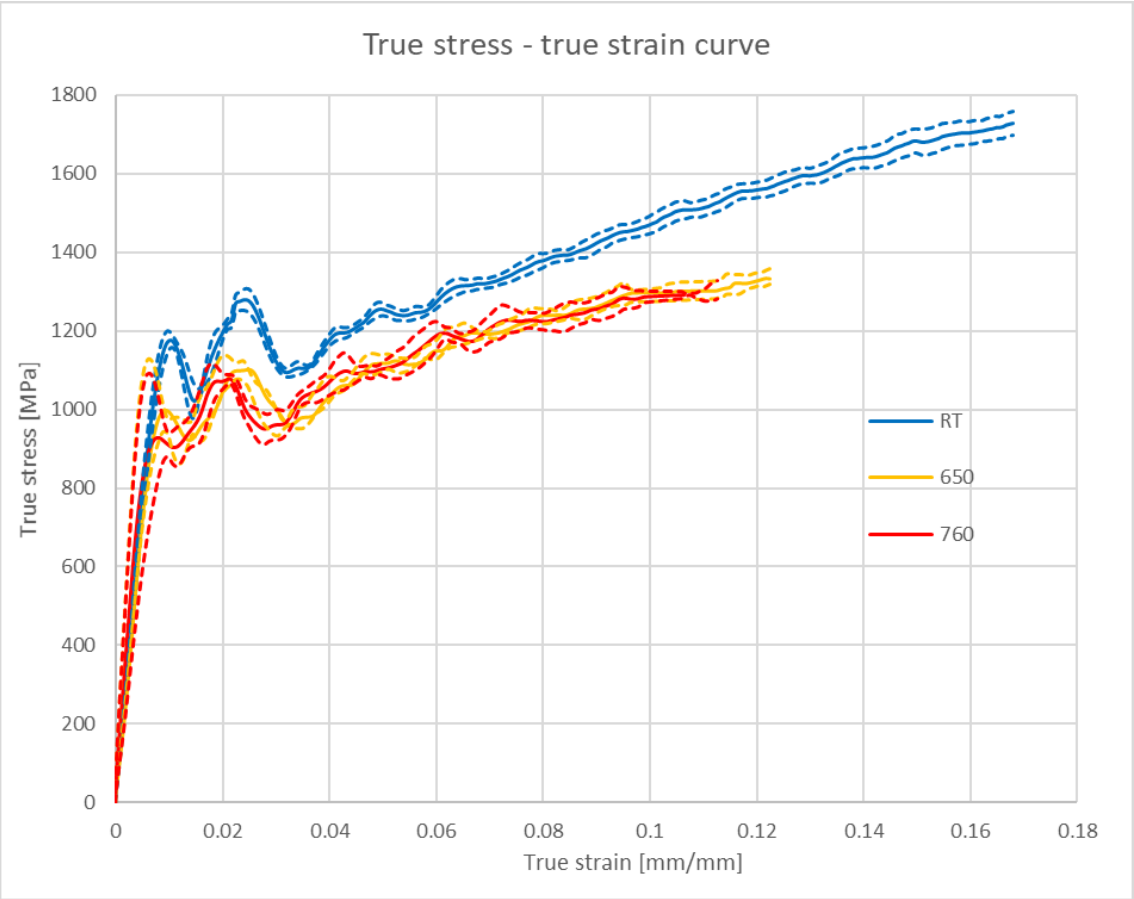

Figure 6.4 *Average true stress – true strain curves at different temperatures.*

When looking at the average yield strength and the average ultimate tensile strength at different temperatures, which are presented in Figure 6.5, it can be seen that the yield strength decreases almost linearly.

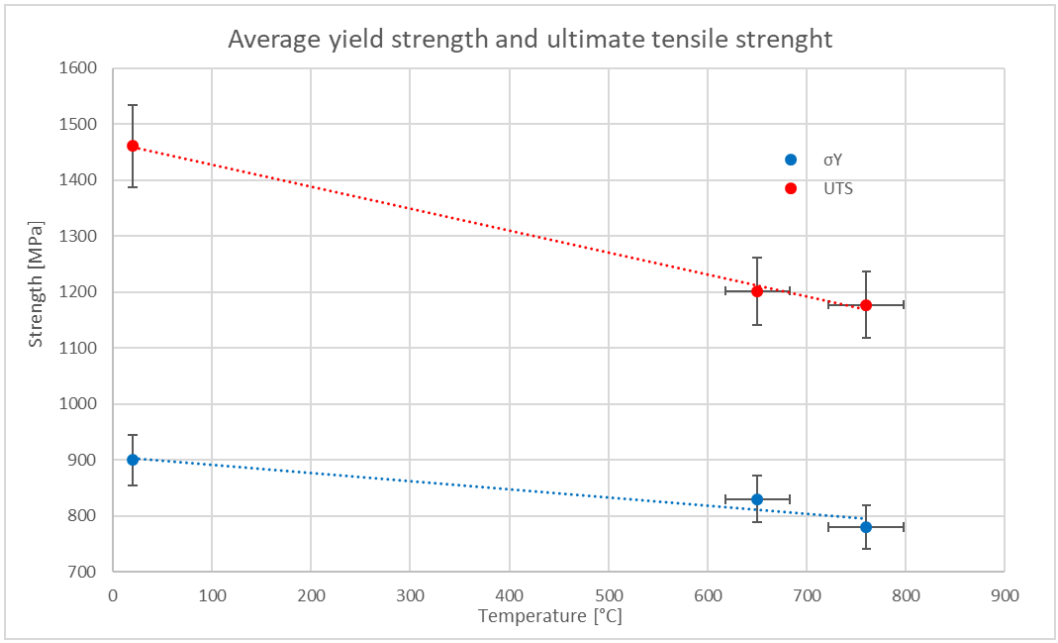

Figure 6.5 *Yield strength and ultimate tensile strength at different temperatures.*

Since the material studied in this thesis is meant to be used in a turbine blade, the results are compared to a few strength values of other turbine blade nickel-based superalloys found in literature to see how it matches the materials already being used in turbine blades.

Körner et al. [29] studied the CMSX-4 nickel superalloy that's typically used in turbine blades. The yield strength and ultimate tensile strength they determined are presented as a function of temperature in Figure 6.6.

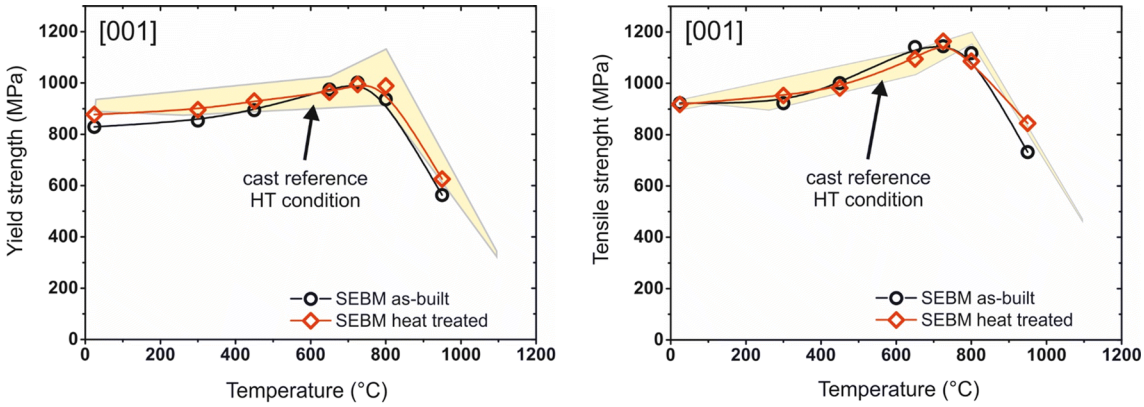

Figure 6.6. *a) yield strength and b) ultimate tensile strength of CMSX-4 nickel-based superalloy as a function of temperature [29].*

They tested both the as built and heat-treated samples which both show similar behaviour: the yield strength and the ultimate tensile strength increase until around 800 °C, after which they start to decrease. The experiments were carried out at a strain rate of $0.83 \cdot 10^{-3}$ 1/s.

Liu et al. [30] studied a K403 nickel-based superalloy and carried out tensile tests at elevated temperatures between 850 and 1000 °C. In their experiments, the ultimate tensile strength also decreased at those temperatures, as well as in the experiment of Körner et al. Depending on the strain rate, which was 0.1-10 1/s, the ultimate tensile strength in 850 °C varied between 1180 and 1400 MPa.

Wang et al. [126] studied DD407, which is a nickel-based superalloy for a turbine blade at different strain rates and at different temperatures. Their results for yield strength with different strain rates as a function of temperature are presented in Figure 6.7 a).

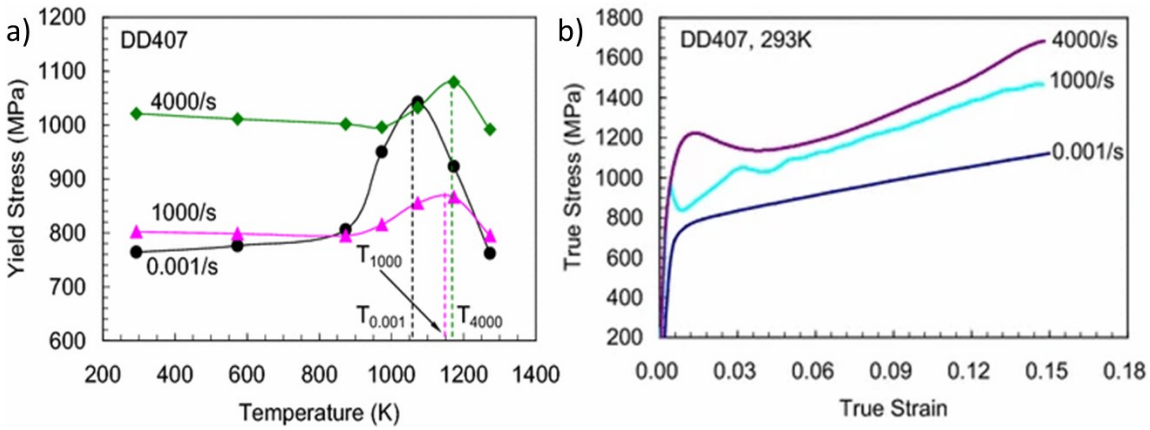

Figure 6.7. *a) The yield strength of DD407 as function of temperature and b) true stress-strain curves in room temperature [126].*

The nickel-based superalloy they studied also had a slight decrease in the yield strength with higher strain rates, 1000 and 4000 1/s, at the temperature range from room temperature to 800 °C. The yield strength was around 800 MPa at the strain rate 1000 1/s, which is the closest in magnitude to the strain rates used in the experiments of this thesis. With higher strain rates higher strengths were measured, as can be expected, as was explained in Chapter 2 of this thesis. The ultimate tensile strengths of their experiment were also higher at higher strain rates. The true stress-strain curves can be seen in Figure 6.7 b). At room temperature and at strain rate of 1000 1/s the ultimate tensile strength is around 1200 MPa.

Tan et al. [127] studied the temperature dependency of tensile properties of a novel nickel-superalloy to be used in jet engines as well. Their results are presented in Figure 6.8.

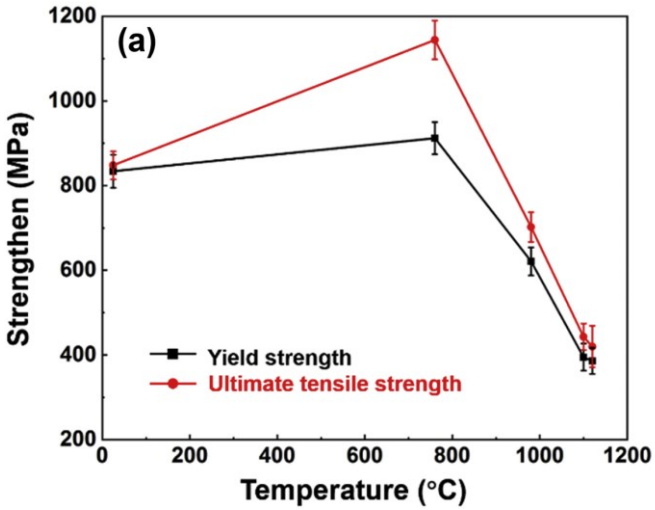

Figure 6.8. *The yield strength and ultimate tensile strength of a novel nickel-based superalloy for jet engines studied by Tan et al [127].*

They also concluded that the yield strength and the ultimate tensile strength increase with increasing temperature until 800 °C, after which both of them start decreasing rapidly.

CMSX-4 and the novel nickel-based superalloy studied by Tan et al. were both tested in room temperature as well as in elevated temperatures. They also concluded that both the yield strength and the ultimate tensile strength increase as a function of temperature up to 800 °C, after which they start decreasing. The K403 nickel-based superalloy was only tested in elevated temperatures between 850 °C and 1000 °C, it also had a decrease in yield strength and UTS with increasing temperature. The superalloy DD407 however had a slight decrease in both the yield strength and the ultimate tensile strength from room temperature to 800 °C and they only started to increase after 900 °C and then decrease rapidly after the temperature of 1000-1200 °C was reached.

The yield strengths of the nickel-based superalloys for turbine engines varied at room temperature between 750 and 1000 MPa and at around 800 °C between 800 and 1400 MPa. The ultimate tensile strengths were between 800 and 1600 MPa at room temperature and between 1200 and 1400 MPa at around 800 °C temperatures. [30, 126, 127]

When comparing the yield strength and ultimate tensile strength of the nickel-based superalloy studied in this thesis, the yield strengths at room temperature and at 760 °C, 900 MPa and 780 MPa respectively, are within the range of the materials found from the literature. At room temperature the ultimate tensile strength of the material studied in this thesis is 1460 MPa, which is rather high, when compared to the other presented materials. At 760 °C the UTS is 1180 MPa, being around the same range as the lowest ultimate tensile strengths at around 800 °C of the materials found from literature.

Both the yield strength and the ultimate tensile strength of the material studied in this thesis are rather high at room temperature when compared to other materials used in jet engines, in which this material is planned to be used as well. However, at elevated temperatures the yield strength and UTS are both rather on the lower side of the strength range of the other presented materials that are meant to be used in highest temperature applications.

6.2 Strain rate sensitivity

In this chapter, the strain rate sensitivity of the studied nickel alloy is evaluated. In Figure 6.9, the strain rate sensitivity of ultimate tensile strength and yield strength at each temperature is plotted.

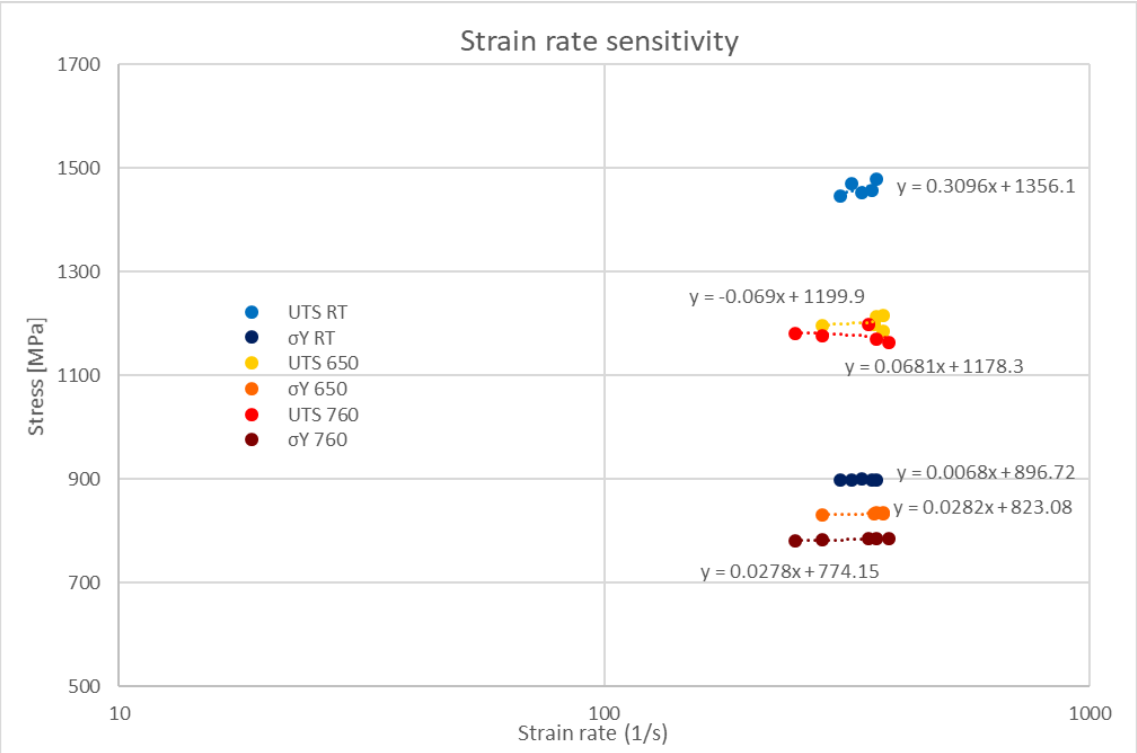

Figure 6.9. *The strain rate sensitivity of the material.*

The strain rate sensitivities at different temperatures vary between -0.07 and 0.31 MPa·s, meaning that the strain rate sensitivity of the material in this narrow strain rate range is quite low. The ultimate tensile stress seems slightly more strain rate sensitive at room temperature than at elevated temperatures. To have a more complete understanding of the strain rate sensitivity of the studied material it should be tested further at a wider strain rate range. The strain rate range of this thesis is not enough to determine the strain rate sensitivity completely reliably.

6.3 Strain hardening coefficients with Hollomon Equation

Strain hardening coefficient of a material can be calculated using the Hollomon Equation [128, 129], which is presented as Eq. 9.

$$\sigma = K_H \varepsilon^{n_H}, \tag{9}$$

where σ is true stress, K_H the strength coefficient, and n_H the strain hardening coefficient or exponent [128, 129].

The Hollomon Equation was fitted to the experimental data using the Matlab Curve fitting toolbox. First, the plastic part of the true strain – true stress data was extracted from the whole dataset to be used in the fitting. Figure 6.10 illustrates the fitting of the Hollomon Equation to the data of sample T01 which was tested at a strain rate of 431 1/s and at room temperature.

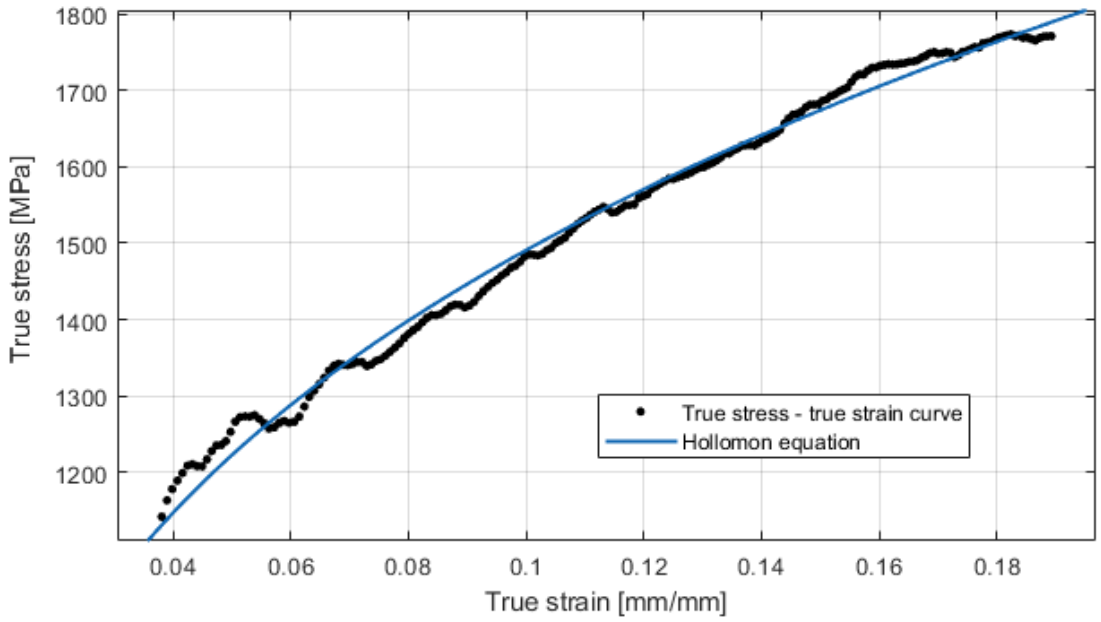

Figure 6.10. *The fitting of the Hollomon Equation to the experimental data of specimen T01.*

Similar fitting was carried out for all the successful experiments. The parameters K_H and n_H for each test are shown in table 6.3.1.

Table 6.3.1. *K_H and n_H values obtained for each test.*

Sample	K [MPa]	n	Strain rate [1/s]	Temperature [°C]
T01	2880	0.29	431	20
T05	2860	0.29	414	20
T12	2890	0.28	371	20
T14	2820	0.28	357	20
T17	2810	0.28	394	20
T02	2070	0.20	414	650
T07	2080	0.21	397	650
T09	2100	0.21	425	650
T13	2010	0.20	429	650
T18	2150	0.21	321	650
T03	2010	0.20	313	760
T08	1980	0.19	396	760
T11	2020	0.20	420	760
T15	2080	0.19	288	760
T19	1920	0.18	451	760

The strain hardening coefficients vary between 0.18 and 0.29, reaching higher values at lower temperatures. The strain hardening coefficient as a function of strain rate is presented in Figure 6.11.

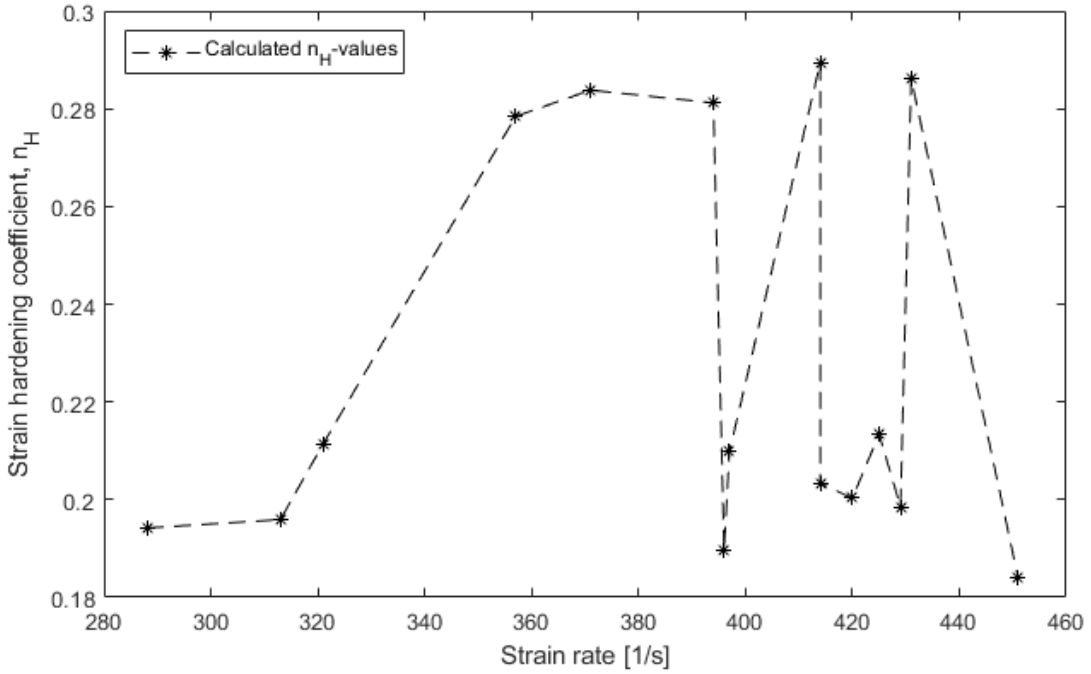

Figure 6.11. *The strain hardening coefficient as a function of strain rate at different temperatures.*

The strain hardening coefficient is not dependent on the strain rate but decreases quite much with increasing temperature. In Figure 6.12, the average and all calculated n_H values are plotted as a function of temperature.

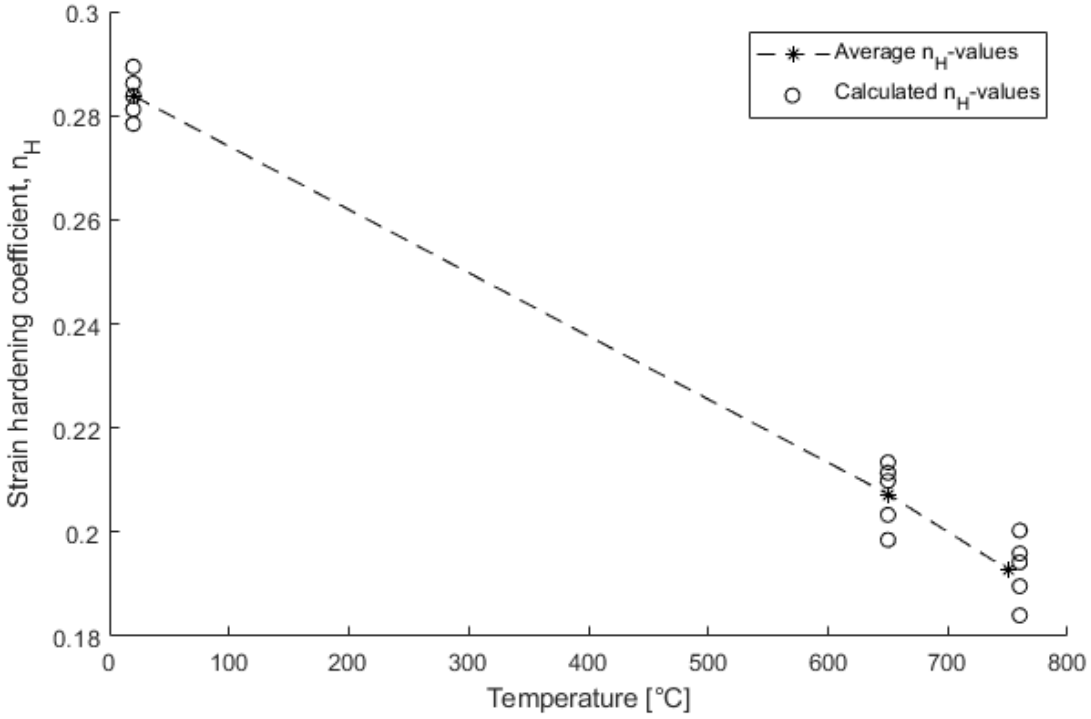

Figure 6.12. *The strain hardening coefficient as a function of temperature.*

The strain hardening of the studied material depends on the temperature and decreases linearly with increasing temperature. At room temperature, the strain hardening coefficients of the different samples are slightly closer to each other than at elevated temperatures. This might be explained with the smoother true stress – true strain curves at room temperature than at elevated temperatures.

In experiments by Gopinath et al. [130], the effect of temperature and strain rate on strain hardening coefficient of a nickel-based superalloy 720Li was studied. The material had been heat treated with solutionizing and two-stage aging. In their experiment it was concluded that the strain hardening rate is not strain rate sensitive at a temperature range 25-400 °C, however, the strain rates were only 10^{-5} - 10^{-1}. Their strain hardening coefficients for 720Li were 0.22-0.25. Zhang et al. [131] tested the single crystal superalloy CMSX-4, which is used in turbine blades. The tests were carried out at room temperature and at strain rates of $5 \cdot 10^{-4}$ 1/s and $5 \cdot 10^{-3}$ 1/s. They also analysed the Hollomon Equation strain hardening coefficients, resulting in average n_H-value of 0.57 with the smaller strain rate and 0.48 with the higher strain rate.

The strain hardening coefficient values of nickel-based superalloys found in literature, vary a lot, between 0.22-0.57 at room temperature, depending a lot on the heat treatments but also on the strain rates used in the experiments. The average strain hardening coefficient at room temperature of the material studied in this thesis was 0.28, meaning that it fits to the range of the values found in literature. However, more specific comparing is hard to perform, since the effect of strain rate is hard to evaluate, since the strain rate range of the experiments of this thesis was so narrow. Also, the chemical composition of the material is not known and nor is the heat treatment history.

6.4 Johnson-Cook model

The Johnson-Cook model was fitted to the experimental data. The Johnson-Cook model is given in Eq. 10 [132-136].

$$\sigma = \left[A + B\varepsilon_p^{n_{JC}}\right][1 + C \ln \dot{\varepsilon}^*][1 - T^{*m}], \tag{10}$$

where σ is the true stress, A is the yield strength, ε_p is the plastic strain, $\dot{\varepsilon}^*$ is the strain rate $\dot{\varepsilon}$ divided by the reference strain rate, $\dot{\varepsilon}_{ref}$, and B, n_{JC}, C, and m are constants that are determined to fit the model to the experimental data [132-136]. T* of the Equation 10 is given as Eq. 11

$$T^* = \frac{T - T_{ref}}{T_m - T_{ref}}, \tag{11}$$

where T is the temperature of the specimen, T_{ref} is the reference temperature, and T_m is the melting temperature of the material [132-136]. The Johnson-Cook model is a widely used constitutive equation that considers the effects of strain hardening, temperature and strain rate. [136] There are also a number of modified Johnson-Cook models available [132, 137-141], but in this thesis the unmodified Johnson-Cook model is used. The first term of the model represents the effect of work-hardening, second term the effect of strain rate, and the last part the effect of the temperature [136]. The Johnson-Cook model fitting is done in this thesis since the yield strength of the material cannot be obtained from the stress-strain curves due to the oscillations. With the fitting, a better estimation of the yield strengths can be achieved, even if some properties, for example a sharp yield point, might not be found out.

The exact melting temperature range of the specific material studied in this experiment is not known and therefore a literature value of 1350°C was used [135, 142-145].

Sample T01 was chosen as the reference sample, since it has the largest deformation. The reference strain rate used in the calculations is 431 1/s and the reference temperature is 20 °C. The first step of the fitting of the data to the model is to take the first term of the Johnson-Cook model, also known as Ludvik equation [135, 146], and fit it to the data of the reference sample, which is T01. The second term reduces to 1, since the strain rate is the reference strain rate. The third term is also reduced, since the temperature of the experiment is the reference temperature. The Ludvik equation was fitted to the experimental data with Matlab's curve fitting tool. After the fitting, the values were edited slightly by trial and error method to fit better to the experimental data. The resulting curve with the original data is presented in Figure 6.13.

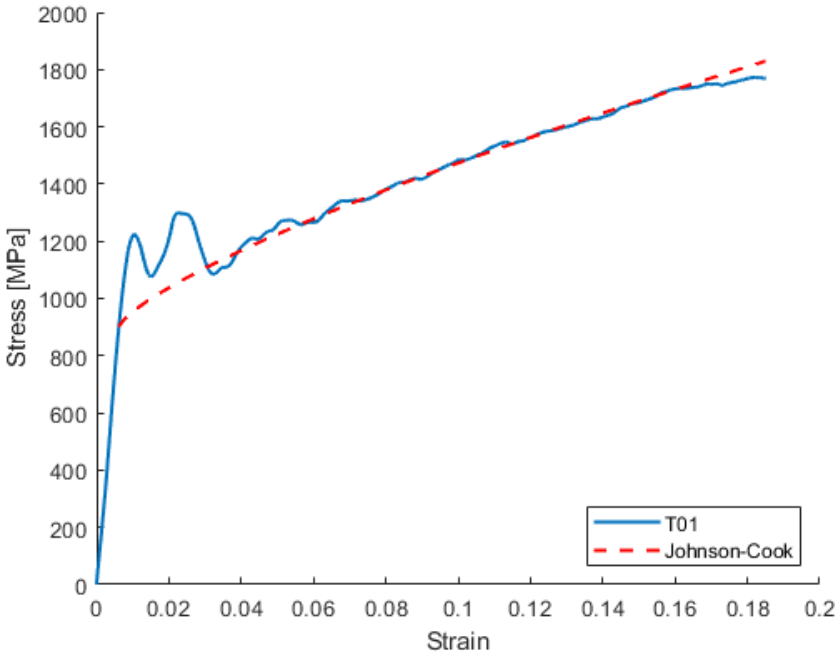

Figure 6.13. *The experimental data of sample T01 tested at room temperature at a strain rate of 431 1/s and the Johnson-Cook model.*

The fitting of the model is quite similar to the original data, excluding the oscillations in the beginning of the plastic deformation. Next step was to take the strain rate sensitive part of the equation into consideration by choosing a sample tested in the same temperature but at different strain rate. The strain rates in all the experiments were quite similar to each other, but sample T14 had the most different strain rate of the samples tested at room temperature when compared to the reference sample T01. The strain rate of sample T14 was 357 1/s. The value of constant C was then determined by trial and error by changing the value and plotting the curves. The resulting Johnson-Cook curve is presented in Figure 6.14.

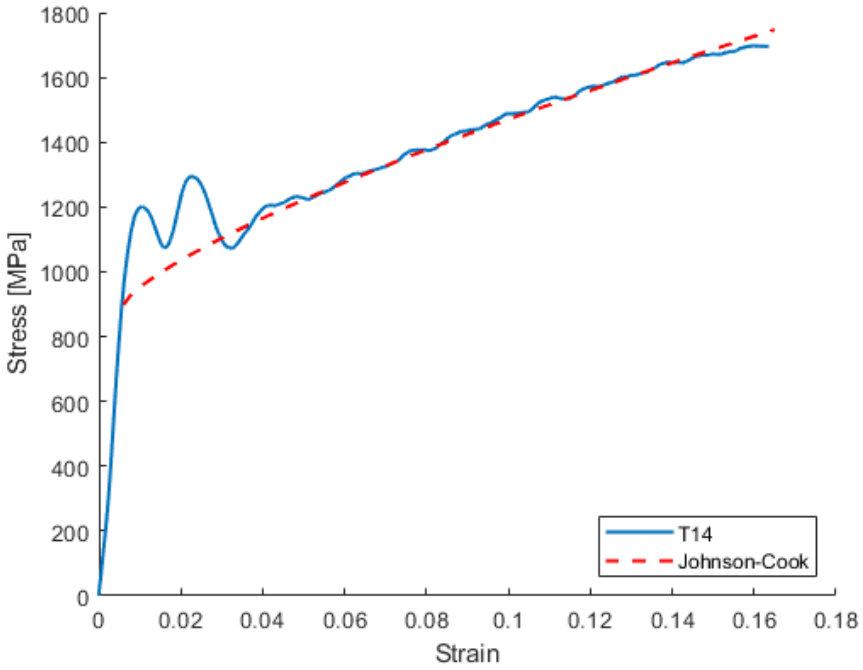

Figure 6.14. *The experimental data of sample T14 tested at room temperature at a strain rate of 357 1/s and the Johnson-Cook model.*

The calculated data is quite similar to the original data. The last part of the fitting was to take into consideration the last part of the Johnson-Cook model, which is the temperature term. For this, the Johnson-Cook model was fitted to two samples in each elevated temperature. At 650 °C the samples were T02 and T18 and at 760 °C they were T03 and T19. In Figure 6.15, the curves of sample T02 tested at 650 °C are shown.

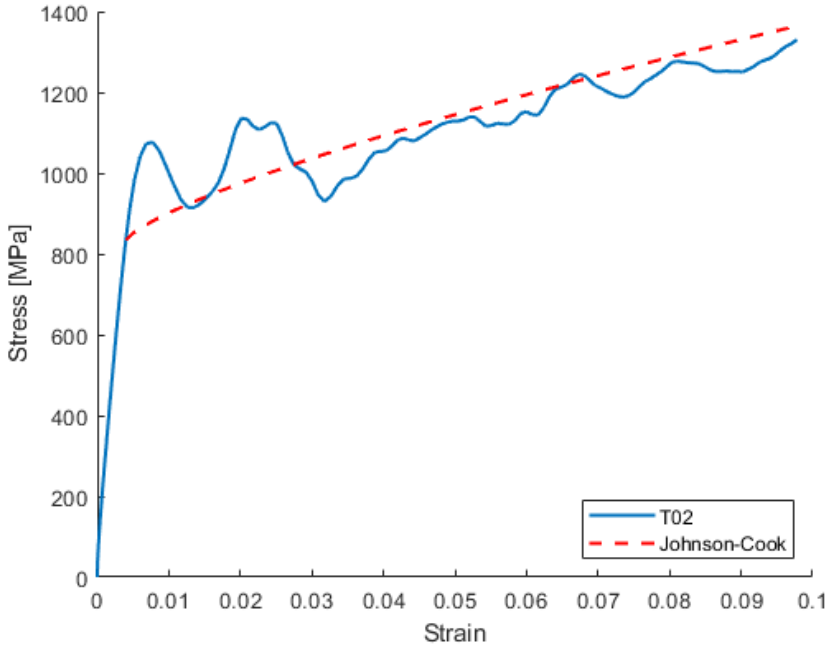

Figure 6.15. *The experimental data of sample T02 tested at 650 °C and at a strain rate of 414 1/s and the Johnson-Cook model.*

The last term and the constant m were the hardest to fit. For this reason, the Johnson-Cook model was fitted to two sets of experimental data in both elevated temperatures to make sure, that it represents the material properly. In Figure 6.16, the experimental data and the data calculated with the Johnson-Cook model of sample T18 tested at 650 °C, are presented.

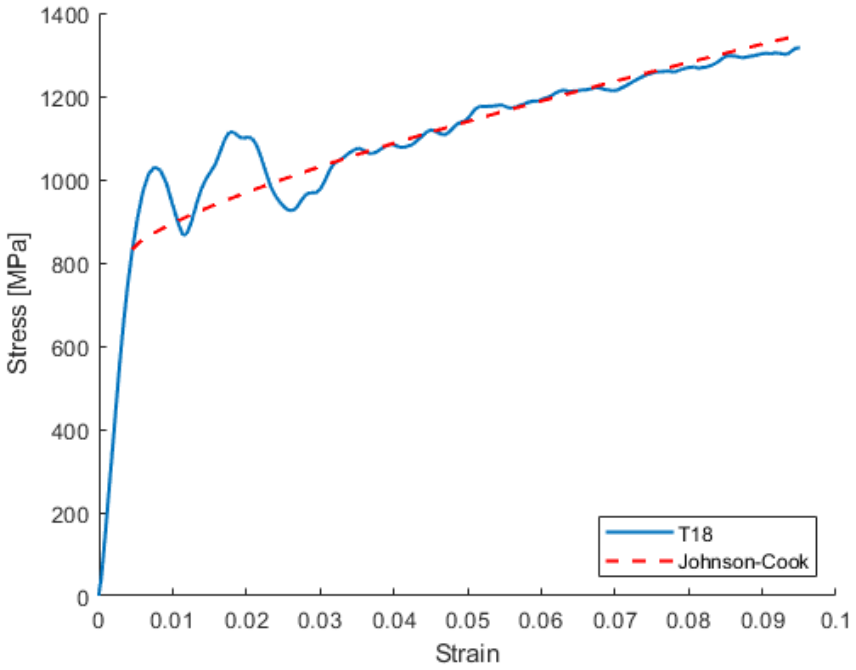

Figure 6.16. *The experimental data of sample T18 tested at 650 °C and at a strain rate of 321 1/s and the Johnson-Cook model.*

Rather good fitting was achieved with both samples tested at 650 °C, T02 and T18. In Figure 6.17, the curves of sample T03 tested at 760 °C are presented.

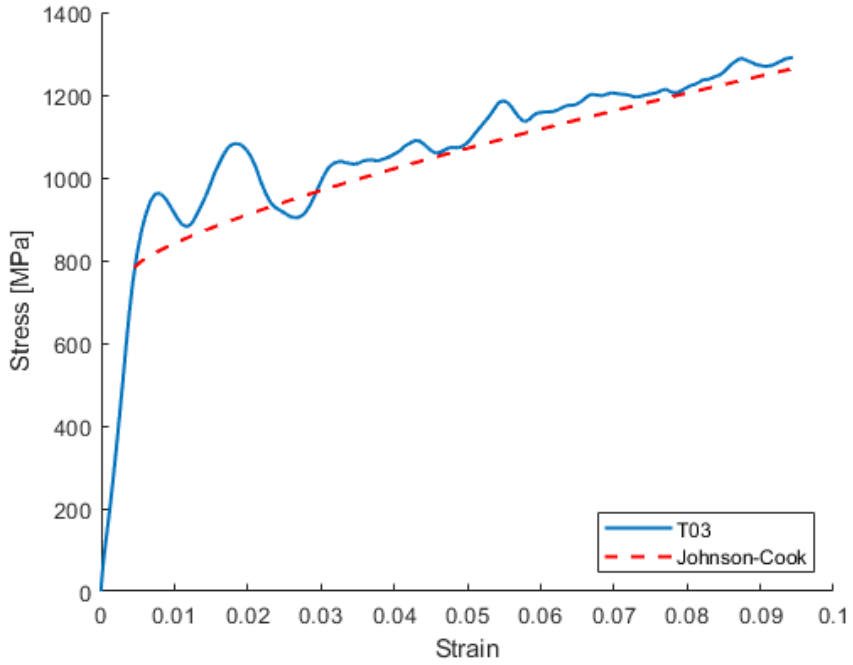

Figure 6.17. *The experimental data of sample T03 tested at 760 °C and at a strain rate of 313 1/s and the Johnson-Cook model.*

The fitting of the constant m was the hardest task, since the model gave slightly too high stress values for the samples tested at 650 °C and correspondingly slightly too low stress values for samples tested at 760 °C with the same value of m. However, with the value of m = 3.5, the model was rather presentative of the experimental data of each of the samples. In Figure 6.18, the Johnson-Cook model and experimental data of sample T19 are presented.

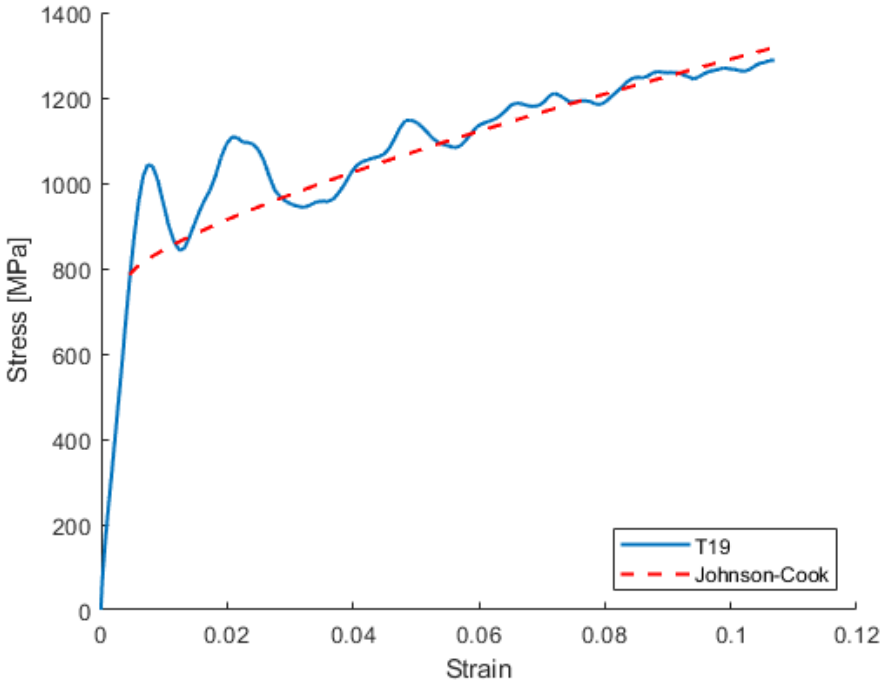

Figure 6.18. *The experimental data of sample T19 tested at 760 °C and at a strain rate of 451 1/s and the Johnson-Cook model.*

Determination of m was also done with trial and error in Matlab. Table 6.4.1 presents the values of the Johnson-Cook model parameters obtained with

Table 6.4.1. *The determined constants of the Johnson-Cook model.*

Constant	A (MPa)	B (MPa)	n_{JC}	C	m
Value	900	3377	0.75	0.01	3.5

Matlab's curve fitting -tool and trial and error. Table 6.4.2 presents some sets of constants for different nickel superalloys.

Table 6.4.2. *Some Johnson-Cook constants for nickel superalloys.*

Material	A (MPa)	B (MPa)	n_{JC}	C	m
Haynes 282 [145]	672.53	943.9	0.54	0.023	0.855
Inconel 718 I [143]	1108	699	0.5189	0.015	1.2861
Inconel 718 II [147]	1241	622	0.652	0.0134	1.30
Inconel 718 III [147]	450	1700	0.65	0.017	1.30
Inconel 718 IV [147]	1485	904	0.777	0.015	1.69
Inconel 718 V [148]	1350	1139	0.6522	0.0134	0
Inconel 718 VI [142]	1012	393	0.125	0.0271	2.42
Inconel 718 VII [142]	1012	511	0.396	0.0271	4.33
Inconel 718 VIII [142]	1012	513	0.422	0.0271	2.54
Alloy 625 [135]	558.8	2201	0.80	0.000209	1.146

As can be seen, the parameters differ from each other quite much, even the ones of the same material, depending on both the Johnson-Cook model itself but also on the possible heat treatments. Since the exact composition nor the heat treatment history of the material is not known, the comparison of the results is carried out in a more general manner, to see how the nickel-based superalloy studied in this thesis compares to other nickel-based superalloys used in jet engines.

The resulting constants of the fitting suggest that the material studied in this thesis work hardens considerably, since the values of n_{JC} and B are relatively high [135, 136], when compared to the values presented in Table 6.4.2. Also, the thermal softening effect of

the nickel-based superalloy studied in this thesis seems to be rather high, since the value of m is 3.5, only the Inconel 718 VII has a higher value. As discussed in Chapter 6.1, nickel-based superalloys typically have better tensile properties at higher temperatures than at room temperature, but the superalloy studied in this thesis has better properties at room temperature than at elevated temperatures.

Johnson-Cook model is used widely, and it is one of its biggest strengths since it makes comparing different experimental results easier, even if they have been made at different temperatures or strain rates. However, all the parameters are dependent on each other, as was noticed when the model fitting was done for this thesis. Also, the differences in the parameter sets of Inconel 718 presented in Table 6.4.2 could be explained with the dependency of the parameters.

6.5 Performance of studied material compared to Inconel 718

Inconel 718 is used in turbine engines, but not in the applications that operate at the highest temperatures but in the rotating parts which include for example shafts and blades. The yield strength and ultimate tensile strength of Inconel 718 are 1000 – 1200 MPa and 1200 – 1400 MPa [149-151] at room temperature, respectively. At 650 °C the yield strength of Inconel 718 is 900 - 1000 MPa and UTS is 1000-1200 MPa and at 760 °C, the corresponding values are 700 – 750 MPa at 760-800 °C [152, 153]. The yield strength and UTS of the material studied in this thesis were 900 ± 1 MPa and 1460 ± 11 MPa at RT, 830 ±1 MPa and 1200 ± 10 MPa at 650 °C and 780 ± 2 MPa and 1180 ± 12 MPa at 760 °C. When comparing these values, the studied material seems rather similar to Inconel 718. The ultimate tensile strengths are even higher than the corresponding Inconel 718 values, even at high temperatures which is in line with the Johnson-Cook parameter sets. Based on these results, when considering the strength, the novel nickel-based superalloy studied in this thesis would be a suitable material for jet engine turbine blades.

7 CONCLUSIONS

The material studied in this thesis is a novel nickel-based superalloy which is planned to be used in jet engine turbine blades, where the materials have to endure high temperatures as well as possible sudden impacts, causing high strain rates [126]. For this reason, both the temperature and strain rate dependency of the tensile properties of the alloy were studied. The material properties were compared to other nickel superalloys used in jet engines. Typically, the turbine blades are made of, for example, single crystal CMSX nickel superalloys, and when possible, the results were compared to CMSX-4, but also to other nickel-based superalloys including Inconel 718.

The yield strengths obtained with Matlab were 900 ± 1 MPa at room temperature, 830 ±1 MPa at 650 °C and 780 ± 2 MPa at 760 °C. When compared to materials used in turbine blades, the yield strengths were rather high at room temperatures and rather low at elevated temperatures when compared to nickel-based superalloys used in turbine engines. The ultimate tensile strengths were 1460 ± 11 MPa at room temperature, 1200 ± 10 MPa at 650 °C and 1180 ± 12 MPa at 760 °C. The ultimate tensile strength of the nickel-based superalloy studied in this thesis was rather high at room temperature and rather low at elevated temperatures in comparison to the values found literature. The yield strength and the ultimate tensile strength of nickel-based superalloys used in the highest temperature applications typically increase with increasing temperature [29, 30, 126] and have higher values at elevated temperatures than at room temperature which was not the case with the material studied in this thesis.

The yield strength and ultimate tensile strength of the material studied in this thesis were not affected by the strain rate much as the studied range of strain rates was very narrow. Neither the Hollomon strain hardening coefficients were visibly affected by the strain rate in this narrow strain rate range. The temperature dependence of the strain hardening coefficients on the other hand was quite clear, since at room temperature they had an average of 0.28, at 650 °C the average was 0.21, and at 760 °C the average was 0.19, decreasing rather linearly with temperature. The strain hardening coefficients were on the lower side, when compared to results of other experiments [130, 154, 155]. However, more exact comparison is impossible to do since the microstructure and the heat treatment history of the material studied in this thesis are not known.

Since the tensile properties did not improve at higher temperatures, it is presumable that the precipitates were quite small. Balicki et al. [27] studied the effect of the precipitate

size and concluded that with more coarse precipitates the yield strength and ultimate tensile strength enhanced more at elevated temperatures than with finer precipitates. This result was obtained at the strain rate of 10^{-3}. They also concluded that the strain hardening coefficients increase with increasing temperature with both fine and coarse precipitates, but more with more coarse precipitates.

A Johnson-Cook model was also fitted to the experimental data. The obtained parameters were A = 900 MPa, B = 3377 MPa, n = 0.75, C = 0.01, and m = 3.5. The work-hardening related parameters B and n_{JC}, were rather high when compared to other nickel-based superalloys found in literature, whose B-values varied between 400 and 2200 MPa and n_{JC}-values between 0.125 and 0.80. The coefficient related to the strain rate C was small, as can be presumed since the tensile properties of the material are not dependent on strain rate in this very narrow range. However, the strain rate dependency of the studied material in a larger strain rate range is not possible to evaluate with the results of the experiments of this thesis. The temperature related coefficient (m) was higher than in most of the reference parameter sets, and only the parameter set Inconel 718 VII [135] had higher value for m, being 4.33. As was discussed in Chapter 6.1, both the yield strength and the ultimate tensile strength decrease with increasing temperature, so the high value of m was expected.

All in all, the experiments were successful, since when excluding the three failed experiments, all the results were in line with each other and reasonable when compared to the reference results found in the literature. The material has good tensile properties at room temperature, when compared to other nickel superalloys used in turbine engines. However, the material does not hold the properties at high temperatures as nickel-based superalloys used in the applications that operate at the highest temperatures. When compared to Inconel 718, that is nowadays used for turbine blades, the yield strength and UTS are similar and UTS values are even higher, even at elevated temperatures. Based on these results, when considering only the yield strength and ultimate tensile strength, the material is suitable to be used in jet engine turbine blades.

To ensure the veracity of these results, however, more tests at different strain rates are needed, especially to study the strain rate sensitivity of the material. Also, the material should be studied at even higher temperatures than 760 °C, since the increasing of the strength of nickel-based superalloys can happen at even higher temperatures.

REFERENCES

[1] M.A. Meyers, K.K. Chawla, Chapter 13: Creep and Superplasticity, in: Anonymous (ed.), Mechanical behavior of materials, 2nd ed., Cambridge University Press, Cambridge, 2009, pp. 653-712.

[2] M. Meyers, K. Chawla, Imperfections: Point and Line Defects, in: K.K. Chawla, M.A. Meyers (ed.), Mechanical Behavior of Materials, 2nd ed., Cambridge University Press, Cambridge, 2008, pp. 251-320.

[3] U. Messerschmidt, Introduction, in: U. Messerschmidt (ed.), Dislocation Dynamics During Plastic Deformation, Springer Berlin Heidelberg, Berlin, Heidelberg, 2010, pp. 3-9.

[4] S. Nemat-Nasser, W.G. Guo, J.Y. Cheng, Mechanical properties and deformation mechanisms of a commercially pure titanium, Acta Materialia, Vol. 47, Iss. 13, 1999, pp. 3705-3720. http://www.sciencedirect.com/science/article/pii/S1359645499002037.

[5] A. Gilat, X. Wu, Plastic deformation of 1020 steel over a wide range of strain rates and temperatures, International Journal of Plasticity, Vol. 13, Iss. 6, 1997, pp. 611-632. http://www.sciencedirect.com/science/article/pii/S0749641997000284.

[6] J. Rämö, Experimental Studies and Numerical Modeling of Strain Rate and Temperature Dependent Material Behavior in Dynamic Processes, Tampere University, 2019, Available: https://trepo.tuni.fi/handle/10024/118057.

[7] U. Messerschmidt, Dislocation Motion, in: U. Messerschmidt (ed.), Dislocation Dynamics During Plastic Deformation, Springer Berlin Heidelberg, Berlin, Heidelberg, 2010, pp. 73-154.

[8] J. Wang, W. Guo, X. Gao, J. Su, The third-type of strain aging and the constitutive modeling of a Q235B steel over a wide range of temperatures and strain rates, International Journal of Plasticity, Vol. C, Iss. 65, 2015, pp. 85-107. https://www.infona.pl//resource/bwmeta1.element.elsevier-2700961f-d7a2-38f1-9561-20ee35492b95.

[9] D. Porter, K. Easterling, Phase Transformations in Metals and Alloys , 2nd ed. Springer-Science+Business Media, B.Y., 1992, .

[10] R.E. Smallman, A.H.W. Ngan, Physical Metallurgy and
Advanced Materials, Elsevier, 2007, .

[11] J.L. Barrilao, Microstructure Evolution of Laves Phase Strengthened Ferritic Steels for High Temperature Applications, 2017, .

[12] C. Solenthaler, M. Ramesh, P.J. Uggowitzer, R. Spolenak, Precipitation strengthening of Nb-stabilized TP347 austenitic steel by a dispersion of secondary Nb(C,N) formed upon a short-term hardening heat treatment, Materials Science and Engineering: A, Vol. 647, 2015, pp. 294-302. http://www.sciencedirect.com/science/article/pii/S0921509315303683.

[13] C. Li, Z. Wang, 9 - Computational modelling and ab initio calculations in MAX phases – I, in: I.M. Low (ed.), Advances in Science and Technology of Mn+1AXn Phases, Woodhead Publishing, 2012, pp. 197-222.

[14] D.N. Blaschke, Velocity dependent dislocation drag from phonon wind and crystal geometry, Journal of Physics and Chemistry of Solids, Vol. 124, 2019, pp. 24-35. https://www-sciencedirect-com.libproxy.tuni.fi/science/article/pii/S0022369718317323.

[15] G. Leibfried, Über den Einfluß thermisch angeregter Schallwellen auf die plastische Deformation, Zeitschrift für Physik, Vol. 127, 1950, pp. 344-356.

[16] D.N. Blaschke, E. Mottola, D.L. Preston, Dislocation drag from phonon wind in an isotropic crystal at large velocities, Philosophical Magazine, Vol. 100, Iss. 5, 2020, pp. 571-600. https://www-tandfonline-com.libproxy.tuni.fi/doi/full/10.1080/14786435.2019.1696484.

[17] B.N. Bhat Aerospace materials and applications, American Institute of Aeronautics and Astronautics, AIAA, Reston, VA, .

[18] Rolls Royce, The Jet Engine, 5th ed. Wiley, 2015, .

[19] How a Jet Engine Works, https://interestingengineering.com/how-a-jet-engine-works.

[20] A.S. Shaikh, Development of a gamma' Precipitation Hardening Ni-Base Superalloy for Additive Manufacturing, 2018, .

[21] Bhat, Biliyar N. et al., Chapter 2: Aerospace Materials Characteristics, in: Anonymous (ed.), Aerospace Materials and Applications, American Institute of Aeronautics and Astronautics, 2018, pp. 11-207.

[22] T.M. Pollock, R.D. Field, Chapter 63 Dislocations and high-temperature plastic deformation of superalloy single crystals, in: F.R.N. Nabarro, M.S. Duesbery (ed.), Dislocations in Solids, Elsevier, 2002, pp. 547-618.

[23] Y. Liu, Y. Wu, J. Yu, J. Ju, Z. Zhang, M. Kang, J. Wang, B. Sun, Y. Ning, Temperature-dependent deformation mechanisms and microstructural degradation of a polycrystalline nickel-based superalloy, Journal of Alloys and Compounds, Vol. 775, 2019, pp. 181-192. http://www.sciencedirect.com/science/article/pii/S0925838818337502.

[24] P.M. Mignanelli, N.G. Jones, M.C. Hardy, H.J. Stone, On the Time-Temperature-Transformation Behavior of a New Dual-Superlattice Nickel-Based Superalloy, Metallurgical and Materials Transactions A, Vol. 49, Iss. 3, 2018, pp. 699-707. https://link-springer-com.libproxy.tuni.fi/article/10.1007/s11661-017-4355-8.

[25] T. Courtney, Mechanical Properties of Materials, McGraw Hill, 2000, 203–205 p.

[26] M. Dodaran, A. Hemmasian Ettefagh, S.M. Guo, M.M. Khonsari, W.J. Meng, N. Shamsaei, S. Shao, Effect of alloying elements on the γ’ antiphase boundary energy in Ni-base superalloys, Intermetallics, Vol. 117, 2020, pp. 106670. https://www-sciencedirect-com.libproxy.tuni.fi/science/article/pii/S0966979519309227.

[27] E. Balikci, A. Raman, R. Mirshams, Tensile strengthening in the nickel-base superalloy IN738LC, Journal of Materials Engineering and Performance, Vol. 9, Iss. 3, 2000, pp. 324-329.

[28] H. Zhang, K. Zhang, H. Zhou, Z. Lu, C. Zhao, X. Yang, Effect of strain rate on microstructure evolution of a nickel-based superalloy during hot deformation, Materials & Design, Vol. 80, 2015, pp. 51-62. http://www.sciencedirect.com/science/article/pii/S0261306915002423.

[29] C. Körner, M. Ramsperger, C. Meid, D. Bürger, P. Wollgramm, M. Bartsch, G. Eggeler, Microstructure and Mechanical Properties of CMSX-4 Single Crystals Prepared by Additive Manufacturing, Metallurgical and Materials Transactions A, Vol. 49, Iss. 9, 2018, pp. 3781-3792. Available (accessed ID: Körner2018): https://doi.org/10.1007/s11661-018-4762-5.

[30] J. Liu, W. Tang, J. Li, Deformation and fracture behaviors of K403 Ni-based superalloy at elevated temperatures, Journal of Alloys and Compounds, Vol. 699, 2017, pp. 581-590. http://www.sciencedirect.com/science/article/pii/S0925838816342542.

[31] T. Zhou, H. Ding, X. Ma, W. Feng, H. Zhao, A. Li, Y. Meng, H. Zhang, Effect of precipitates on high-temperature tensile strength of a high W-content cast Ni-based superalloy, Journal of Alloys and Compounds, Vol. 797, 2019, pp. 486-496. http://www.sciencedirect.com/science/article/pii/S0925838819317499.

[32] E.W. Collings, The physical metallurgy of titanium alloys, American Society for Metals, Metals Park, OH, 1984, .

[33] H. Kolsky, An Investigation of the Mechanical Properties of Materials at very High Rates of Loading, Proceedings of the Physical Society. Section B, Vol. 62, Iss. 11, 1949, pp. 676–700. https://doi.org/10.1088%2F0370-1301%2F62%2F11%2F302.

[34] M. Meyers, Experimental Techniques: Methods to Produce Dynamic Deformation, in: Anonymous (ed.), Dynamic Behavior of Materials, 1994, pp. 296-322.

[35] W.W. Chen, B. Song, Conventional Kolsky bars, in: W. Chen, B. Song (ed.), Split Hopkinson (Kolsky) Bar: Design, Testing and Applications, Springer US, Boston, MA, 2011, pp. 1-35.

[36] A. Bracq, G. Haugou, R. Delille, F. Lauro, S. Roth, O. Mauzac, Experimental study of the strain rate dependence of a synthetic gel for ballistic blunt trauma assessment, Journal of the Mechanical Behavior of Biomedical Materials, Vol. 72, 2017, .

[37] W. Guo, X. Gao, On the constitutive modeling of a structural steel over a range of strain rates and temperatures, Materials Science and Engineering: A, Vol. 561, 2013, pp. 468-476. http://www.sciencedirect.com/science/article/pii/S0921509312015006.

[38] Dynamic Mechanics of Materials Laboratory Data from a Compression Split-Hopkinson Bar Experiment, https://dmm.engineering.osu.edu/materials/data-compression-split-hopkinson-bar-experiment.

[39] V. Vilamosa, A.H. Clausen, T. Børvik, B. Holmedal, O.S. Hopperstad, A physically-based constitutive model applied to AA6082 aluminium alloy at large strains, high strain rates and elevated temperatures, Materials & Design, Vol. 103, 2016, pp. 391-405. http://www.sciencedirect.com/science/article/pii/S0264127516305214.

[40] V. Vilamosa, A.H. Clausen, E. Fagerholt, O.S. Hopperstad, T. Børvik, Local Measurement of Stress–Strain Behaviour of Ductile Materials at Elevated Temperatures in a Split-Hopkinson Tension Bar System, Strain, Vol. 50, Iss. 3, 2014, pp. 223-235. https://onlinelibrary.wiley.com/doi/abs/10.1111/str.12084.

[41] V. Vilamosa, A.H. Clausen, T. Børvik, S.R. Skjervold, O.S. Hopperstad, Behaviour of Al-Mg-Si alloys at a wide range of temperatures and strain rates, International Journal of Impact Engineering, Vol. 86, 2015, pp. 223-239. http://www.sciencedirect.com/science/article/pii/S0734743X15001839.

[42] V. Vilamosa, A.H. Clausen, E. Fagerholt, O.S. Hopperstad, T. Børvik, Local Measurement of Stress–Strain Behaviour of Ductile Materials at Elevated Temperatures in a Split-Hopkinson Tension Bar System, Strain, Vol. 50, Iss. 3, 2014, pp. 223-235. Available (accessed https://onlinelibrary.wiley.com/doi/pdf/10.1111/str.12084): https://onlinelibrary.wiley.com/doi/abs/10.1111/str.12084.

[43] J. Kajberg, B. Wikman, Viscoplastic parameter estimation by high strain-rate experiments and inverse modelling – Speckle measurements and high-speed photography, International Journal of Solids and Structures, Vol. 44, Iss. 1, 2007, pp. 145-164. http://www.sciencedirect.com/science/article/pii/S0020768306001272.

[44] Z.N. Yin, T.J. Wang, Deformation response and constitutive modeling of PC, ABS and PC/ABS alloys under impact tensile loading, Materials Science and Engineering: A, Vol. 527,

Iss. 6, 2010, pp. 1461-1468. http://www.sciencedirect.com/science/article/pii/S092150930901226X.

[45] W.W. Chen, B. Song, Kolsky Bar for Dynamic Tensile/Torsion Experiments, in: W. Chen, B. Song (ed.), Split Hopkinson (Kolsky) Bar: Design, Testing and Applications, Springer US, Boston, MA, 2011, pp. 261-289.

[46] S. Nemat-Nasser, J.B. Isaacs, J.E. Starrett, Hopkinson techniques for dynamic recovery experiments, Proceedings of the Royal Society of London. Series A: Mathematical and Physical Sciences, Vol. 435, Iss. 1894, 1991, pp. 371-391. https://royalsocietypublishing.org/doi/10.1098/rspa.1991.0150.

[47] U.S. Lindholm, L.M. Yeakley, High strain-rate testing: Tension and compression, Experimental Mechanics, Vol. 8, Iss. 1, 1968, pp. 1-9. Available (accessed ID: Lindholm1968): https://doi.org/10.1007/BF02326244.

[48] T. Nicholas, Tensile testing of materials at high rates of strain, Experimental Mechanics, Vol. 21, Iss. 5, 1981, pp. 177-185. Available (accessed ID: Nicholas1981): https://doi.org/10.1007/BF02326644.

[49] F.E. Hauser, Techniques for measuring stress-strain relations at high strain rates, Experimental Mechanics, Vol. 6, Iss. 8, 1966, pp. 395-402. Available (accessed ID: Hauser1966): https://doi.org/10.1007/BF02326284.

[50] A. Fahem, A. Kidane, Hybrid Computational and Experimental Approach to Identify the Dynamic Initiation Fracture Toughness at High Loading Rate, in: Anonymous (ed.), Dynamic Behavior of Materials, 2018, pp. 141-146.

[51] W.E. Baker, C.H. Yew, Strain-Rate Effects in the Propagation of Torsional Plastic Waves, Journal of Applied Mechanics, Vol. 33, Iss. 4, 1966, pp. 917-923. Available (accessed 2020): https://doi.org/10.1115/1.3625202.

[52] A. Khosravifard, M.M. Moshksar, R. Ebrahimi, High strain rate torsional testing of a high manganese steel: Design and simulation, Materials & Design (1980-2015), Vol. 52, 2013, pp. 495-503. http://www.sciencedirect.com/science/article/pii/S0261306913005153.

[53] X. Yu, L. Chen, Q. Fang, X. Jiang & Y. Zhou, A Review of the Torsional Split Hopkinson Bar, Hindawi, https://www.hindawi.com/journals/ace/2018/2719741/.

[54] J. Duffy, J.D. Campbell, R.H. Hawley, On the Use of a Torsional Split Hopkinson Bar to Study Rate Effects in 1100-0 Aluminum, Journal of Applied Mechanics, Vol. 38, Iss. 1, 1971, pp. 83-91. https://asmedigitalcollection.asme.org/appliedmechanics/article/38/1/83/391653/On-the-Use-of-a-Torsional-Split-Hopkinson-Bar-to.

[55] X. Nie, R. Prabhu, W.W. Chen, J.M. Caruthers, T. Weerasooriya, A Kolsky Torsion Bar Technique for Characterization of Dynamic Shear Response of Soft Materials, Experimental Mechanics, Vol. 51, Iss. 9, 2011, pp. 1527-1534. Available (accessed ID: Nie2011): https://doi.org/10.1007/s11340-011-9481-4.

[56] Y. Zhou, Q. Fang, L. Chen, et al., A preliminary research on the rotating-wheel TSHB testing system, Proceedings of 11th National Conference on Explosion Mechanics, 2016, Zhuhai, China, pp. 248.

[57] X. Jiang, Y. Xiao, L. Chen, Q. Fang, Y. Zhou, An electromagnetic driven torsional split Hopkinson bar, Proceedings of 2nd International Conference on Impact Loading of Structures and Materials, 2018, Xi'an, China, pp. 103–105.

[58] M. Zhang, H.J. Wu, Q.M. Li, F.L. Huang, Further investigation on the dynamic compressive strength enhancement of concrete-like materials based on split Hopkinson pressure bar tests. Part I: Experiments, International Journal of Impact Engineering, Vol. 36, Iss. 12, 2009, pp. 1327-1334. http://www.sciencedirect.com/science/article/pii/S0734743X09000955.

[59] A.M. Eleiche, J. Duffy, Effects of temperature on the static and dynamic stress-strain characteristics in torsion of 1100-0 aluminum, International Journal of Mechanical Sciences, Vol. 17, Iss. 2, 1975, pp. 85-95. http://www.sciencedirect.com/science/article/pii/0020740375900016.

[60] Y. Li, Y. Guo, H. Hu, Q. Wei, A critical assessment of high-temperature dynamic mechanical testing of metals, International Journal of Impact Engineering, Vol. 36, Iss. 2, 2009, pp. 177-184. http://www.sciencedirect.com/science/article/pii/S0734743X08001188.

[61] O.S. Lee, M.S. Kim, Dynamic material property characterization by using split Hopkinson pressure bar (SHPB) technique, Nuclear Engineering and Design, Vol. 226, Iss. 2, 2003, pp. 119-125. http://www.sciencedirect.com/science/article/pii/S0029549303001894.

[62] A.M. Lennon, K.T. Ramesh, A technique for measuring the dynamic behavior of materials at high temperatures, International Journal of Plasticity, Vol. 14, Iss. 12, 1998, pp. 1279-1292. http://www.sciencedirect.com/science/article/pii/S0749641998000564.

[63] S.P. Mates, R. Rhorer, E. Whitenton, T. Burns, D. Basak, A Pulse-Heated Kolsky Bar Technique for Measuring the Flow Stress of Metals at High Loading and Heating Rates, Experimental Mechanics, Vol. 48, Iss. 6, 2008, pp. 799-807. Available (accessed ID: Mates2008): https://doi.org/10.1007/s11340-008-9137-1.

[64] V. Pare, P. Puthoor, K.N. Jonnalagadda, Murty, S. V. S. N., High Temperature Dynamic Characterization of an Aluminum Alloy with Modified Kolsky Bar, Procedia Engineering, Vol. 173, 2017, pp. 844-850. http://www.sciencedirect.com/science/article/pii/S1877705816345222.

[65] J. Kajberg, K.-. Sundin, Material characterisation using high-temperature Split Hopkinson pressure bar, Journal of Materials Processing Technology, Vol. 213, Iss. 4, 2013, pp. 522-531. http://www.sciencedirect.com/science/article/pii/S0924013612003330.

[66] M. Scapin, Mechanical characterization and modeling of the heavy tungsten alloy IT180, International Journal of Refractory Metals and Hard Materials, Vol. 50, 2015, pp. 258-268. http://www.sciencedirect.com/science/article/pii/S0263436815000190.

[67] B. Jiang, L. Cao, F. Zhu, Dynamic tensile behavior of polypropylene with temperature effect, Composites Part B: Engineering, Vol. 152, 2018, pp. 300-304. http://www.sciencedirect.com/science/article/pii/S1359836818315385.

[68] Y.B. Lu, Q.M. Li, Dynamic behavior of polymers at high strain-rates based on split Hopkinson pressure bar tests, International Journal of Impact Engineering, Vol. 38, Iss. 1, 2011, pp. 41-50. http://www.sciencedirect.com/science/article/pii/S0734743X10001223.

[69] Z. Xu, F. Huang, Thermomechanical behavior and constitutive modeling of tungsten-based composite over wide temperature and strain rate ranges, International Journal of Plasticity, Vol. 40, 2013, pp. 163-184. http://www.sciencedirect.com/science/article/pii/S0749641912001209.

[70] A. Aldoshan, S. Khanna, Dynamic High Temperature Compression of Carbon Nanotubes Reinforced Aluminum Foams, Journal of Dynamic Behavior of Materials, Vol. 3, Iss. 1, 2017, pp. 1-11. Available (accessed ID: Aldoshan2017): https://doi.org/10.1007/s40870-016-0088-9.

[71] W.W. Chen, B. Song, Kolsky Compression Bar Experiments on Soft Materials, in: W. Chen, B. Song (ed.), Split Hopkinson (Kolsky) Bar: Design, Testing and Applications, Springer US, Boston, MA, 2011, pp. 119-175.

[72] Z. Ruan, L. Chen, Q. Fang, Numerical investigation into dynamic responses of RC columns subjected for fire and blast, Journal of Loss Prevention in the Process Industries, Vol. 34, 2015, pp. 10-21. http://www.sciencedirect.com/science/article/pii/S0950423015000108.

[73] C. Liu, Y. Li, Z. Wu, W. Guo, Y. Ge, Dynamic compression behavior of heated concrete, Tumu Gongcheng Xuebao/China Civil Engineering Journal, Vol. 44, Iss. 4, 2011, pp. 78-83.

[74] J.-. Tao, L.-. Qin, K. Li, D. Liu, B. Jia, X.-. Chen, G. Chen, Experimental investigation on dynamic compression mechanical performance of concrete at high temperature, Baozha Yu Chongji/Explosion and Shock Waves, Vol. 31, Iss. 1, 2011, pp. 101-106.

[75] Y.-. He, J.-. Huo, B.-. Chen, Y. Xiao, Tests on dynamic behavior of concrete at elevated temperatures, J.Railw. Sci. Eng., Vol. 8, Iss. 7 SUPPL, 2010, pp. 27-30.

[76] X. Yu, L. Chen, Q. Fang, Z. Ruan, J. Hong, H. Xiang, A concrete constitutive model considering coupled effects of high temperature and high strain rate, International Journal of Impact Engineering, Vol. 101, 2017, pp. 66-77. http://www.sciencedirect.com/science/article/pii/S0734743X16305814.

[77] K. Xia, W. Yao, Dynamic rock tests using split Hopkinson (Kolsky) bar system – A review, Journal of Rock Mechanics and Geotechnical Engineering, Vol. 7, 2014, .

[78] J. Lankford, Temperature-strain rate dependance of compressive strength and damage mechanisms in aluminium oxide, Journal of Materials Science, Vol. 16, Iss. 6, 1981, pp. 1567-1578.

[79] W.W. Chen, B. Song, Kolsky Compression Bar Experiments on Brittle Materials, in: W. Chen, B. Song (ed.), Split Hopkinson (Kolsky) Bar: Design, Testing and Applications, Springer US, Boston, MA, 2011, pp. 77-118.

[80] P. Verleysen, J. Peirs, J. Van Slycken, K. Faes, L. Duchene, Effect of strain rate on the forming behaviour of sheet metals, Journal of Materials Processing Technology, Vol. 211, Iss. 8, 2011, pp. 1457-1464. http://www.sciencedirect.com/science/article/pii/S0924013611000859.

[81] P. Verleysen, J. Degrieck, Experimental investigation of the deformation of Hopkinson bar specimens, International Journal of Impact Engineering, Vol. 30, Iss. 3, 2004, pp. 239-253. http://www.sciencedirect.com/science/article/pii/S0734743X03000691.

[82] H. Huh, W.J. Kang, S.S. Han, A tension split Hopkinson bar for investigating the dynamic behavior of sheet metals, Experimental mechanics, Vol. 42, Iss. 1, 2002, pp. 8-17. https://search.datacite.org/works/10.1007/bf02411046.

[83] V. Tarigopula, O.S. Hopperstad, M. Langseth, A.H. Clausen, F. Hild, A study of localisation in dual-phase high-strength steels under dynamic loading using digital image correlation and FE analysis, International Journal of Solids and Structures, Vol. 45, Iss. 2, 2008, pp. 601-619. http://www.sciencedirect.com/science/article/pii/S0020768307003411.

[84] Y. Chen, A.H. Clausen, O.S. Hopperstad, M. Langseth, Application of a split-Hopkinson tension bar in a mutual assessment of experimental tests and numerical predictions, International Journal of Impact Engineering, Vol. 38, Iss. 10, 2011, pp. 824-836. http://www.sciencedirect.com/science/article/pii/S0734743X11000790.

[85] R. Bobbili, A. Paman, V. Madhu, High strain rate tensile behavior of Al-4.8Cu-1.2Mg alloy, Materials Science and Engineering: A, Vol. 651, 2016, pp. 753-762. http://www.sciencedirect.com/science/article/pii/S0921509315306213.

[86] F. Feng, S. Huang, Z. Meng, J. Hu, Y. Lei, M. Zhou, Z. Yang, A constitutive and fracture model for AZ31B magnesium alloy in the tensile state, Materials Science and Engineering: A, Vol. 594, 2014, pp. 334-343. http://www.sciencedirect.com/science/article/pii/S0921509313012264.

[87] S. Fu, Y. Wang, Y. Wang, Tension testing of polycarbonate at high strain rates, Polymer Testing, Vol. 28, Iss. 7, 2009, pp. 724-729. http://www.sciencedirect.com/science/article/pii/S0142941809001020.

[88] J.T. Fan, J. Weerheijm, L.J. Sluys, Glass interface effect on high-strain-rate tensile response of a soft polyurethane elastomeric polymer material, Composites Science and Technology, Vol. 118, 2015, pp. 55-62. http://www.sciencedirect.com/science/article/pii/S0266353815300555.

[89] T. Zhong, Z.Y. Zhong, J.W. Huang, T. Sun, K. Fezzaa, J.Y. Huang, S.N. Luo, Rate-dependent phase transition of high density polyethylene, Materialia, Vol. 6, 2019, pp. 100274. http://www.sciencedirect.com/science/article/pii/S2589152919300705.

[90] A.A. Heravi, I. Curosu, V. Mechtcherine, A gravity-driven split Hopkinson tension bar for investigating quasi-ductile and strain-hardening cement-based composites under tensile impact loading, Cement and Concrete Composites, Vol. 105, 2020, pp. 103430. http://www.sciencedirect.com/science/article/pii/S0958946519312739.

[91] A.C.C. Trindade, A.A. Heravi, I. Curosu, M. Liebscher, F. de Andrade Silva, V. Mechtcherine, Tensile behavior of strain-hardening geopolymer composites (SHGC) under impact loading, Cement and Concrete Composites, Vol. 113, 2020, pp. 103703. http://www.sciencedirect.com/science/article/pii/S0958946520302109.

[92] Z. Song, S. Li, J. Lei, R.L. Noble, Z. Wang, Dynamic tensile properties of ROP/OCC natural hybrid fibers reinforced composites, Composite Structures, Vol. 185, 2018, pp. 600-606. http://www.sciencedirect.com/science/article/pii/S026382231732041X.

[93] X. Chen, C. Chen, L. Cheng, W. Chen, An investigation of dynamic failure progress and properties of 2D C/SiC composite from 173 K to 1273 K by SHTB, Composites Part B: Engineering, Vol. 116, 2017, pp. 30-39. http://www.sciencedirect.com/science/article/pii/S1359836816320169.

[94] R. Guo, H. Ren, L. Zhang, Z. Long, X. Jiang, X. Wu, H. Wang, Direct dynamic tensile study of concrete materials based on mesoscale model, International Journal of Impact Engineering, Vol. 143, 2020, pp. 103598. http://www.sciencedirect.com/science/article/pii/S0734743X20300737.

[95] J. Lim, J. Hong, W.W. Chen, T. Weerasooriya, Mechanical response of pig skin under dynamic tensile loading, International Journal of Impact Engineering, Vol. 38, Iss. 2, 2011, pp. 130-135. http://www.sciencedirect.com/science/article/pii/S0734743X10001351.

[96] J. Duffy, R.H. Hawley, R.A. Frantz, The Deformation of Lead in Torsion at High Strain Rates, Journal of Applied Mechanics, Vol. 39, Iss. 3, 1972, pp. 651-656. https://asmedigitalcollection.asme.org/appliedmechanics/article/39/3/651/387305/The-Deformation-of-Lead-in-Torsion-at-High-Strain.

[97] J. Lipkin, J.D. Campbell, J.C. Swearengen, The effects of strain-rate variations on the flow stress of OFHC copper†, Journal of the Mechanics and Physics of Solids, Vol. 26, Iss. 4, 1978, pp. 251-268. http://www.sciencedirect.com/science/article/pii/0022509678900200.

[98] K.T. Ramesh, On the localization of shearing deformations in tungsten heavy alloys, Mechanics of Materials, Vol. 17, Iss. 2, 1994, pp. 165-173. http://www.sciencedirect.com/science/article/pii/0167663694900574.

[99] J.E. Lawson, T. Nicholas, The dynamic mechanical behavior of titanium in shear, Journal of the Mechanics and Physics of Solids, Vol. 20, Iss. 2, 1972, pp. 65-76. http://www.sciencedirect.com/science/article/pii/0022509672900312.

[100] W. Lee, Z. Tang, Relationship between mechanical properties and microstructural response of 6061-T6 aluminum alloy impacted at elevated temperatures, Materials & Design, Vol. 58, 2014, pp. 116-124. http://www.sciencedirect.com/science/article/pii/S026130691400082X.

[101] J. Wang, W. Guo, P. Li, P. Zhou, Z. Wang, Dynamic tensile properties of a single crystal Nickel-base superalloy at high temperatures measured with an improved SHTB technique, Materials Science and Engineering: A, Vol. 670, 2016, pp. 1-8. http://www.sciencedirect.com/science/article/pii/S0921509316306475.

[102] S. Nemat-Nasser, J.B. Isaacs, Direct measurement of isothermal flow stress of metals at elevated temperatures and high strain rates with application to Ta and TaW alloys, Acta Materialia, Vol. 45, Iss. 3, 1997, pp. 907-919. http://www.sciencedirect.com/science/article/pii/S1359645496002431.

[103] J. Wang, W. Guo, Y. Su, P. Zhou, K. Yuan, Anomalous behaviors of a single-crystal Nickel-base superalloy over a wide range of temperatures and strain rates, Mechanics of Materials, Vol. 94, 2016, pp. 79-90. http://www.sciencedirect.com/science/article/pii/S0167663615002574.

[104] M. Shazly, V. Prakash, S. Draper, Mechanical behavior of Gamma-Met PX under uniaxial loading at elevated temperatures and high strain rates, International Journal of Solids and Structures, Vol. 41, Iss. 22, 2004, pp. 6485-6503. http://www.sciencedirect.com/science/article/pii/S0020768304002410.

[105] R. Bobbili, V. Madhu, A.K. Gogia, Tensile behaviour of aluminium 7017 alloy at various temperatures and strain rates, Journal of Materials Research and Technology, Vol. 5, Iss. 2, 2016, pp. 190-197. http://www.sciencedirect.com/science/article/pii/S2238785415001234.

[106] R. Bobbili, A. Paman, V. Madhu, High strain rate tensile behavior of Al-4.8Cu-1.2Mg alloy, Materials Science and Engineering: A, Vol. 651, 2016, pp. 753-762. http://www.sciencedirect.com/science/article/pii/S0921509315306213.

[107] W. Huang, X. Zan, X. Nie, M. Gong, Y. Wang, Y. Xia, Experimental study on the dynamic tensile behavior of a poly-crystal pure titanium at elevated temperatures, Materials Science and Engineering: A, Vol. 443, Iss. 1, 2007, pp. 33-41. http://www.sciencedirect.com/science/article/pii/S0921509306010574.

[108] R. Smerd, S. Winkler, C. Salisbury, M. Worswick, D. Lloyd, M. Finn, High strain rate tensile testing of automotive aluminum alloy sheet, International Journal of Impact Engineering, Vol. 32, Iss. 1, 2005, pp. 541-560. http://www.sciencedirect.com/science/article/pii/S0734743X05000680.

[109] F. Feng, S. Huang, Z. Meng, J. Hu, Y. Lei, M. Zhou, D. Wu, Z. Yang, Experimental study on tensile property of AZ31B magnesium alloy at different high strain rates and temperatures, Materials & Design, Vol. 57, 2014, pp. 10-20. http://www.sciencedirect.com/science/article/pii/S0261306913011643.

[110] D. Forni, B. Chiaia, E. Cadoni, High strain rate response of S355 at high temperatures, Materials & Design, Vol. 94, 2016, pp. 467-478. http://www.sciencedirect.com/science/article/pii/S0264127515310200.

[111] Z. Rosenberg, D. Dawicke, E. Strader, S.J. Bless, A new technique for heating specimens in split-Hopkinson-bar experiments using induction-coil heaters, Experimental Mechanics, Vol. 26, Iss. 3, 1986, pp. 275-278.

[112] A. Pandey, A.S. Khan, E. Kim, S. Choi, T. Gnäupel-Herold, Experimental and numerical investigations of yield surface, texture, and deformation mechanisms in AA5754 over low to high temperatures and strain rates, International Journal of Plasticity, Vol. 41, 2013, pp. 165-188. http://www.sciencedirect.com/science/article/pii/S0749641912001362.

[113] S.L. Lemanski, N. Petrinic, G.N. Nurick, Experimental Characterisation of Aluminium 6082 at Varying Temperature and Strain Rate, Strain, Vol. 49, Iss. 2, 2013, pp. 147-157. Available (accessed https://onlinelibrary.wiley.com/doi/pdf/10.1111/str.12022): https://onlinelibrary.wiley.com/doi/abs/10.1111/str.12022.

[114] S. Curtze, V.-. Kuokkala, M. Hokka, P. Peura, Deformation behavior of TRIP and DP steels in tension at different temperatures over a wide range of strain rates, Materials Science and Engineering: A, Vol. 507, Iss. 1, 2009, pp. 124-131. http://www.sciencedirect.com/science/article/pii/S0921509308013464.

[115] S.P. Shamchi, Queirós de Melo, Francisco J. M., P.J. Tavares, Moreira, Pedro M. G. P., Thermomechanical characterization of Alclad AA2024-T3 aluminum alloy using split Hopkinson tension bar, Mechanics of Materials, Vol. 139, 2019, pp. 103198. http://www.sciencedirect.com/science/article/pii/S0167663619303795.

[116] J.L. Chiddister, L.E. Malvern, Compression-impact testing of aluminum at elevated temperatures, Experimental Mechanics, Vol. 3, Iss. 4, 1963, pp. 81-90. Available (accessed ID: Chiddister1963): https://doi.org/10.1007/BF02325890.

[117] J. Wang, W. Guo, P. Li, P. Zhou, Z. Wang, Dynamic tensile properties of a single crystal Nickel-base superalloy at high temperatures measured with an improved SHTB technique, Materials Science and Engineering: A, Vol. 670, 2016, pp. 1-8. http://www.sciencedirect.com/science/article/pii/S0921509316306475.

[118] S. Sen, B. Banerjee, A. Shaw, Taylor impact test revisited: Determination of plasticity parameters for metals at high strain rate, International Journal of Solids and Structures, Vol. 193-194, 2020, pp. 357-374. http://www.sciencedirect.com/science/article/pii/S0020768320300615.

[119] H. Lim, J.D. Carroll, C.C. Battaile, S.R. Chen, A.P. Moore, J.M.D. Lane, Anisotropy and Strain Localization in Dynamic Impact Experiments of Tantalum Single Crystals, Scientific Reports, Vol. 8, Iss. 1, 2018, pp. 1-6. https://www.nature.com/articles/s41598-018-23879-1.

[120] D.E. Eakins, N.N. Thadhani, Instrumented Taylor anvil-on-rod impact tests for validating applicability of standard strength models to transient deformation states, Journal of Applied Physics, Vol. 100, Iss. 7, 2006, pp. 073503. https://aip.scitation.org/doi/full/10.1063/1.2354326.

[121] A. Mardoukhi, High Temperature High Strain Rate Behavior of Superalloy MA 760, Tampere University of Technology, 2013, Available: https://trepo.tuni.fi/handle/123456789/21756.

[122] T. Tang, G. Ren, Z. Guo, Q. Li, An improved technique of expanding metal ring experiment under high explosive loading, Review of Scientific Instruments, Vol. 84, Iss. 4, 2013, pp. 043908. https://aip.scitation.org/doi/10.1063/1.4802255.

[123] J. Zhang, Y. Zheng, F. Zhou, J. Liu, Experimental Technique for Dynamic Fragmentation of Liquid-Driving Expanding Ring, EPJ Web of Conferences, Vol. 183, 2018, pp. 02034.

[124] P.C. Johnson, B.A. Stein, R.S. Davis, Measurement of Dynamic Plastic Flow Properties under Uniform Stress, in: N.o. University, D.M. Rocky (ed.), ASTM International, West Conshohocken, PA, 1963, pp. 195-207.

[125] S.J. Ling, J. Sanny, B. Moebs, 17.3: Speed of Sound, in: Anonymous (ed.), Physics LibreTexts, 2016, .

[126] J. Wang, W. Guo, J. Guo, Z. Wang, S. Lu, The Effects of Stress Triaxiality, Temperature and Strain Rate on the Fracture Characteristics of a Nickel-Base Superalloy, Journal of Materials Engineering and Performance, Vol. 25, Iss. 5, 2016, pp. 2043-2052. Available (accessed ID: Wang2016): https://doi.org/10.1007/s11665-016-2049-9.

[127] Z.H. Tan, X.G. Wang, Y.L. Du, T.F. Duan, Y.H. Yang, J.L. Liu, J.D. Liu, L. Yang, J.G. Li, Y.Z. Zhou, X.F. Sun, Temperature dependence on tensile deformation mechanisms in a novel Nickel-based single crystal superalloy, Materials Science and Engineering: A, Vol. 776, 2020, pp. 138997. http://www.sciencedirect.com/science/article/pii/S0921509320300861.

[128] J. CAO, F. LI, X. MA, Z. SUN, Tensile stress–strain behavior of metallic alloys, Transactions of Nonferrous Metals Society of China, Vol. 27, Iss. 11, 2017, pp. 2443-2453. http://dx.doi.org/10.1016/S1003-6326(17)60271-1.

[129] R. Kwesi Nutor, Using the Hollomon Model to Predict Strain-Hardening in Metals, American Journal of Materials Synthesis and Processing, Vol. 2, Iss. 1, 2017, pp. 1.

[130] K. Gopinath, A.K. Gogia, S.V. Kamat, R. Balamuralikrishnan, U. Ramamurty, Tensile Properties of Ni-Based Superalloy 720Li: Temperature and Strain Rate Effects, Metallurgical and Materials Transactions A, Vol. 39, Iss. 10, 2008, pp. 2340-2350. Available (accessed ID: Gopinath2008): https://doi.org/10.1007/s11661-008-9585-3.

[131] H. Zhang, P. Li, X. Gong, T. Wang, L. Li, Y. Liu, Q. Wang, Tensile properties, strain rate sensitivity and failure mechanism of single crystal superalloys CMSX-4, Materials Science and Engineering: A, Vol. 782, 2020, pp. 139105. http://www.sciencedirect.com/science/article/pii/S0921509320301933.

[132] A. He, G. Xie, H. Zhang, X. Wang, A comparative study on Johnson–Cook, modified Johnson–Cook and Arrhenius-type constitutive models to predict the high temperature flow stress in 20CrMo alloy steel, Materials & Design (1980-2015), Vol. 52, 2013, pp. 677-685. http://www.sciencedirect.com/science/article/pii/S0261306913005438.

[133] A. Banerjee, S. Dhar, S. Acharyya, D. Datta, N. Nayak, Determination of Johnson cook material and failure model constants and numerical modelling of Charpy impact test of armour steel, Materials Science and Engineering: A, Vol. 640, 2015, pp. 200-209. http://www.sciencedirect.com/science/article/pii/S0921509315300228.

[134] M.E. Korkmaz, M. Günay, P. Verleysen, Investigation of tensile Johnson-Cook model parameters for Nimonic 80A superalloy, Journal of Alloys and Compounds, Vol. 801, 2019, pp. 542-549. http://www.sciencedirect.com/science/article/pii/S0925838819322340.

[135] M. Hokka, D. Gomon, A. Shrot, T. Leemet, M. Bäker, V.-. Kuokkala, Dynamic Behavior and High Speed Machining of Ti-6246 and Alloy 625 Superalloys: Experimental and Modeling Approaches, Experimental Mechanics, Vol. 54, Iss. 2, 2014, pp. 199-210. Available (accessed ID: Hokka2014): https://doi.org/10.1007/s11340-013-9793-7.

[136] M. Meyers, K. Chawla, Plasticity, in: K.K. Chawla, M.A. Meyers (ed.), Mechanical Behavior of Materials, 2nd ed., Cambridge University Press, Cambridge, 2008, pp. 161-250.

[137] L. Niu, M. Cao, Z. Liang, B. Han, Q. Zhang, A modified Johnson-Cook model considering strain softening of A356 alloy, Materials Science and Engineering: A, Vol. 789, 2020, pp. 139612. http://www.sciencedirect.com/science/article/pii/S0921509320306900.

[138] R. Chakrabarty, J. Song, A modified Johnson-Cook material model with strain gradient plasticity consideration for numerical simulation of cold spray process, Surface and Coatings Technology, Vol. 397, 2020, pp. 125981. http://www.sciencedirect.com/science/article/pii/S0257897220306502.

[139] Y. Zhao, J. Sun, J. Li, Y. Yan, P. Wang, A comparative study on Johnson-Cook and modified Johnson-Cook constitutive material model to predict the dynamic behavior laser additive manufacturing FeCr alloy, Journal of Alloys and Compounds, Vol. 723, 2017, pp. 179-187. http://www.sciencedirect.com/science/article/pii/S0925838817322594.

[140] Z.X. Li, M. Zhan, X.G. Fan, J.Q. Tan, A modified Johnson-Cook model of as-quenched AA2219 considering negative to positive strain rate sensitivities over a wide temperature range, Procedia Engineering, Vol. 207, 2017, pp. 155-160. http://www.sciencedirect.com/science/article/pii/S1877705817355297.

[141] R. Bobbili, V. Madhu, A modified Johnson-Cook model for FeCoNiCr high entropy alloy over a wide range of strain rates, Materials Letters, Vol. 218, 2018, pp. 103-105. http://www.sciencedirect.com/science/article/pii/S0167577X18301812.

[142] W. Grzesik, P. Niesłony, P. Laskowski, Determination of Material Constitutive Laws for Inconel 718 Superalloy Under Different Strain Rates and Working Temperatures, Journal of Materials Engineering and Performance, Vol. 26, Iss. 12, 2017, pp. 5705-5714. Available (accessed ID: Grzesik2017): https://doi.org/10.1007/s11665-017-3017-8.

[143] H.K. Farahani, M. Ketabchi, S. Zangeneh, Determination of Johnson–Cook Plasticity Model Parameters for Inconel718, Journal of Materials Engineering and Performance, Vol. 26, Iss. 11, 2017, pp. 5284-5293. Available (accessed ID: Farahani2017): https://doi.org/10.1007/s11665-017-2990-2.

[144] X. Wang, C. Huang, B. Zou, H. Liu, H. Zhu, J. Wang, Dynamic behavior and a modified Johnson–Cook constitutive model of Inconel 718 at high strain rate and elevated temperature, Materials Science and Engineering: A, Vol. 580, 2013, pp. 385-390. http://www.sciencedirect.com/science/article/pii/S0921509313006023.

[145] M. Rodríguez-Millán, J. Díaz-Álvarez, R. Bernier, J.L. Cantero, A. Rusinek, M.H. Miguelez, .Thermo-Viscoplastic Behavior of Ni-Based Superalloy Haynes 282 and Its Application to Machining Simulation, Metals, Vol. 12, Iss. 561, 2017, https://www.mdpi.com/2075-4701/7/12/561#cite.

[146] H. Shin, j. Kim, A Phenomenological Constitutive Equation to Describe Various Flow Stress Behaviors of Materials in Wide Strain Rate and Temperature Regimes, Journal of Engineering Materials and Technology, Vol. 132, 2010, .

[147] E. Uhlmann, von der Schulenburg, M. Graf, R. Zettier, Finite Element Modeling and Cutting Simulation of Inconel 718, CIRP Annals, Vol. 56, Iss. 1, 2007, pp. 61-64. http://www.sciencedirect.com/science/article/pii/S0007850607000170.

[148] A. Iturbe, E. Giraud, E. Hormaetxe, A. Garay, G. Germain, K. Ostolaza, P.J. Arrazola, Mechanical characterization and modelling of Inconel 718 material behavior for machining process assessment, Materials Science and Engineering: A, Vol. 682, 2017, pp. 441-453. http://www.sciencedirect.com/science/article/pii/S0921509316314071.

[149] A. Shokrani, V. Dhokia, S. Newman, R. Imani Asrai, An Initial Study of the Effect of Using Liquid Nitrogen Coolant on the Surface Roughness of Inconel 718 Nickel-Based Alloy in CNC Milling, Procedia CIRP, Vol. 3, 2012, pp. 121–125.

[150] P. BHARTI, MAHESHWARI, C. Sharma, Experimental investigation of Inconel 718 during die-sinking electric discharge machining, International Journal of Engineering Science and Technology, Vol. 2, 2010, .

[151] L.M. Maiyar, R. Ramanujam, K. Venkatesan, J. Jerald, Optimization of Machining Parameters for end Milling of Inconel 718 Super Alloy Using Taguchi based Grey Relational Analysis,

Procedia Engineering, Vol. 64, 2013, pp. 1276-1282. http://www.sciencedirect.com/science/article/pii/S1877705813017220.

[152] INCONEL 718 TECHNICAL DATA, https://www.hightempmetals.com/techdata/hitempInconel718data.php.

[153] VDM® Alloy 718, .

[154] K.V.U. Praveen, G.V.S. Sastry, V. Singh, Work-Hardening Behavior of the Ni-Fe Based Superalloy IN718, Metallurgical and Materials Transactions A, Vol. 39, Iss. 1, 2008, pp. 65-78. Available (accessed ID: Praveen2008): https://doi.org/10.1007/s11661-007-9375-3.

[155] C. Tian, G. Han, C. Cui, X. Sun, Effects of Co content on tensile properties and deformation behaviors of Ni-based disk superalloys at different temperatures, Materials & Design, Vol. 88, 2015, pp. 123-131. http://www.sciencedirect.com/science/article/pii/S0264127515303671.